UNIVERSITY OF BELGRADE

SCHOOL OF ELECTRICAL ENGINEERING

Dragan Pavlović

Plasma channel evolution in the triggered lightning discharges

Doctoral Dissertation

Belgrade, 2019

УНИВЕРЗИТЕТ У БЕОГРАДУ

ЕЛЕКТРОТЕХНИЧКИ ФАКУЛТЕТ

Драган Павловић

Еволуција плазма канала код тригерованих атмосферских пражњења

Докторска дисертација

Београд, 2019

Committee members

PhD Jovan Cvetić, Dissertation Advisor
Full Professor
School of Electrical Engineering, University of Belgrade

PhD Tomislav Šekara
Full Professor
School of Electrical Engineering, University of Belgrade

PhD Milorad Kuraica
Full Professor
Faculty of Physics, University of Belgrade

PhD Gradimir Milovanović
Full member of the
Serbian Academy of Sciences and Arts

PhD Branko Kolundžija
Full Professor
School of Electrical Engineering, University of Belgrade

Defense date:

————————————————

To my family

Acknowledgments

Dissertation Title: Plasma channel evolution in the triggered lightning discharge

Abstract: Plasma channel evolution is of fundamental interest for the study of the lightning physics, the electrodynamics of the atmosphere and for electrical engineering practice. The subject of this dissertation is the development of detailed and efficient numerical algorithms for application in the study of the lightning channel evolution.

First off all, the classical numerical methods for the calculating the three - dimensional integrals were used to calculate the axial electric field along the lightning channel axis. The results measurement of the negative triggered lightning discharge have been used as input parameters during calculation. Different engineering models were used in the calculation - the TL, the MTLE, the MTLP, the MTLE and the GTCS model. Obtained results for electric field as well as the point form of Ohm's law have been used to calculate the profile of longitudinal electrical conductivity on the lightning channel. The comparison with the experimental results was performed. It has been shown that the mean values of the mentioned physical quantities are in accordance with the experimental results. On the basis of the experimental results and semi-empirical formulas, other essential parameters of the lightning channel (the concentration and the temperature of the carriers) can be estimated.

After a detailed overview of all methods used in the literature to study the lightning channel dynamics, the decision was to use the GTCS model. For this purpose, it is necessary to precisely calculate the channel discharge function from Volterra integral equation of the first kind. This equation is solved analytically by Laplace transformation, as well as by the convolution quadrature method (CQ method). The Volterra equation is also solved by the modified composite trapezoidal formula method (MCTF method), which is one of the numerical methods used to provide a very high degree of accuracy with minimal approximations. Results showed excellent agreement with the analytical method. Obtained channel discharge function is used in the calculations of other physical parameters along radial and axial directions of the channel.

Based on the afore stated results, the guidelines for further study of the lightning channel dynamics are given.

Наслов дисертације: Еволуција плазма канала код тригерованих атмосферских пражњења

Сажетак: Еволуција канала је од базичног значаја за проучавање физике канала муње, електродинамике атмосфере као и за електроинжењерску праксу. Циљ ове дисертације је развој детаљних аналитичких и нумеричких алгоритама за примену у проучавању еволуције канала муње.

Као прво, класичне нумеричке методе израчунавање тродимензионалних интеграла су коришћене за израчунавање аксијалног електричног поља дуж осе канала муње. Резултати мерења код негативних тригерованих атмосферских пражњења су коришћени као улазни параметри током прорачуна. У прорчуну су коришћени различити инжењерски модели - TL, MTLE, MTLP, MTLE и GTCS модел. За израчунавање профила подужне електричне проводности у каналу муње коришћени су добијени резултати за електрично поље као и Омов закон у локалном облику. Извршено је поређење са експерименталним резултатима. Показано је да су средње вредности наведених физичких величина у складу са експерименталним резултатима. На основу експерименталних резултата и полуемпиријских формула, могу се проценити остали битни параметри канала муње (концентрација и температура носилаца).

После детаљног прегледа свих метода који се користе у литератури за проучавање динамике канала муње, одлучено је да се користи GTCS модел. За ту сврху потребно је прецизно израчунати функцију пражњења из Волтерине интегралне једначине прве врсте. Једначина је решена аналитички, методом Лапласове трансформације, као и методом конволуционих квадратура (CQ method (engl. *convolution quadrature method*)). Једначина је такође решена нумеричком методом модификоване композитне трапезне формуле (MCTF method), која је једна од нумеричких метода коришћена да обезбеди веома висок степен тачности уз минималне апроксимације. Добијени аналитички резултати су показали одлично слагање са нумеричком методом. Добијена функција пражњења канала се користи за прорачун других физичких параметара дуж радијалног и аксијалног правца.

На основу претходно наведених резултата, дате су смернице за даље проуча-

вање динамике канала муње.

Кључне речи: електрично поље, електрична проводност, динамика канала муње, Волтерина интегрална једначина, аналитички методи, нумерички методи, Лапласова трансформација, конволуционе квадратуре.

Научна област: Електротехника и рачунарство.

Ужа научна област: Физика плазме.

УДК: 621.3.

Contents

List of Tables

List of Figures

Chapter 1

Introduction

Electrical phenomena in the atmosphere are in the sphere of interest of the scientific community for more than two decades, since the linear correlation between global frequency, intensity of atmospheric discharges and temperature rise on the Earth's surface has been established. For the atmospheric physics, cloud-to-ground (CG) lightning and upper-atmospheric lightning are areas of special interest. Negative lightning represents over 80 % of all cloud-to-ground (CG) lightnings. This type of discharge is very important for research in the field of plasma physics and electrodynamics of the atmosphere. CG lightnings are also very important for engineering practice due to significant damage that lightning current may produce.

The modeling of the lightning channel processes is very complex, but studying the plasma physics and plasma confinement configuration of charged particles are said to receive much attention. The first necessary prerequisite for fusion experiments is to form a high performance plasma. These plasmas have high density, temperature and long confinement time [1]. For lightning, it does not meet these conditions, concerning temperature and density but the confinement of charges in the channel take place in a way that has not been completely explored at all.

Numerical simulations of the process inside the lightning channel are hardly solvable due to the large number of complex physical processes that occur simultaneously. In order analysis to carry out, the certain assumptions must be introduced to facilitate the computation processes. One intriguing approximation is to treat the channel with engineering return stroke models. These models are relatively simple, as opposed to complex hydrodynamic model [2] that monitors the evolution of the lightning channel parameters in time and space. Engineering return stroke models can incorporate a model of the charged corona sheath surrounded by the uncharged highly conductive lightning channel core. They can also took into account the evolution of the channel incorporating hydrodynamics, energy losses and Joule heating

[3]. It is necessary to say that lightning physics is more complex than any of the suggested models.

The subject of the dissertation is the development of advanced, detailed and efficient methods for the modeling of the processes in lightning channel. The aim of the dissertation is to give new insights into dynamics of the processes along return stroke. This dissertation is organized in chapters as follows:

- The introductory chapter gives an overview of the problem of the modeling the plasma channel evolution. The role and the significance of this topic from the aspect of physics is discussed. In the Section 1.1 the challenges that one faces in modeling of such processes are listed, as well as the ways in which the problems can be overcome.

- Chapter 2 is dedicated to the basic facts about electric discharge in gases. Also, mechanisms of electrical discharges in gases, Townsend (Subsection 2.2.2) and streamer mechanism (Subsection 2.2.3), are described in detail in Section 2.2. At the end of this Chapter a description of electrical arc is given, since this kind of discharge is most similar to channel core characteristics;

- Chapter 3 presents the basic physical mechanisms of lightning flash, as well as the models of the return stroke. Special attention has been paid to the Transmission line type of models (TLM) description (Section 3.4) as well as the description of the Traveling current source type of models (TCS, Section 3.5). Also, the Section 3.7 provides a detailed description of the Generalized Traveling Current Return Stroke (GTCS) Model;

- Chapter 4 gives an insight into the corona sheath dynamics. In particular, Section 4.1 gives an overview of the experiments used to verify the results of the theoretical predictions. A detailed description of the two models that predict charge motion in the corona sheath is given in Section 4.2 and Section 4.3;

- In Chapter 5.1, a detailed calculation of the vertical electric field along the channel axis is given. The conductivity of the channel core is calculated in the Section 5.2. In Section 5.3, a new channel discharge function is calculated taking into account the ground current reflections. It is proposed that they affect the dynamics of the corona sheath;

- Methods for solving the Volterra integral equation are derived in the Chapter 6. An analytical method is presented and examined in details, as well as the

numerical methods that provide convergent solutions. A comparative analysis has been done and the solutions of several examples are given;

- Conclusion of dissertation is given in Chapter 7.

1.1   General information about lightning research

Engineering return stroke models are used to calculate the most important parameters in lightning channel evolution. Detail overview of these models is given in reference [69]. In the dissertation the GTCS model [58] will be used as referent model for which it has been shown that it unites all the engineering models theoretically, and at the same time includes the physics of gas discharges into calculation.

Further research will focus on the application of these models to the study of internal plasma channel evolution. Also, there is a need to connect these models to gas discharge physics [4] and physics of suddenly created plasma [7]. If the study shows that these models have certain limitations, the space for development of new physical and engineering models will be opened. The area of process modeling in the lightning channel is in the developing phase, both in theoretical and practical terms.

The initial assumptions of this research were:

- The lightning channel is straight and vertical;

- The return stroke is modeled by engineering models;

- The lightning channel consists of a corona sheath surrounding central core. The corona sheath contains almost all charge and has low conductivity, while the core (with the diameter in order of 1 cm) contains negligible charge and has high conductivity. The corona envelope consists of two zones [77];

- The distribution of positive and negative charges in the corona sheath is azimuthal and radially homogeneous [78];

- At the distance where measurement was performed (10 cm), electrostatic component of the electric field is dominant and induction and radiation components are negligible [80];

- Two cases of soil influence on the dynamics of the lightning channel were modelled (cases $R = 0$ and $R = 1$);

The latest techniques for triggering lightning enabled precise measurements of the horizontal electric field near the striking point on a distance of only 10 cm from the channel core. At the same time, the current at the striking point was measured. These experiments are carried out at Camp Blanding campus in Florida [80]. The measurement results will be taken as the input data for calculating the channel discharge function.

Integral methods have been applied to various return stroke engineering models in order to calculate the electric field inside the lightning channel. The point form of Ohm's law is applied for the calculation the electrical conductivity of the lightning channel, as well as to obtain the time profile of electrical conductivity. For the determination of the lightning channel parameters, theoretical results that have already been mentioned will be compared to the experimental results [81].

First, it is necessary to calculate the channel discharge function in order to obtain the distribution of certain physical quantities along radial and axial directions of the lightning channel, it has been decided to describe the lightning channel dynamics by means of the GTCS model. The question was whether the problem could be solved in closed analytical form. If an analytical solution was obtained, then this would be a great result for further research.

Chapter 2

Electric discharge in gases

Knowledge of the laws of electric discharges in gases is important for studying atmospheric phenomena because these laws provide an explanation for the occurrence of the electric charges and the formation of electricity in gases. On the other hand, knowledge of plasma physics is a prerequisite for a detailed understanding of the process in the lightning channel. Therefore, a brief overview of plasma physics and gas discharge physics is given in this chapter. A qualitative overview of the parameters for all types of DC discharges is also presented.

2.1 Gases and Plasma

An electric current presents a flow of electric charge. In metals, electricity is carried out by electrons, while in electrolytes and ionized gases it is carried out by positive and negative ions and electrons.

At atmospheric pressure and at room temperature, there are small concentration of free electrons or ions in gases. Because of this, gases are good insulators. In order for gas to become a good conductor, it is necessary to ionize atoms and molecules. Charged particles appear in the gas due to ionization processes.
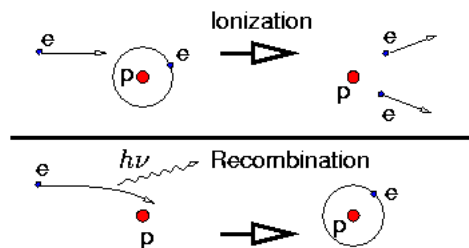
Figure 2.1: Ionization and recombination in the gas. Adapted from [5].

Ionization is the process of the formation of the charged particles, ions and electrons, from neutral atoms and molecules. Ionization in various ways can be caused by an electron, which moves through the gas, if it has sufficient kinetic energy to throw out electron from neutral atom in a collision with it. During the ionization, electrons come out from the atomic orbital and thus generate free electrons and positive ions (Fig. 2.1). Free electrons can be combined with neutral atoms or molecules, thus forming negative ions. After these processes, free charges are formed in the gas subsequently rendering it a medium that can potentially conduct electricity.

Ionization energy is a required amount of energy that removes the valence electron from isolated atoms or molecules. The first ionization energy of an element is energy that needs to remove the highest energy electron from a neutral atom in the gas phase. The first ionization energy of hydrogen is measured in the experiment and is equal to $\triangle H^0 = -13212.0$ kJ/mol (this process would be represented by the following equation $H(g) \rightarrow H^+(g) + e^-$). The first ionization energy for different gases is given in Fig. 2.2.
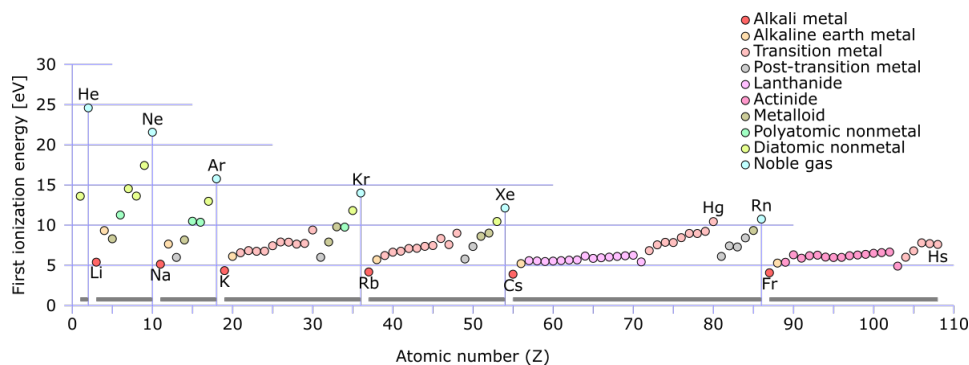
Figure 2.2: The first ionization energy of different elements. Adapted from [6].

In general, for ionization of gases some external source of the ionization is required. Gases can be ionized in several ways: with X-ray and UV radiation, naturally occurring radiation, gas temperature increment, and high voltage application on electrodes or collisions of electrons or other elementary particles with gas molecules. The number of created ions depends on the strength of the ionizer.

Positive ions and negative electrons can be connected thereby forming neutral atoms and molecules. This process is called recombination. Recombination leads to a decrease in the number of ions in the gas. As a result, the conductivity of the gas decreases. Recombination of ions occurs in the presence of ionizers, but then a balance between the number of formed and recombinant ions is set up. The conductivity of gases, produced under the influence of the external sources (ionizers) is rapidly decreasing when the source is removed.

Electrical particles move chaotically in gas. Additionally, the particles in the gas can be moved directionally due to the effects of the electric field and concentration gradient. In ionized gases, both conditions occur simultaneously. Electric discharges in gases occurs when electric current flow through gases, because of the previously caused ionization of the gas. The positive ions move in the direction of electric field, while the negative ions and electrons move in the opposite directions. The characteristic of gas discharge depends on: the type of the gas, pressure and temperature of the gas, the types of electrodes, the relative position, and shape and dimensions of the electrodes. Also, very important parameter represents the voltage, current and electric power of the power supply connected to the gas tube electrodes.

Ionized gas is the gas that contains neutral molecules, ions and electrons. Plasma is the fourth state of matter , and it is obtained from ionized gas in which the density of positive and negative charges is practically the same. The basic characteristic of plasma is the electroneutrality. Inside the volume, plasma is high-conductive structure in which long-range electric and magnetic fields have dominant influence to the behavior of the matter [8]. Examples of plasma can be found in nature (for example, lightning, aurora borealis, ionosphere), but the majority of plasma for use is produced in gas laboratories. Some typical naturally occurring and laboratory plasmas are illustrated in Fig. 2.3. It can be clearly seen in Fig. 2.3 that different types of plasma vary considerably in terms of characteristic parameters (such as temperature, pressure, plasma density). However, the definition of plasma is fulfilled for all types.

The charged particles in plasma interact with each other particles individually (this type of interaction is the Coulomb interaction) but also through the so-called *averaged field* with all other charged particles. Namely, around the charged particles (for example electrons) the opposite charge particles are collected and formed a spherical cloud, which is called the *Debye sphere* of a certain radius - *Debye radius* r_D [9]. These particles shield the electron and change its electric potential (Fig. 2.4).

The result of this is that every charge particles interact with the charge particles in the sphere, while the effect on the interaction outside the sphere is negligible. Debye radius is then:

$$r_D = \left(\frac{\varepsilon_0 \cdot \mathrm{k} \cdot T}{n_e \cdot \mathrm{e}^2} \right)^{\frac{1}{2}} \tag{2.1}$$

where the ε_0 is the dielectric permittivity of vacuum, k is the Boltzmann constant, e is the elementary charge, T is the temperature and n_e is the electron density. For
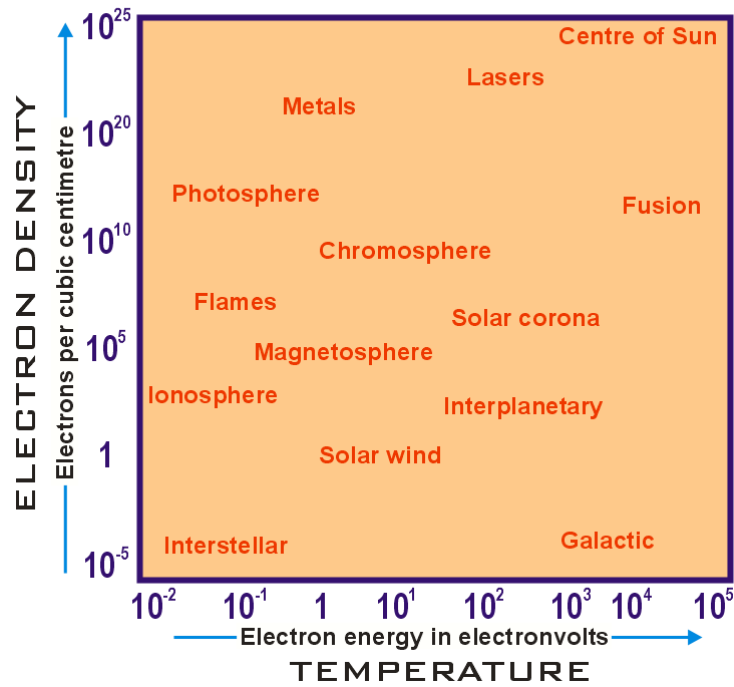
Figure 2.3: The different plasmas according to their temperature with respect to their density. Adapted from [6].
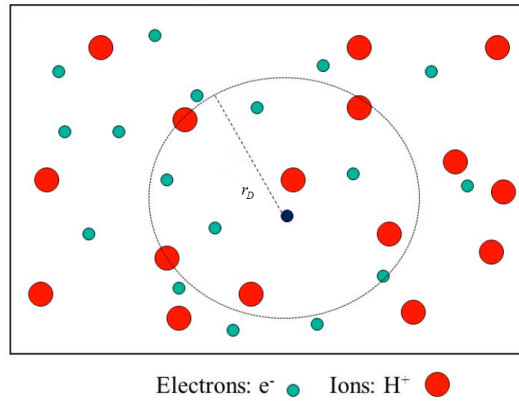
Figure 2.4: Debye radius in plasma.

example, for plasma with temperature $T = 10000$ K and electron density $n_e = 10^{16}$ m^{-3}, $r_D = 6,9 \cdot 10^{-5}$ m is obtained.

Plasma emits its own electromagnetic radiation in the frequency spectrum, $f = 10^5 - 10^{11}$ Hz. This radiation originates from the electron oscillation in plasma.

The occurrence of these oscillations is associated with the conservation of quasi-neutrality in plasma. Actually, any shift of the electron in relation to the charge particle leads to the strong electric field that returns electron back. Electron starts to oscillate with Langmuir frequency ω_p:

$$\omega_p = \sqrt{\frac{n_e \cdot e^2}{m_e \cdot \epsilon_0}} \tag{2.2}$$

All in all, an ionized gas could be called plasma, if it satisfies the following conditions:

- *Plasma parameter* - the number of particles in a sphere of radius equal to the Debye radius r_D; this number must be large, sufficient for collective effects. This condition can be written as $r_D \cdot n \gg 1$, and n is the concentration of the particles in plasma [10];

- *Debye shielding* - the Debye radius should be law in comparison to the dimension on plasma. This criterion means that the interactions which occur inside plasma are more significant than those on its surface. Under this condition, plasma can be considered as a quasi-neutral. The mathematical expression of this condition is: $r_D/L \ll 1$ [11];

- *Plasma frequency* - The time between impacts is long compared to the plasma oscillation. The plasma oscillation is larger than the electron-neutral plasma frequency. When this condition is met, electrodynamic interactions are more dominant than the processes of the molecular-kinetic interaction. This condition can be written in the following way: $\tau \cdot \omega_{pl} \gg 1$;

All these conditions are rarely fulfilled in gas discharge experiments. For example, in gas discharge only one part of channel in discharge is in the form of plasma.

It is important to say that, unlike gases, liquids and solid state, the plasma is a higher-energy state of the matter , Fig. 2.5. More specifically, plasma is not a stable state, but requires constant energy investment for maintenance of the state. Otherwise, if the source of ionization is removed, electrons and ions would be recombined and plasma decay would occur in a very short period of time.

A characteristic feature of the plasma, unlike other aggregate states, is the shielding of electrostatic interactions. In gases, solids and liquids, the polarization of atoms and molecules leads to a decrease in the interaction between charges on a value determined by dielectric constant. In plasma, the interaction does not simply decrease, it is very fast, exponentially, fading with increasing distance between
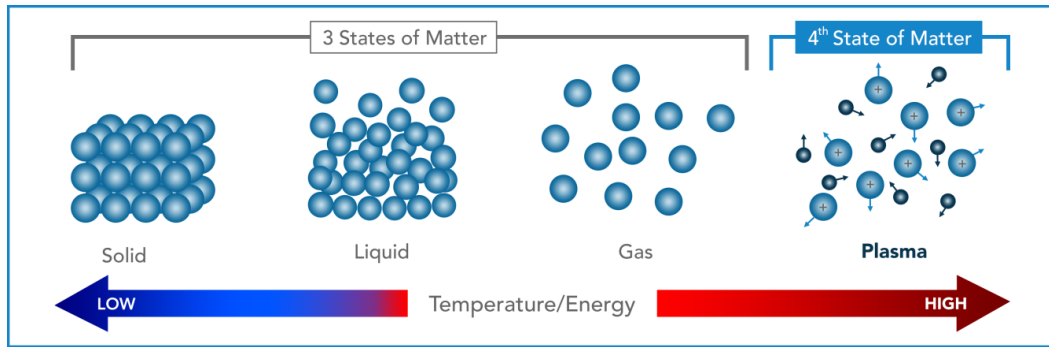
Figure 2.5: States of matter and its energy. Adapted from [6].

charges. This shielding is caused by the rebuilding of the charge density of the opposite sign around any charge. Due to the screening, the electrons and ions in the plasma move as if in the averaged field, and they can be interpreted as free particles.

Due to the screening, the external electric field does not penetrate into plasma at a distance, much bigger than the Debye length. However, a magnetic field can penetrate the plasma. Plasma in which the magnetic field is strong enough to influence the motion of charged particles is called magnetized plasma.

Plasma state has the most similarities with the gaseous state because it does not have a constant shape and volume. There are some differences when comparing plasma and gases. The conductivity of plasma is very high, but in the gas state it is very low. The velocity distribution of the particles in gases is always Maxwellian, however in plasma it is non-Maxwellian. The main difference between plasma and gases is that the electromagnetic field is an essential part of plasma, along with atoms, ions and electrons. There is no clearly defined phase transition between gas and plasma. The substance passes to plasma state of gas gradually with an increase in the degree of ionization.

2.1.1 Classification of plasmas

The fields of gas discharge and plasma physics are quite extensive and contain a lot of different physical effects, and therefore are quite complicated. Also, the processes of obtaining electrical discharges are very diverse. Some of these processes are suitable for realization, but some of these are very complex.

Gas must be ionized to be turned into plasma state. The degree of ionization is proportional to the number of atoms that gave or absorbed the electrons, and most depends on the temperature. Even weakly ionized gas, in which less than 1 % of particles are in an ionized state, may exhibit some typical properties of plasma (inte-

raction with the external electromagnetic field and high electrical conductivity). The degree of ionization α is defined as $\alpha = n_i/(n_i + n_a)$, where n_e is the concentration of ions and n_a the concentration of neutral atoms after ionization. Depending on the degree of ionization, plasma is divided into [13]:

- *Weakly ionized plasma* $\rightarrow \alpha < 10^{-4}$;

- *Ionized medium* $\rightarrow 10^{-4} < \alpha < 10^{-2}$;

- *Strongly ionized* $\rightarrow \alpha > 10^{-2}$;

- *Totally ionized* $\rightarrow \alpha = 1$;

Depending on the pressure between electrons and ions, plasmas that exist are:

- *Low-pressure plasma.* In this category, there are glow discharge, capacitively and inductively coupled plasmas as well as microwave plasmas. These plasmas are generally low-temperature plasmas;

- *Atmospheric-pressure plasma.* In this category there are: corona discharge, arc discharge and dielectric barrier discharges (DBD).

Depending on the temperature of the electrons and ions in plasmas, plasmas are divided into:

- *Non-thermal (Low-temperature, Non-equilibrium) plasma.* In these plasmas, the temperatures of the ions and electrons are different. The ions in these plasmas are at room temperatures, but the electron temperatures are the thousands of degrees Celsius. Low-temperature plasma is characterized by a small degree of ionization (up to 1 %). Since such plasmas are often used in technological processes, they are sometimes called *technological plasmas*. Most often they are created by means of electric fields, which accelerate electrons, which in turn ionize atoms. Electrical fields are introduced into the gas by inductive or capacitive couplings (see inductively coupled plasma). Typical applications of low-temperature plasma include plasma modification of surface properties (diamond films, metal nitriding, change in wettability), plasma etching of surfaces (semiconductor industry), purification of gases and liquids (water ozonation and soot particles burning in diesel engines). These plasmas are easily produced at low pressure. In this category plasmas are as follows: glow discharge, capacitively coupled plasmas, microwave discharge and DBD plasmas;

- *Thermal plasmas.* In thermal plasmas, the temperatures of the ions and electrons are the same and most of energy goes into gas heating and walls of the chamber. Hot plasma is almost always completely ionized (ionization rate ~ 100 %). Examples of these plasmas are: different types of arcs, inductively coupled plasmas and lightning.

According to the character of the electric breakdown in gases, the mechanism of the breakdown can be classified in two categories:

- *Townsend mechanism*;

- *Streamer mechanism.*

For the electricity flow through the gases, there is need for charge carriers and an electric field that will direct them. In laboratory conditions, plasma is most often obtained by applying DC electric field, or applying high voltage to the electrodes. For the purpose of lightning research, it is important to review the process of the electric discharge in gases in DC electric field. The brief overview of the important physical process is given in Chapter 2.2. According to the fact that the discharge is maintained without an external ionization source, discharges are divided into two categories:

- *Non-self-sustained discharge*;

- *Self-sustained discharge.*

The self-sustained discharges are more common in physical practice. These discharges are also of great importance for engineering practice. Stable self-sustained discharges are:

- *Glow discharges*;

- *Arc discharges*;

- *Corona discharges*;

- *Spark discharges.*

Generalized classification of the gas discharges also exists. Electric discharge is classified according to the state of ionized gas and the frequency range of the applied field. Primary characteristics make the difference between: breakdown in gases, non-thermal plasma and thermal plasma. The second characteristic make the

difference between the frequency of electric field that is applied and therefore, the following type of discharge are: (1) DC, low-frequency and impulse electric field, (2) radio-frequency electric field ($f \sim 10^5 - 10^6$ Hz), (3) microwave electric field ($f \sim 10^9 - 10^{11}$ Hz, $\lambda \sim 10^2 - 10^{-1}$ cm) and (4) optical field (from infrared to ultraviolet light). This classification has lead to 12 different types of discharge [12]. Every type of this discharge is experimentally confirmed. The detailed overview of the gas discharge type is given in the Table 2.1.

Table 2.1: Parameters of laboratory plasmas. Adapted from [14].

	Breakdown	Non-Thermal Plasmas	Thermal Plasmas
Constant electric field	Initiation of glow discharge	Positive column of a glow discharge	Positive column of high-pressure arcs
Radio frequencies	Initiation of RF discharge	Capacitively coupled RF discharge	Inductively coupled RF discharge
Microwave range	Breakdown in waveguides and resonators	Microwave discharges in rare field gases	Microwave plasmatron
Optical range	Gas breakdown by laser radiation	The final stage of optical breakdown	Continuous optical discharge

Plasma can be quantitatively characterized with set of parameters. Parameters of plasmas are: plasma temperature (the temperature of the whole plasma or temperature of the individual particles), concentration of the electrons (or degree of the ionization), concentration of the excited atoms, Debye radius, collision mean free path and plasma frequency. The external parameters are related to the characteristics of the power source which produced plasma: magnitude of the current, breakdown voltage and electrical conductivity of plasma. Parameters that are related to the composition of plasma are: thermal conductivity and viscosity.

Plasma state at a given point in space and at a moment of time is characterized by concentration of particles (electrons, ions, atoms, molecules and radicals) and with the distribution function for velocity and energy. When plasma is in the thermodynamic equilibrium (TE), it can be characterized as a state in which all species of particles from the volume have the same temperature T. In this case, the velocity distribution of each species of particles present in the same volume corresponds to the same temperature T [15]. In that case, the following assumptions are hold:

- the particle velocity distribution are Maxwell distributions;

- the particle energy distribution are Boltzmann distributions;

- the number of ions corresponds to the state of ionizing equilibrium - Saha equation;

- plasma radiated by Planck's law of radiation.

Plank's radiation law was almost never satisfied. In most plasmas, the thermodynamic equilibrium is local (LTE) due to the temperature gradient. The temperatures of these plasmas are in the range from 5000 K to 20000 K. These plasmas are weakly ionized or quasi-neutral. The equilibrium in plasma can also be partial. In that case, the electrons have higher temperature than other particles.

The Table 2.2 shows characteristic parameters of natural plasma.

Table 2.2: Parameters of natural plasma.

	Concentration [cm^{-3}]	Temperature [K]	Debye radius [cm]
The interior of the stars	$10^{23} - 10^{26}$	10^8	10^{-6}
Hot, dense plasma	10^{12}	10^6	10^{-2}
Hot, thin plasma	$10^{14} - 10^{16}$	10^6	10^{-4}
The solar crown	$10^6 - 10^8$	10^6	10
Interstellar gas	$1 - 10^2$	10^4	$10^3 - 10^4$
Interplanetary gas	$10^2 - 10^3$	10^4	$10 - 100$
Ionosphere, layer F	10^6	10^3	10^{-1}
Ionosphere, layer D	10^3	10^3	$1 - 10$

2.2 Plasma as a form of electric discharges in gases

The most common way to obtain plasma in laboratory conditions is by electrical discharges in gases. In these discharges, a certain percentage of the atom or gas molecule is in ionized state and working substance is at least in some discharge areas in the state of plasma. In the laboratory condition, plasma is generated as electric discharge in gases. The characteristics of plasma depend on many parameters. The first plasmas were produced in glass tubes at low pressures. Such plasmas were used for light.

For the lightning research, it is necessary to understand gas discharge mechanism in gases: Townsend and streamer mechanism and arc discharges.

Table 2.3: Parameters of laboratory plasmas.

	Concentration [cm^{-3}]	Temperature [K]	Debye radius [cm]
Fusion plasma	$10^{15} - 10^{17}$	10^8	10^{-3}
Theta pinch	$10^{16} - 10^{18}$	10^6	10^{-5}
Low pressure gas discharge	$10^9 - 10^{14}$	10^4	10^{-4}
Laser plasmas	$10^{20} - 10^{21}$	10^6	10^{-6}
Liquid Mercury	10^{23}	10^2	10^{-10}
Electrons in metals	10^{23}	10^3	10^{-10}

2.2.1 Mechanism of discharge in gases

All electrical processes in gases can be divided in two categories:

- *primary processes* - this category includes processes of gas ionization by electrons and ions and attachment of free electrons by electronegative molecules;

- *secondary processes* - these processes are of the crucial importance for the self-sustained discharge; They can be divided in two categories: the processes that are active on electrodes (photoemission, emission of electrons by ions and metastabiles) and the processes that are active in gases (ionization by positive ions, photoionization and ionization by metastabiles).

The electric breakdown in gases can occur according to two different physical mechanisms. The important question is whether dominant secondary processes of electrical discharge are in electrodes or in gases. If the dominant secondary processes are on electrodes, there is a Townsend breakdown mechanism. This is characteristic for very small interelectrode distances and low pressures. If is the dominant secondary processes are in gases, there is a streamer mechanism. This mechanism is characteristic for the discharges at the atmospheric pressure and for large distances between electrodes. The boundary between the Townsend and streamer discharge breakdown mechanism is not strict [12].

Townsend's avalanche coefficients play a key role in the theoretical modeling of the electric breakdown in gases. Townsend's coefficients are:

- *The Townsend first ionization coefficient α* - the number of ionizations produced by one electron per unit length in the direction of the electric field;

- *The Townsend second ionization coefficient β* - the number of ionizations produced by one ion per unit length in the opposite direction from the direction of the electric field;

- *The first Townsend coefficient η (attachment coefficient)* - expressing the number of attachment electrons per unit of path by electronegative molecules;

- *The second Townsend coefficient γ (ionization coefficient)* - the number of electrons extracted from the cathode as a result of the incidence of positive ion, photon, metastable atom or fast neutral atom;

These Townsend coefficients don't have constant value, but depend on the type of gas, electrical field and gas pressure. The second Townsend coefficient depends on the material of electrodes and topology of their surfaces [16].

2.2.2 Townsend breakdown mechanism

For laboratory research of gas discharge, the circuit shown in the Fig. 2.6, is commonly used. This circuit is especially used for the low pressure gas discharge experiments. The circuit consists: high power supply, discharge tube, high impedance resistor, voltmeter, ammeter, vacuum pump and manometer. The discharge tube consists of two electrodes, anode A and cathode K and a glass or metal cylinder filled with gas.

When the applied voltage on electrodes increase, the kinetic energy of electrons and ions in gases increase. This also increases due to the drift component of the electron and ions velocities towards the electrodes, in relation to the velocity of chaotic movement (kT) and the current increases due to recombination decrease. If it continues to increase the voltage between the electrodes, the energy of the initial electrons becomes large enough so that these electrons can perform ionization in the gas. According to the Townsend theory, per unit path of the initial electron in the direction of the electric field α, ion-electron pairs are formed. After the travelled path to the anode, an initial electron generates $n(x)$ new electrons, whose number on the next element of the path is augmented for dn:

$$dn(x) = n(x) \cdot \alpha \cdot dx. \tag{2.3}$$

When the Eq. (2.3) is solved, it adopted the number of free electrons $n(x)$ and positive ions $n^+(x)$ in the x point:

$$n(x) = e^{\alpha x}, n^+(x) = e^{\alpha x} - 1. \tag{2.4}$$
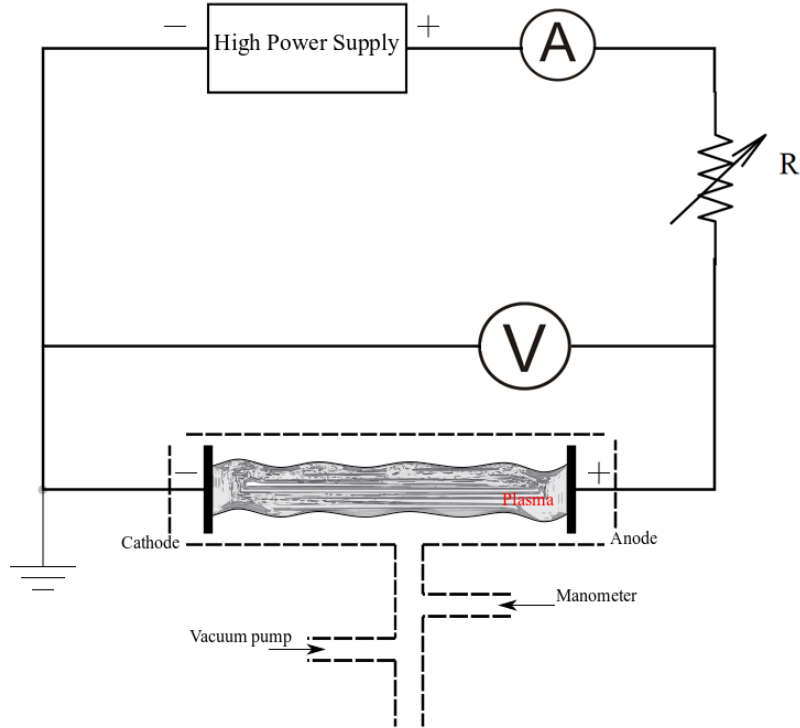
Figure 2.6: Equivalent circuit for the gas discharge at low pressure.

If the Townsend breakdown mechanism occurs in the gas, self-sustaining of the discharge process is based on the ion-induce secondary electron emission at cathode. According to this mechanism, at a time when the primary electron avalanche arrives to the anode, secondary mechanisms on the cathode generate $\gamma \cdot n^+(d)$ secondary initial electrons, illustrated in Fig. 2.7. This way, electron avalanche is generated and n electrons arrive at the anode, according to the Eq. (2.5):

$$n = \sum_{k=0}^{\infty} \left[\gamma \cdot \left(e^{\alpha d} - 1 \right) \right]^k \cdot e^{\alpha d}. \tag{2.5}$$

With the convergence condition of the series, the following expression is obtained:

$$n = \frac{e^{e^{\alpha d}}}{\left[1 - \gamma \cdot \left(e^{\alpha d} - 1 \right) \right]}. \tag{2.6}$$

It is obtained for the Townsend breakdown in gases from Eq. (2.6):

$$\gamma \cdot \left(e^{\alpha d} - 1 \right) = 1. \tag{2.7}$$

When performing the conditions for gas breakdown by the Townsend mechanism,
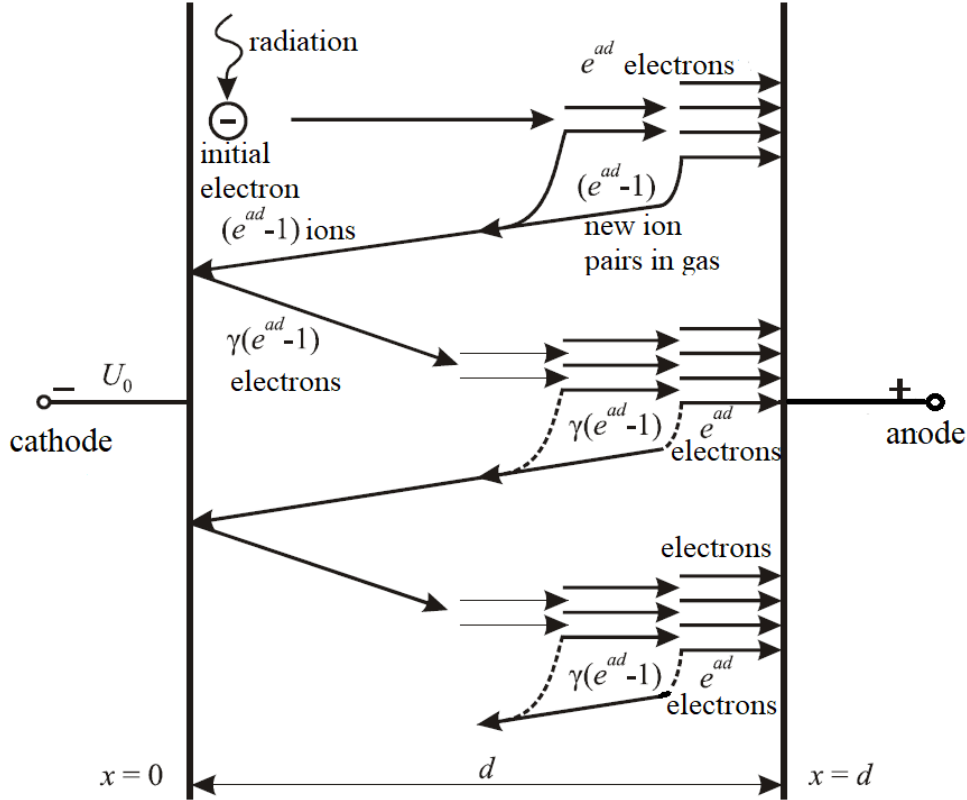
Figure 2.7: Townsend breakdown mechanism gases. Adapted from [16].

it is assumed that the initial electron at each mean free path takes the same amount of energy from the electric field. This assumption is justified only in the case of a homogeneous electric field. In case the electric field in the interelectrode space is not uniform, the condition for the Townsend breakdown mechanism is:

$$\gamma \cdot \int_0^d \alpha \cdot e^{\int_0^x \alpha \, dx} \, dx = 1. \tag{2.8}$$

It can be concluded that Townsend breakdown occurs in the moment when the concentration of the electrons originating from the primary avalanche is equal to the concentration of electrons caused by secondary electron processes [17].

The breakdown voltage in the gases V_b depends on the nature of the gas, the distances between electrodes d, material of electrodes and pressure of the gas p. The good variable for this research has always been a product of gas pressure and interelectrode gap distance (pd). Paschen's law can be derived analytically from mathematical description of the ignition condition. Paschen's law represents the equation for breakdown voltage (the voltage essential to initiate a discharge or electric arc) between two electrodes in a gas as a function of gas pressure and gap

length:

$$V_b = \frac{\mathrm{B}pd}{\ln(\mathrm{A}pd) - \ln\left[\ln\left(1 + \frac{1}{\gamma_{se}}\right)\right]}, \tag{2.9}$$

where pd is the product of pressure and distance (pressure is in Pascals and gap distance is in meters), γ_{se} is the secondary-electron-emission coefficient (the number of secondary electrons produced per incident positive ion) and A and B are the gas constants for calculating the first Townsend ionization coefficient. The constants A and B are experimentally determined and found to be constant over the restricted interval (E/p) for any gas. Paschen's law is tested in numerous experiments [17].
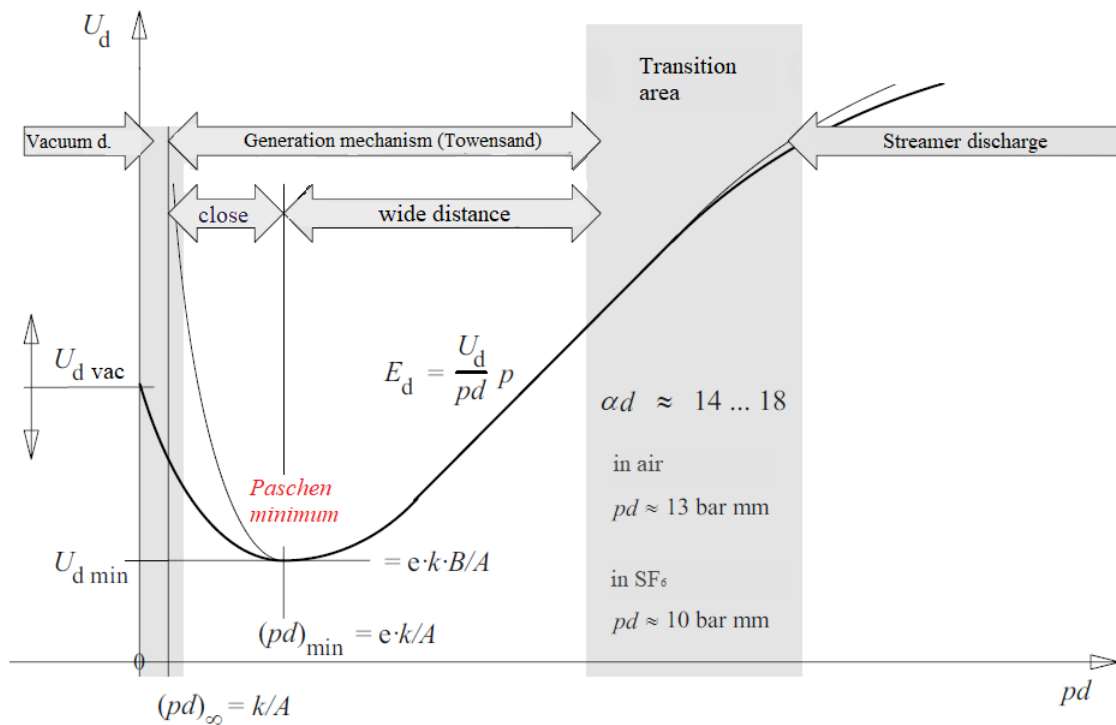
Figure 2.8: Paschen's Law as an analytically determined approximation function (thin curve) and as a real curve (bold curve). In the Figure A and B are gas constants, $k = \ln(1 + 1/\gamma)$ and e $= 2.718$.

Paschen's curve is shown in the Fig. 2.8 (the figure is drawn according to [17]). As can be seen in the Figure, the Paschen's curve characteristics have high values of the breakdown voltage at very *small* and very *large values pd*. In the middle there is a minimum that is called Paschen minimum and the gas breakdown occurs in the vicinity of the Paschen minimum. At low pd values, the breakdown voltage increases because a small number of collisions decrease the number of available molecules in the gas. High pd values mean big distances or high pressures. Large

distances cause reduction of field strength and thus reduction in the speed of the impact processes involved electrons. Large pressures cause greater acceleration of the available electrons, and therefore shorten the lengths of the free paths.

Mechanisms of electric breakdown in gases are explained theoretically. As it is said before, in normal condition, gas is insulator and does not conduct electricity. A very small amount of ion in the tube could be created by external ionizers - cosmic radiation or radioactive sources. If a small voltage is connected to the electrodes at this moment, a current would flow through the gas. This small current could be maintained as long as there is an external source of ionization. This current must be maintained by the external source of ionization and therefore such discharge called non-self-sustained discharge. In the region dark discharge, there is some ionization, but it is small. At low voltage, electricity is generated due to cosmic and ionizing radiation. The current magnitude is in the range between $10^{-12} - 10^{-6}$ A.
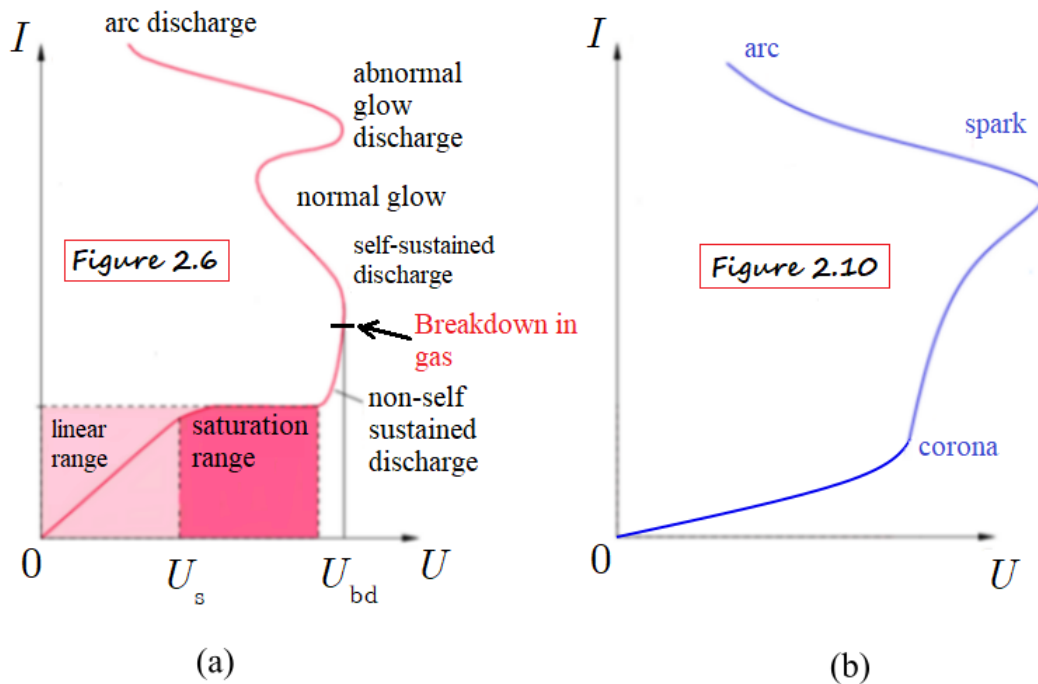
Figure 2.9: Voltage-current characteristics of electrical discharge in gases:(a) at low pressure and (b) atmospheric pressure.

The self-sustained discharge in gases is the discharge that occurs from the external source of ionization independently. This type of discharges is realized by multiplication of the existed number of the primary electron in gases and by emission of electrons from cathodes. These processes compensate the loss of electrons on the electrodes and in recombination. In this case, since flow of electricity through the gas is possible, it can be said that discharge process started. Glow discharges occur

when the breakdown voltage is reached. The voltage across the tube dropped and current increase approximately to the milliamps current range. Characteristic of normal glow discharge is that a voltage is constant, although the current changes. The plasma in the glow discharge is in the non-equilibrium state, and it is visible as a uniform glow column which is faint and cool. Electrons are emitted from cathode in the same way as in Townsend regime. Arc discharges are characterized by high current (in the ampere current range and higher), low voltage and low pressure. The arc column is typically loud, bright and hot. In arcs, electrons are emitted by the heating of the cathode.

2.2.3   Streamer breakdown mechanism

Townsend breakdown mechanism well describes the breakdown at low pressures very well. Namely, it is valid as long as the electric field of the electrons and ions space charges can be neglected compared to the ambient electric field [18]. Based on the experiments, it was confirmed that good agreement between theory and practice is up to $pd < 266.6447$ Pa m, and for higher values deviation is evident. At atmospheric pressure and for big interelectrode distances larger than 1 cm this theory can't exactly describe mechanism of breakdown.

The spark discharge occurs at the atmospheric pressure and at large interelectrode distances, in case when electric field is very strong. Spark discharge, unlike Townsend breakdown mechanism, means a break through the local narrow channel, without direct connection with the properties of the electrodes, and is characterized by very high currents ($10^4 - 10^5$ A). The concept of the spark channel is based on the streamer, the thin channel of the ionized gas formed from the primary avalanche in strong electric fields. Streamers between electrodes develop rapidly.

A spark discharge at high values of the parameter pd develops much faster than time needed to ion to pass through the cathode to secondary emission, so this breakdown is practically independent of the material from which the cathode was made. Loeb, Meek and Raether have set up a new theory of spark discharge [19]. Streamer is a thin ionization front that propagates through interelectrode space following primary electronic avalanche. A large number of secondary avalanches neutralize themselves on the streamer direction due to the photoionization of the gas and acceleration of the photoelectrons in the local electric field. Streamer starts its propagation from one high voltage electrode (cathode or anode). Active region in which processes of ionization, electron avalanche and emission of radiation occur is called *streamer head*. The electrode is connected to the streamers head by the streamers channel. A streamer is formed from an avalanche when the field of space
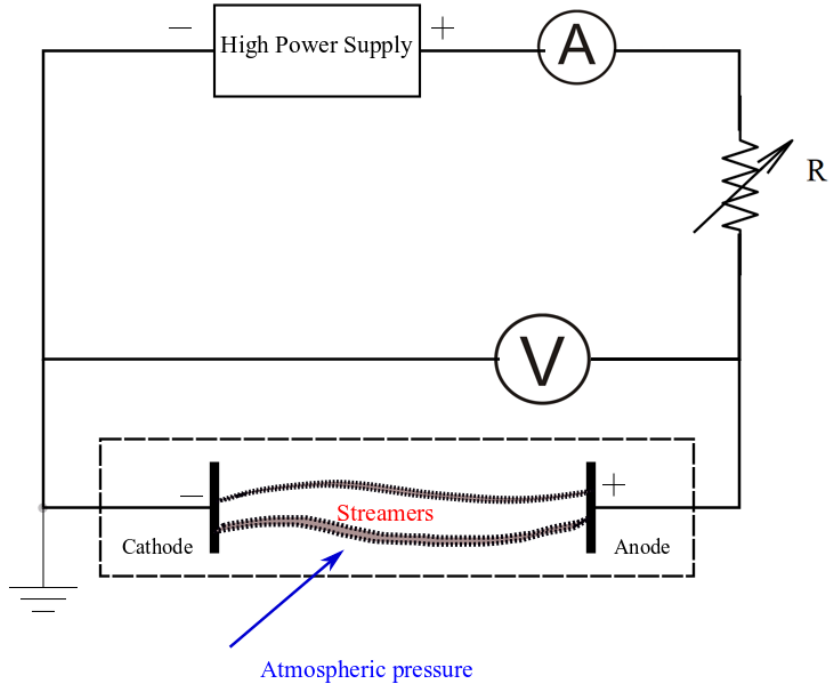
Figure 2.10: Electric circuit for the gas discharge at atmospheric pressure.

charge in the avalanche E_a reaches a value of the order of the external field order value E_0 [22]:

$$E_a = \frac{e}{4\pi\varepsilon_0 \cdot r_a^2} \cdot \left[\alpha\left(\frac{E_0}{p}\right) \cdot x\right] \approx E_0, \tag{2.10}$$

and it be marked as the criterion of streamer formation (r_a is the avalanche head radius and it can be expresses as $r_a \approx 1/\alpha$). The streamer propagation can be understood as a transition from an avalanche to a streamer that happens in the domain of the constant spatial-time progression of ionization processes. The onset of breakdown was identified in the Loeb-Meek theory with the event of streamer formation, but in practice it is not always so. It is important to notice well-known Meek's condition for the breakdown (empirical condition for streamer formation):

$$\alpha\left(\frac{E_0}{p}\right) \cdot d \approx 20, \tag{2.11}$$

From the condition (2.11), it follows that the streamers are not formed in gap with $d < 2.4$ mm, and the Townsend discharge probably happens. Thus, it has been shown that transformation from an avalanche to a streamer generally occurs when the charge within the avalanche head reaches critical value of:

$$N_e = \exp(\alpha d) \approx 3 \times 10^{18}. \tag{2.12}$$

In the theory of gas discharges, there are two type of streamers: *cathode-direct*, positive and anode-direct, negative streamers [23]. Positive streamers propagate in electric field direction and negative streamers propagate in the opposite direction. In case of positive streamers, i.e., electrons from ionizing domains drift into the conducting channel, which leads to a slight increase in concentration of electrons and reduction of the electric field in the channel. Also, in positive streamer, radial diffusion of electrons is compensated with its radial drift in the opposite direction, i.e., to the conduction zone, so that an additional source of an electron is not necessary Fig. 2.11. Unlike them, electrons in the negative streamers are transported forward, into the region of lower electronic concentration which contributes to the reduction of the electric field, and thus obstructs the progression of the streamer. Also, in the case of a negative streamer, radial diffusion and drift drain electrons from the channel of the streamer. This requires the strength axial electric field in this part of the streamer as sufficient for the ionization that will compensate for the loss of electrons. The main differences between positive and negative streamers are [20]:

- maximum of the electron concentration in positive streamer is considerably higher than negative streamer;

- positive streamers have twice high velocity than the negative streamers in the same condition;

- electric field in the head of positive streamer is considerably larger than the field in the head negative streamer.

In the process of avalanche development, the number of electrons and positive ions increases continuously. As the number of electrons in the avalanche head increases, the intensity at the avalanche front increases (Fig. 2.12). The potential is reduced on the tail of the avalanche. The electrons in the head of the avalanche are stopped and can be recombined with the ions. In recombination, emitted photons are able to ionize neutral molecules near the tail of the primary avalanche, forming secondary avalanches.

Secondary avalanches, following the electric field lines and having an excess negative charge (electrons) on the head, are drawn into the area of positive volumetric charge left by the primary avalanche. The electrons of the secondary avalanches mix with the positive ions of the primary avalanche and form a streamer — an
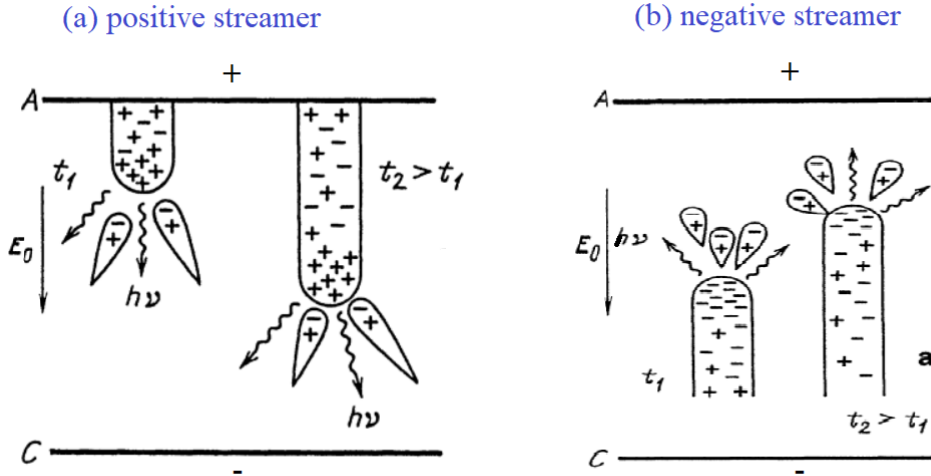
Figure 2.11: Positive and negative streamers. Adapted from [14].

area with the highest current density, which, by warming up, begins to glow and the highest concentration of particles (current density) is formed near the cathode. For photoionization in the gas volume, the photon energy must be larger than the ionization energy. This process is successfully carried out in mixtures of gases containing components with relatively low ionization energy, including air (cathode bombardment with positive ions is effective at low gas pressures). The criterion for the transition of an avalanche discharge into a streamer is the critical number of electrons in an avalanche as shown in Eq. (2.12). The minimum electric field (E_+) required for positive streamer propagation in air at standard temperature and pressure (STP) has been measured between 400 and 440 kV/m [21]. Schematic diagram of positive streamers propagation was prepared according to [25] and it is shown in Fig. 2.12. Note that the streamer channels cannot conduct a high current.

The behavior of the streamer channel is quantitatively described through the following parameters [14]:

- The stream channel is in weakly ionized plasma state. The conductivity of streamer channel $\sigma \sim 10^{-16} \cdot n_e/p$ [atm] Ohm^{-1}cm^{-1}. For example, at $p = 1$ atm and $n_e \sim 10^{13}$ cm^{-3} the conductivity of the streamer channel is $\sigma \sim 10^{-3}$ Ohm^{-1}cm^{-1};

- if the channel diameter is $2r_c \sim 1$mm and the field in it $E \sim 10$kV/cm, the current in the channel is $i \sim 10^{-2}$A;
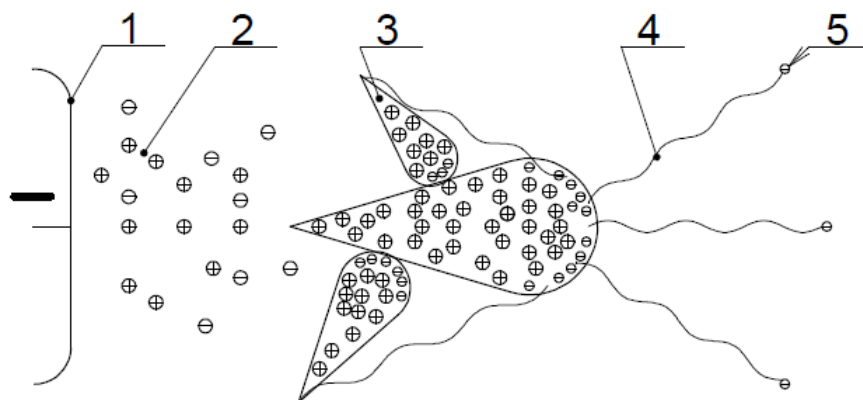
Figure 2.12: Mechanism of cathode streamer development: 1-cathode (electrode), 2 - streamer channel, 3 - avalanches, 4 -photon motion, 5 - electron from photoionization processes. Adapted from [25].

The formation of the spark is going through the streamer. Streamer discharge (also known as filament discharge) is type of transient electric discharge. Theoretically, the transition from streamer (weakly ionized plasma) to spark discharge (highly ionized plasma) will be explained in a simplified way. When one streamer arrives at the cathode, the interelectrode gap is closed by the streamer, the conductivity of the channel increases rapidly and current "flows" through the channel. This current causes thermal ionization in the streamer channel by the Joule's effect, whereby the high-resistant streamer goes into plasma state. In that moment, the spark channel is formed, breakdown is complete and the discharge starts. It can be said that the lightning is an example of *huge* spark discharge at the atmospheric pressure in the Earth's atmosphere.

Plasma in the spark channel is highly ionized and highly conductive. Breakdown in this case is follow by very strong crack in the form of a shock wave. In fact, as time passes, spark channel rapidly expands in the space because it ionizes the surrounding air by rapid heating. In spark discharge it releases the significant energy and it can have destructive effect on reactor electrodes. The behavior of the spark channel is quantitatively described through the following parameters [14]:

- the temperature in the spark channel reaches 20000 K (1800 eV);

- the electron density in the channel is around $n_e \sim 10^{17}$ cm^{-3} ;

- the electron conductivity of the channel is $\sigma \sim 10^2$ Ohm^{-1}cm^{-1} and the electric field inside the channel is $E \sim 10^2$ V/cm;

- the maximum current is $i \sim 10^4 - 10^5$ A;

- the maximum current density is $j \sim 10^4$ A/cm^2;

These are basic pieces of information about spark discharge. Further information about this type of discharges has been given in the Drabkina studies of spark discharge [39]. Depending on the gas pressure, the electrode gap and the electrode configuration, several discharge regimes can be distinguished. With an increase of voltage at the atmospheric pressure, a corona discharge appears first and quickly goes into the spark discharge. Spark discharge is just a transient process and it will easily pass into an arc discharge at atmospheric pressure (Fig. 2.11).

2.3 Arc discharge

Generally, arc discharge occurs at atmospheric pressures or more high pressures. The processes that occurs at electrodes (secondary processes) are more important for the mechanism of discharge than the processes of the ionization of gas by electrons (primary processes), because at high pressures an electron between two collisions can not collect enough energy for ionization. Typically for arc discharge there is: low voltage on electrodes, high current density, high current magnitude and high temperature. Cathode is often hot and in this case it emits electrons by the mechanisms of thermal emission and under the influence of the strong electric field. In the case of arc discharge, the gas is in the state of plasma (arc plasma on the atmospheric pressure is isothermal - LTE) and cathode fall of potential is small (about 10V). When considering electric arcs, static and dynamic arcs can be distinguished. Static arc can be established using DC circuits and it will be further described in detail.

In arc theory, there are different classifications of arc discharge. According to Friedman, there are the following types of arcs [22]:

- hot thermionic cathode arcs;

- arcs with hot cathode spots;

- vacuum arcs;

- high pressure arcs;

- low pressure arc discharge.

High pressure arc will be described in this chapter because their physical characteristics (current, voltage, temperature, and electron density) are the most connected with the physical characteristics of lightning. In this type of arc discharges, 80-90 % of the discharge energy is converted into heat.

During the arc discharge, the cathode is very hot and the thermionic emission is expressed. Namely, in the transition regime from abnormal to arc discharge, when the voltage on the electrodes increases, the current in the gas also increases, cathode temperature increases and thus the number of electrons emitted due to thermionic emission. Transition area to the arc discharge occurs when the number of electrons generated by thermoelectric emission becomes approximately equal to the number of electrons generated by the secondary emission.

Further increase in voltage leads to current increase and discharge goes into the arc discharge where dominant process is the thermoelectric emission. It causes a small voltage drop at the cathode. This cathode fall of potential occurs at a distance from the cathode that is equal to the mean free path of the electrons. Cathode and anode fall of potential are small and they are in the order of ionization potential of the gas in which discharge occurs. Considering a small distance at which the cathode potential drop is realized, the electric field near the cathode is very strong and comes to the emission of electrons from the cathode due to strong electric field. These two mechanisms in the gas produce electrons that are necessary to maintain the discharge. The cathode current magnitude is equal to the current magnitude of the entire discharge. The high temperature of the cathode during discharge resulted in evaporation and erosion of cathode material [24].

This is a theoretical approach that explains how to get arc plasma from glow discharge. In practice, the arcs are produced directly. A typical example of this is the electric arc during welding. This example of the arc will be taken into consideration during the discussion of the electrical characteristics.

The electrical properties of the arc are determined by the processes occurring in three characteristic zones - the column and in near-electrode regions of the arc (cathode and anode) which are located between the arc column on one side and the electrode and the products on the other [25].

The positive column occupies the largest part of the space between the electrodes and is in the state of plasma. Process in the positive column depends on the gas pressure. For example, at low pressures, the discharge fills the entire discharge line. Gas remains cold, while the electron temperature is very high. At higher pressures, the positive column forms a cylinder, whose diameter is smaller than the diameter of the gas tube. It should be noted that the diameter of the positive column is inversely proportional to the pressure of the gas $D \sim 1/p^{\delta}$ (where the δ is constant which depends on the nature of the gas). Column diameter is not constant throughout the length and slightly wider in the vicinity of the cathode [26]. Due to increased frequency of the collision in this case, the gas and electronic temperatures

are equalized and it is a state that is close to thermal equilibrium. The arc column is electrically neutral. In any of its cross sections, there is the same number of charged particles of opposite signs. The length of the arc column on average reaches 10 mm, which corresponds to approximately 99 % of the arc length. The cathode and anode regions are characterized by a very short extension - about 0.0001 mm for the cathode region, which corresponds to the mean free path of the ion, and 0.001 mm for the anode, which corresponds to the mean free path of the electron.

Temperature of the gas is higher than in the case of low pressure arc discharge (Fig. 2.13). The thermal ionization is the dominant and the temperature in the gas column is very high. The highest temperature is in the axis of the arc (the arc can be understood as one cylinder, and the temperature drops radially to the periphery, so the balance is also referred as "local"). The radial gradient of the temperature depends on the arc current and the pressure of the gas. This gradient is related to the density of free charge and collision frequency. The density of the charged particles in the axis of the arc is in the range values of $10^{12} - 10^{17}$ cm^{-3} and the degree of ionization is close to 100 %. Arc plasma is high-energy plasma and it is characterized by a great enthalpy. The temperature in anode region (in welding process) with a consumable electrode is about $2500 - 4000$ °C, the temperature in the arc column is from $7000 - 8000$ °C, and in the cathode region $9000 - 12000$ °C.
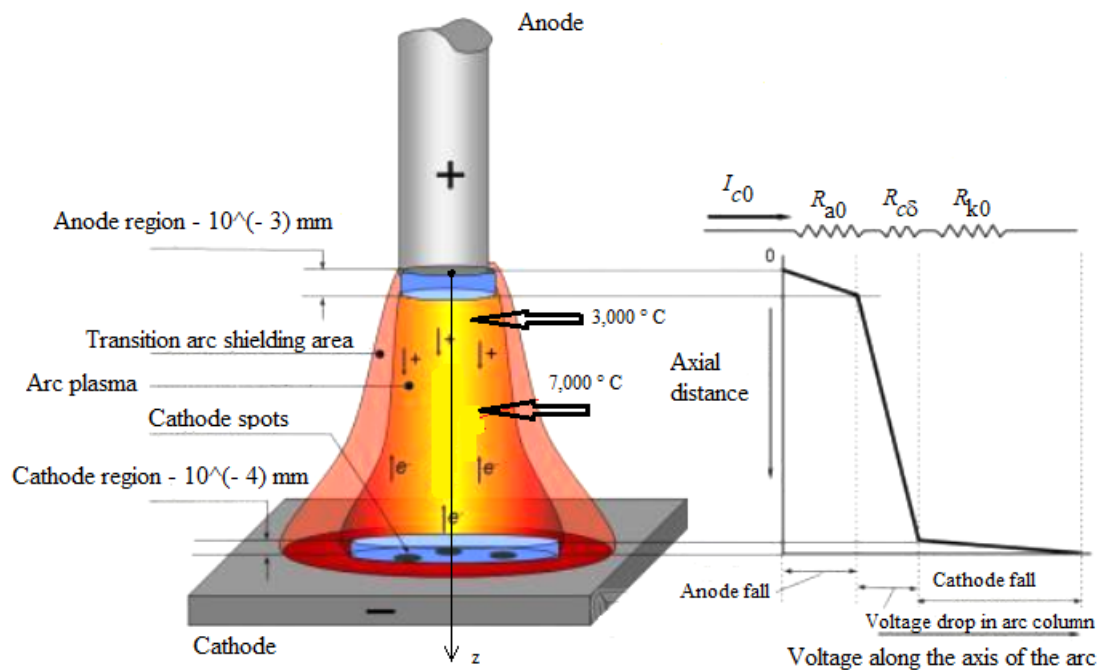
Figure 2.13: Geometry and properties of electric arc.

There are voltage drops in the near-anode and in the near-cathode regions: the cathodic U_k and anodic U_a (Fig. 2.13). It can be seen that a gradient of potential along the arc and the voltage drop in the arc column is proportional to its length as in equation:

$$U_d = U_k + U_a + I \cdot E. \tag{2.13}$$

The gradient is approximately constant along the column and reaches from 100 to 200 V/cm. The magnitude of this voltage drop depends on the materials of the electrodes and on the gas (15V - 30V). The voltage drop across the arc itself exceeds a few volts. The rest of the voltage falls on the cathode and anode regions of the arc. Linear increase indicates that the arc column is uniform with a constant longitudinal electric field E.

The longitudinal electric field depends on the arc current magnitude ($E = B/i^z$, B and z are constants; B depends on the type of gas and z depends on anode material) and gas pressure ($E \sim p^y$, y is constant depends on the nature of the gas). Due to the relatively low intensity of the electric field, considered only single ionization can exist. It follows that arc column is electrically neutral, because in any of its cross sections are the same numbers of charged particles of opposite signs. Thus, the electric field in the arc column lies in the range from 0.1 to 1.0 V/mm.

The total current density can be expressed as:

$$j = (e \cdot n_e \cdot \mu_e + e \cdot n_i \cdot \mu_i) \cdot E, \tag{2.14}$$

where n_e and n_i are concentrations of electrons and ions, μ_e and μ_i are mobility of electrons and ions, respectively and E is the axial electric field. Current density and temperature have the highest values on the axis of the electric arc and in its vicinity. If mobility of the ion that is significantly less than the mobility of the electrons ($\mu_i << \mu_e$) is ignored from Eq. (2.14), the electron concentration can be expressed as:

$$n_e = \frac{j}{e \cdot \mu_e \cdot E}. \tag{2.15}$$

In the Fig. 2.13 axial and radial characteristics of electric arc are shown.

For arc stability, arc voltage and current must have a definite relationship between each other. This relationship is known as the static volt-ampere characteristic of the arc and its typical shape is shown in Fig. 2.14. The volt-ampere characteristic has three characteristic regions: (1) drooping or negative volt-ampere characteristic (approximately from 1-100 A), (2) flat volt-ampere characteristics (approximately
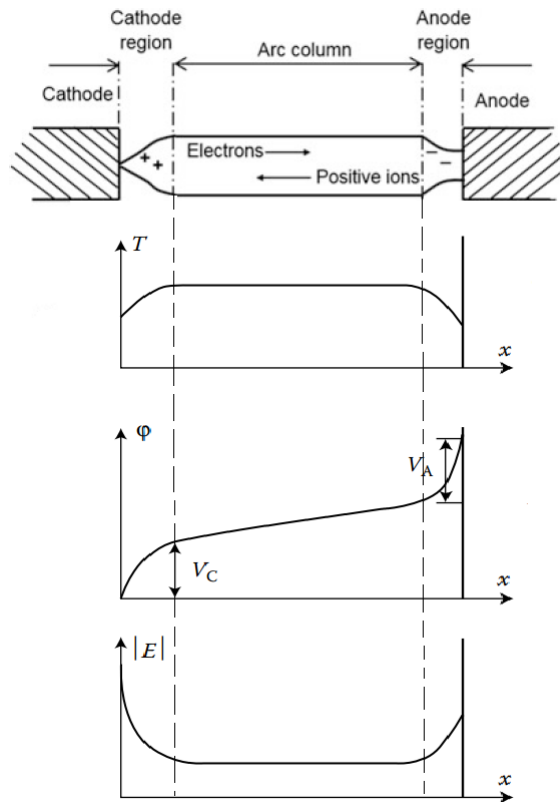
Figure 2.14: Characteristic parameters for arc discharge.

from 100-1000 A) and (3) rising volt-ampere characteristics (approximately more than 1000 A). Static U-I characteristic of an argon shielded tungsten arc for normally used welding current range of up to about 300A and for the arc length range of 1 to 16 mm is shown in Fig. 2.15. It is clearly evident that the static volt - ampere characteristic for such an arc between the workable ranges is very slightly rising in nature.
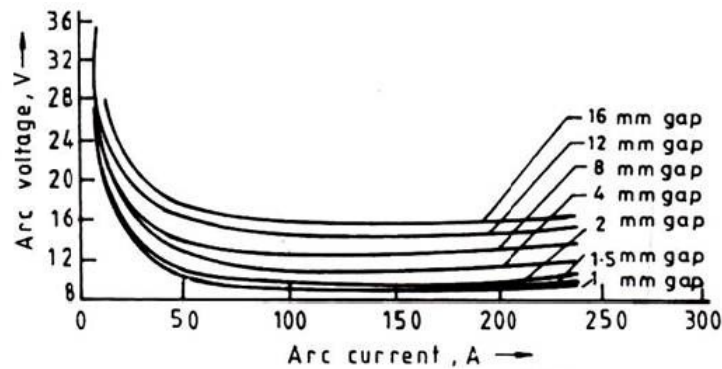
Figure 2.15: Volt-ampere characteristic of the arc depending on parameters.

Numerical simulations of the electric arc are very complex. It should be noted that the reference [27] exemplifies the research carried out in a fine way for numerical arc simulation. The commercial simulation software ANSYS CFX is used for a rotationally symmetric steady-state model of a gas metal arc. Current numerical models of gas metal arc welding (GMAW) are trying to combine magnetohydrodynamics (MHD) models of the arc and volume of fluid (VoF) models of metal transfer. They neglect vaporization and assume an argon atmosphere for the arc region, as it is common practice for models of gas tungsten arc welding (GTAW). For the calculation of the electric current density, resistive heating and pinch force in the droplet, VoF-based models either use heat and electric current flux boundary conditions or are combined with an arc model that has been developed and tested for tungsten inert gas (TIG) arcs. They are based on magnetohydrodynamics (MHD) and assume a single-component fluid of argon in a state of a local thermodynamic equilibrium (LTE). The results of the simulation of the arc are shown in the Fig. 2.16.
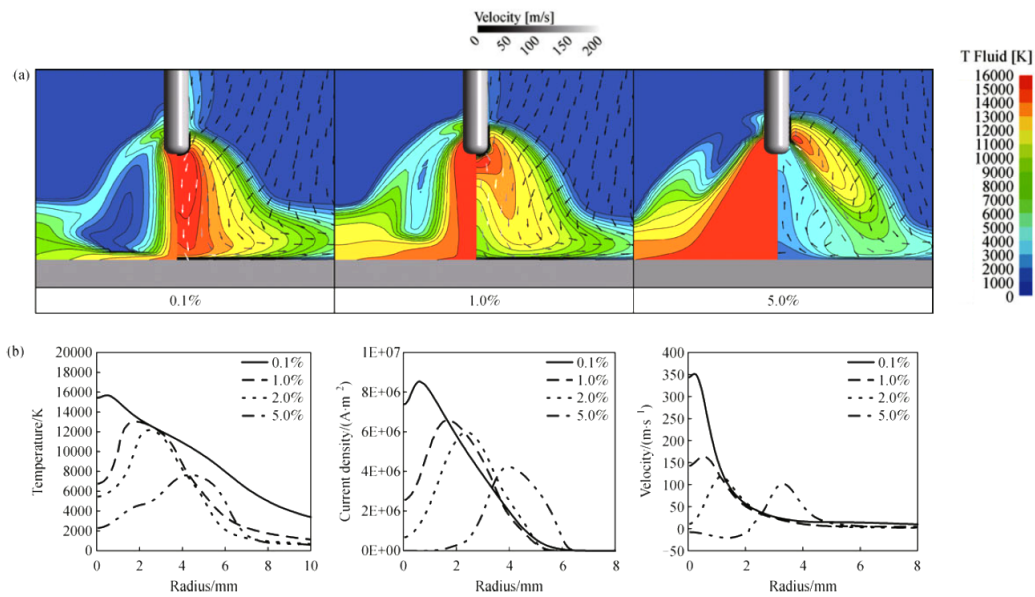
Figure 2.16: Result of the arc simulation: (a) the temperature distribution and flow vectors (right) and metal vapour mass fraction distribution (left), images are scaled and sized; (b) radial distributions of temperature, current density and downward velocity at a position of 1.5 mm above the workpiece. Adapted from [27].

At the end of the study [27], the model predictions are compared to the arc temperature measurements and high-speed video images.

The general conclusion for arc is that there is no need to maintain the discharge if the discharge takes place at atmospheric pressure and low interelectrode distances. It can be said that this case leads to distortion and instability of the positive column.
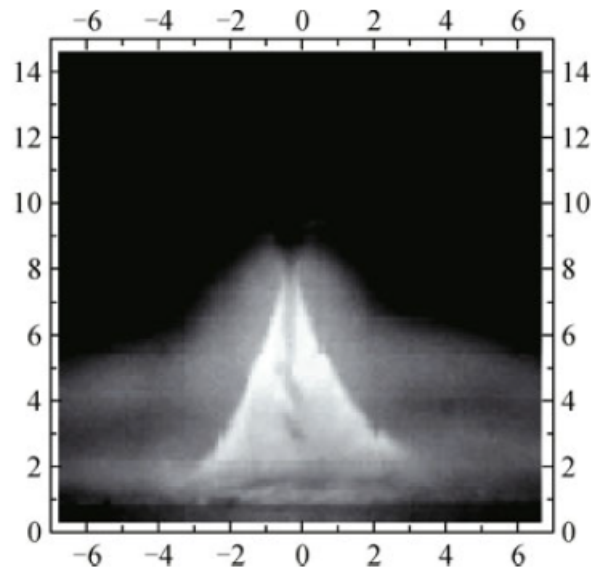
Figure 2.17: Arc in practice. Adapted from [27].

Because of this, the arc is stable. The types of stabe arcs are:

- temporal and spatial stabilized arcs;

- magnetically stabilized arcs;

- gas-stabilized arcs;

- wall-stabilized arcs;

2.3.1 Lightning - Electric arc in the earth atmosphere

Lightning can be understood as long electric arc in earth atmosphere. A lightning channel is composed of thermal plasma, which can be treated as a fluid with high current density. Lightning discharge usually starts with corona inception, and subsequently develops into plasma channel due to the Joule heating effect, which results from the high intensity of the electric field near the avalanche.

Basic theoretical assumptions for the lightning study were taken from the literature and are presented in Chapter 3. Radiation from lightning produces light in the form of black body radiation. The voltage difference between the clouds and the ground is 200MV or more, while the maximum discharge current is about $50 - 100$ kA. The total duration of the lightning flashes vary from the 0.1 to 0.6 s and the temperature in the lightning channel increases up to the 28000 K, while the density of the electron reaches 10^{24} m^3. Because of the sudden heating of the lightning

channel and the physical processes inside the lightning channel, the air pressure is changed and it causes thunder. Lightning emits the visible light, broad spectra of radio frequencies, X-rays, gamma rays and the particles of the antimatter. For the detail study of lightning physics, especially for the study of the evolution of the lightning channel, there is a need for good knowledge of fluid dynamics, electrodynamics and gas discharge physic.

The physical process of return stroke is quite complicated and yet, not fully clear. For a detailed simulation of the lightning discharge, it is necessary to take all of the processes into account. The simulation of the physical processes in the lightning channel is much more complex than the simulation of an electric arc.

The aim of this dissertation is to obtain a quantitative and qualitative picture of physical processes in lightning the channel, based on a simple, engineering approach.

Chapter 3

The Physics of the Lightning discharge and lightning channel modeling

In this chapter, the basis things about the lightning discharge physics and the physical structure of the lightning channel will be given. Also, a detailed overview of engineering models that will be used in the calculation of the dynamic of the lightning channel and the electric field inside the lightning channel will be presented.

3.1 Physical structure of the Lightning Channel

For a brief remainder, the charge distribution deposited in the channel of the step and dart leader was the subject of many studies. The specific data for the step leader line charge vary from 0.7 mC/m to 30 mC/m. Dart leaders consist of less charge than the step leaders.

Scientists use a Baum and Cooray model for the charge modeling in the channel of the dart leader. The Baum's model of charge distribution of the dart leader before the return stroke assumes that the corona envelope is in the form of the reverse circular cone, a few tens of meters in the bottom of the channel [28]. The charge density in the Baum's model is zero at the ground and increase linear with height. Basically, the model consideres the lightning channel as a pre-charged transmission line. The Baum model gives good results in terms of charge distribution very close to the ground, but the speed of the leader does not fully comply with the experiment. However, the radial distribution of the charge density in the corona sheath of the dart leader before the return stroke remains unknown. It was assumed that this distribution is similar to the distribution formed in the corona discharge in the

coaxial or cylindrical geometry in the laboratory.

In theoretical study of the leader, Cooray applied quasi-static (electrostatic) approach [29]. Unlike Baum's model, the electrostatic model of the dart leader is modeled as vertical wire above the ground without charge in corona sheath in a certain diameter. It is assumed that the electric field is homogeneous and the charge density of the dart leader should increase linearly down to ground, except at the last few meters above the ground. The linear distribution calculation of the charge based on quasi-stationary principle doesn not provide the exact result because of the high speed of the leader. Mistakes are more evident as the top of the leader when it approaches the ground. So, in terms of charge distribution Baum's model yields better results than the Cooray model.

The charge distribution along the lightning channel before the return stroke play a crucial role in the generating of a channel-base current as well as in the corona sheath dynamic during the discharges. Theoretically, the physical structure of a leader during a return stroke should be as follows: the lightning channel is modeled by a negatively charged corona sheath that stretches around a thin, very conductive central core, Fig. 3.1. It is assumed that the most carrier of the charge is located in the corona envelope whose radius is several meters and the high-conducting core of the channel is estimated to be one centimeter that conducts all axial current. The channel charge generates strong horizontal and vertical electric field.
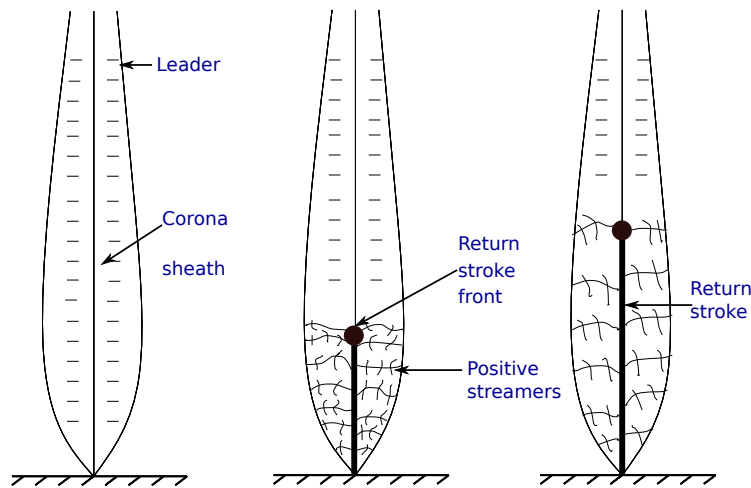
Figure 3.1: Structure of the lightning channel.

When the negatively charged step leader come near to the ground surface, electric field between the head of the leader and the ground is greatly enhanced. At a time when the leader goes to the object close enough, an upward discharge that moves towards the cloud is initiated from the object. Encounter with the downward leader

comes at some points above the ground and then the return stroke starts.

Golde [52] was a scientist whose experimental results in the field of lightning were very noticeable in the first half of the twentieth century. He was the first scientist who published a photography of the connecting leader and return stroke and that connection was at 15 to 30 meters above ground. The longitudinal field potential of the top of the leader is from 10 to 100 MV/m and the return stroke speed is between 10^8 m/s and $3 \cdot 10^8$ m/s. At the time of connection, negatively charged leader is short-circuited with ground. The wave front of the return stroke is in the place where the potential of channel is equal to the potential of the ground. At that place the electric field is very strong. As the length of the wave front is estimated to the several meters based on the photography of the return stroke, it follows that the field strength is in the order of tens of megavolts.

The propagation of the wave front is taken place as in Fig. 3.2. The total current in the channel consists of the electrons which causes the ions to be very slow because of their big masses. Electrons from the ionized part of the channel go into the ground and create current from the ground to the cloud. The current magnitude can be measured on the ground surface.
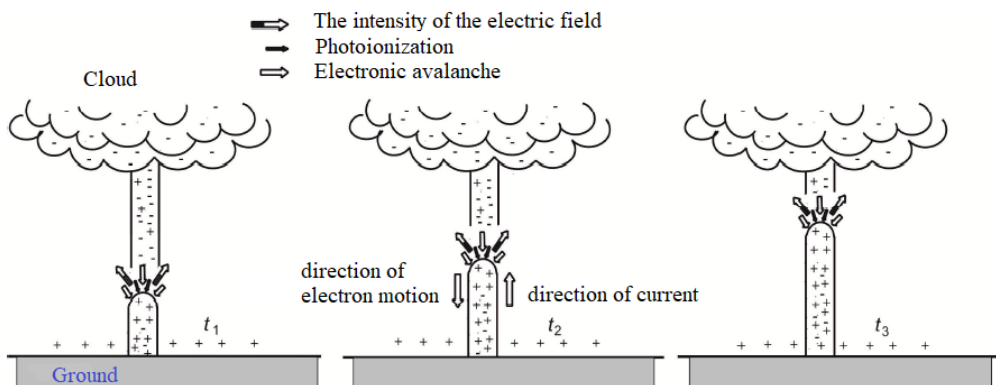
Figure 3.2: The propagation of the wave front of the return stroke. Adapted from [60].

It was established that the velocity of the return stroke decreases with height, while the speed of the next return strokes is less dependent on the height [30]. Schonland considered that a return stroke is slower in the older parts of channel [30].

In the theory of the return stroke, there is a hypothesis that predicts that the lightning channel consist of the high-conductive central core and the corona sheath surrounding. In this case one can expect that the return stroke will move along the

core. The most important question is how the charge transports from the corona envelope to the core of the lightning channel (in the radius of the order of several centimeters) since the compression of the charge is opposed by the electrostatic repulsive forces. Two theories were given by Wagner and Hileman [31] and Pierce and Wormell [32].

According to the first theory, the filament discharges between the core and the corona envelope lead the charge to the core for less than a microsecond [31]. They predict a significant reduction of the charge in the corona envelope during the return stroke phase. Their theory is most similar to TCS model, which anticipates instant removal of the charge from the corona sheath.

According to the second theoretical approach, the reduction of the charge in the envelope takes time of the order of microsecond, but mechanism of discharging is totally different [32]. They consider that the core is on the ground potential because of its high conductivity, while the corona envelope is on the potential of the cloud. This large potential difference produces the radial corona currents with a maximum value of 1 kA and the duration time of one microsecond. Many authors connect this decrease with linear pinch effect [30], [33]. Namely, it is considered that the return stroke current is established in the channel which diameter is about a few meters and after that the channel is compressed due to the pinch effect. Some calculations show disagreement with this standpoint [34]. If one takes into account that magnetic pressure for the channel of radius 1m is 1 bar, required current is very high and its magnitude is the order of 10^6 A, which is too high value (magnetic pressure on the channel surface is proportional to the $\sqrt{I/r}$).

The leader and return stroke currents are established in the narrow channel core. Assuming that the channel consists of the core and the envelope then the core is in equilibrium with the surrounding air. Therefore, the core is on the atmospheric pressure of the environment. The return stroke transfers energy to the channel core for a very short time. The core temperature and pressure rapidly increase. The charge particle density in the core also increases because of the processes of ionization and dissociation during the return stroke phase. The temperature of the channel during the return stroke phase is 30000 K and pressure at that moment is about 10 bar. After this phase, the temperature decreases to the 3000K. It is assumed that at this moment the pinch effect becomes very significant. For example, if a current magnitude of 80 kA is in the channel, on the surface of the channel whose radius is about 1cm, the pressure of 10 bars will be appear. For the same effects in the channel whose radius is about 0.1cm, a current of 8 kA is required.

This is the very high magnitude of the current for given radius. The channel

is expanding as long as the pressure in the channel does not equalize with the environment. The expansion of the channel takes place at supersonic speed. It produces a cylindrical shock wave that is heard as a sound effect of discharge. This effect is heard as a thunder when the shock wave speed is reduced to the speed of sound. Expansion of the shock wave lasts 5 to 10 µs. As the wave spreads, the density of the gas in the channel decreases almost. All energy is spent on the gas expansion. Evidence of the channel existence, previously described, is obtained by spectroscopic pressure measurements in the experiments with long sparks in air [36] and in many experiments with the expansion channel of the spark discharge [37], [38] and [39].

After the phase of the shock wave when the expansion of the channel is completed, the channel comes into the state of the balance of its pressure with the environment [40]. Laboratory experiments show that the current density is stabilized at 10^7 A/m². This value is for two orders of magnitude greater than the value of current density in the electric arc in air. At that moment the channel expands slowly and the current density has a tendency towards a value that is characteristic for the stable arc.

The good physical model for the lightning discharge should include the following assumptions:

1. *The channel of the lightning discharge consists of a core and corona envelope. The core of the channel is high conductive and the main axial current flow through it*;

2. *The return stroke moves along the core and initiates the breakdown in the corona envelope on same height. The velocity of the return stroke v decreases with height and it is more or less constant for following strokes*;

3. *Generation of the radial currents is not instantaneous and it depends on height and conductivity of the channel*;

4. *The carrier concentration in the channel is the function versus time and height*;

5. *The distribution of the charge deposited in the channel, determined the current at a given height*;

6. *It is necessary to take into account the influence of the ground conductivity on channel dynamics*;

Also, a good model of the lightning discharge should provide a clear physical interpretation of processes during the atmospheric discharge. The physical processes in

the lightning channel are very complex and for some of their characteristics experimental data are still unknown. Many models have been developed to describe the channel dynamics.

Each model requires certain approximations, and thus it notes more or less from physical reality. That's why scientists consistently compare experimental data to their models. Base on this comparison, they improve their models.

In theory of return strokes, there are four types of lightning models:

- *Gas dynamics models*;

- *Electromagnetic models*;

- *Distributed circuit models*;

- *Engineering models*.

Gas dynamics and engineering models are useful to describe the evolution of the lightning channel.

3.2   Gas dynamics models

The first models that were used for studying the evolution of lightning channel are gas dynamics models. Gas dynamic models describe the physical behavior of a short segment of a cylindrical plasma column. In order to get the results for these models, three gas dynamics equations (which represent the conservation of mass, momentum and energy) are usually solved coupled to the two equations of state with assume input parameter - current versus time. The main output models include temperature, pressure and mass density as a function of radial coordinate and time.

The first gas dynamics model was developed to describe the dynamics of the plasma in the spark discharges and these models later were applied in the study of lightning return strokes. This chapter provides short overview of several models from this group.

Drabkina (1951) developed the first gas dynamic model [39]. She studied the radial evolution of a spark channel and its associated shock wave as a function of the time-dependent energy injected into the channel. She assumed that the spark channel pressure is much higher than the pressure of the environment. That approximation is called "strong-shock" approximation. Following this "strong-shock" approximation, Braginski (1958) developed the spark channel model describing the time-variation parameters such as radius, temperature and pressure as a function of input

current [41]. Braginski obtained formula for channel radius: $r(t) \approx 9.35 \cdot \sqrt[3]{I(t)} \cdot \sqrt{t}$, where $r(t)$ is in centimeters, $I(t)$ is in amperes and t in seconds. Braginski (1958) set the electrical conductivity σ of the channel at 2.24×10^{-4} Sm^{-1} and assumed the ambient air density is 1.29×10^{-3} gcm^{-3}. For a known $r(t)$, resistance per unit channel is $R(t) = [\sigma \pi r^2(t)]^{-1}$ and the input energy is $W = \int_0^t I^2(\tau)R(\tau)d\tau$.

Hill's gas dynamic model (1971) starts from the following assumption: the plasma column is straight and cylindrically symmetrical, the algebraic sum of all positive and negative charges in any volume is zero and local thermodynamic equilibrium exists at all times [42]. Initial condition that characterize the lightning channel (with radius of 1mm and temperature of 10^4 K) are:

- *The input current is about 20 kA in the first few microseconds, and after that in the next 10-20 microseconds decreases;*

- *The pressure is equal to ambient pressure;*

- *The density of plasma in the channel is equal to the density of ambient.*

For Hill's model it is necessary to define electric energy of sources and radiation energy sources. Electric energy deposited in the channel is defined as follows: the plasma column consists of several sub-zones in which the gas parameters are constant. For known temperature and density, the conductivity can be calculated using the Plooster's equation. After that, the energy that heats the channel for each of the sub-zones should be calculated. The energy deposited in the channel is spent on heating, ionization and expansion of the channel.

About 50 years ago, Plooster developed the 1D gas dynamic model of the return stroke with coupled hydrodynamics and a radiation model based on an emission term only [44, 45]. The advanced model is given by Paxton et al. [46, 47]. That model use Euler equation coupled with P1 diffusion model [48] for computing spectrally dependent radiation of the air plasma. The results from those studies for temperature, density, pressure and longitudinal electric conductivity as a function of radius in five different moments of time are shown in Fig. 3.3.

Dubovoy (1991) in his model includes pinch effect due to interaction of a current with its own magnetic field [43]. In this case, it is necessary to calculate Lorentz's force that is in the opposite with the dynamic spread of the gas.

Validation of gas dynamic models is done on the basis of the comparison of theoretical results given by the model with experimental results in the laboratory for long spark. For example, the input energy of return strokes that predicts different gas dynamics model is derived from comparison of optical radiation that produces the lightning channel with radiation of long sparks produced in the laboratory.
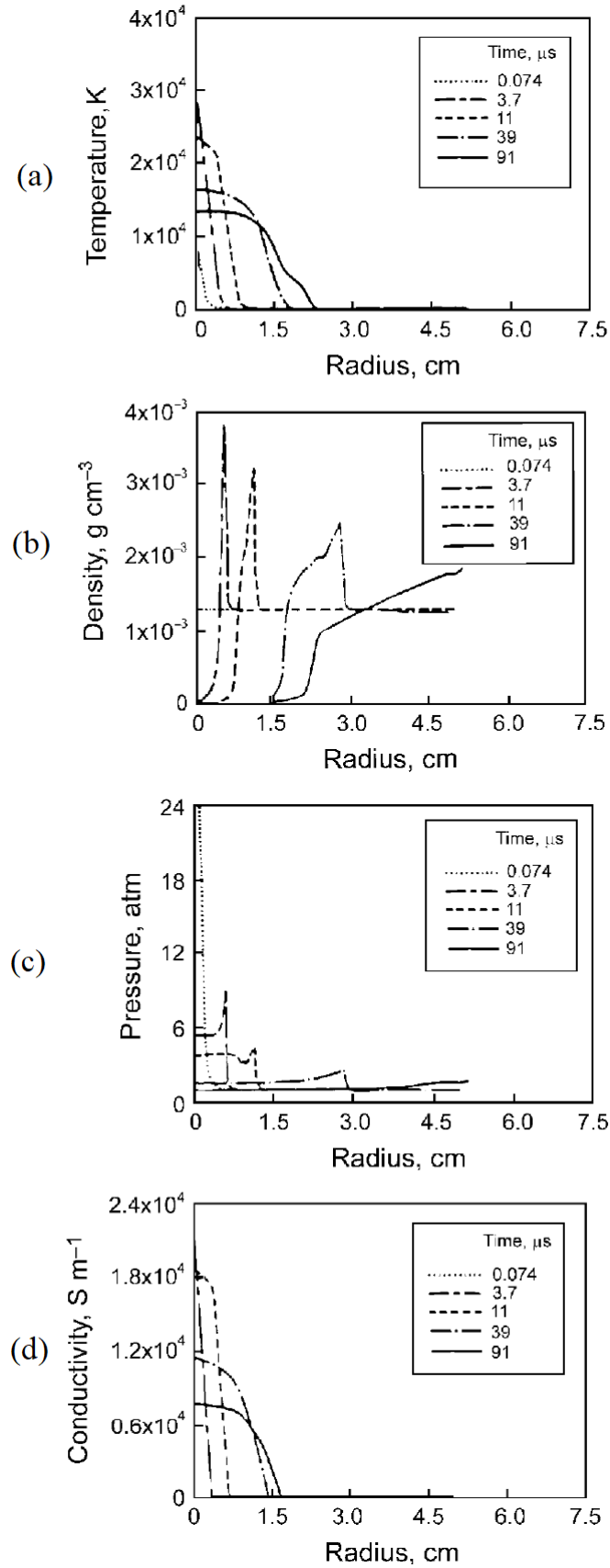
Figure 3.3: Physical characteristics of plasma channel versus radius at five instants of time: (a) Temperature, (b) Density, (c) Pressure, (d) Conductivity. Adapted from [46], [47].

Gas dynamic models can be used for the simulation of gas dynamics of the lightning return strokes, detailed air chemistry and accurate air radiation transport. These models allow great opportunities for lightning studies, but this complex mixture of hydrodynamics, chemistry and radiative transport is not yet understandable in detail.

3.3 Engineering return stroke models

Numerous return stroke models have been developed with the aim of enabling numerical calculation of the radiated lightning electromagnetic pulse and describing the physics of the gaseous-discharge processes in the lightning channel.

It is obvious that gas dynamic models can be useful for studying of plasma channel evolution, while electromagnetic models and distributed circuit models cannot be useful in this situation. The engineering models are used for study the evolution of the lightning plasma channel, primarily because of their simplicity. *It is supposed, in this study, that the physical structure of the lightning channel and all physical mechanisms related to the physics of electrical discharges are the same in the natural and triggered lightning.*

The engineering return stroke models can be divided into two categories, the Transmission-Line-Type Models (TLM, also called current propagation models) and Traveling-Current-Source-Type Models (TCSM, also known as current generation models).

The latest TCS model is the GTCS model. This is the general model from which all other TCS models can be derived as special cases. The extension of the GTCS model is a GTCS model with the current reflections from the ground.

3.4 Transmission line type models (TLM)

In these groups of models the return stroke channel serves as a guiding structure for the propagation of the return stroke current wave, which is injected in the channel base. The current wave travels upwards with a certain speed (usually assumed to be one third of the speed of the light), while its amplitude may decrease with height depending on the model. Models from this category are:

- Original transmission line model - **TL model** (proposed by Uman and McLain [35])

- Modified transmission line model with linear current decay with height - **MTLL model** (proposed by Rakov and Dulzon [49])

- Modified transmission line model with exponential current decay with height - **MTLE model** (proposed by Nucci [50])

- Modified transmission line model with parabolic current decay with height - **MTLP model** (proposed by Rakov and Dulzon [51]).

3.4.1 TL model

TL model of the lightning discharge starts from the assumption that the lightning channel is an ideal conductor (vertical, right, uncharged and infinitely conductive) and the current impulse propagates thought it with a constant speed. This speed was measured experimentally and it is equal to c/3. In the TL model, it is assumed the speed of the current pulse that is less than the speed of the light without any physical explanation. Namely, the channel is highly conductive structure and the wave should propagate through the channel with the speed of the light. The current at same height $i(z,t)$ has the same waveform as channel-base current $i_0(0,t)$, but it is delayed for the time that is required the current wave front to reach from the ground to the height z. The mathematical expression for the channel-base current $i_0(t)$ is adopted from the experimental measurements. The magnitude of the current on the same height z in time t is given by the dependence:

$$i(z,t) = i_0(t - z/v)u(t - z/v) \tag{3.1}$$

and the time is calculated from the moment when the return stroke starts. In Eq. (3.1), u is the Heaviside function and v is speed of the return stroke wave front. It can be concluded that, the current waveform at the striking point is assumed to propagate upward with a constant speed without any distortion or attenuation.

If it is accepted that τ is some instant of time when the discharge of the channel stops, then it is $\rho_L(z,t)$ is zero. If the equation of continuity and the basic equation of electromagnetism are used, the expression for the line chare density above and below the wave front is obtained [60]:

$$\rho_L(z,t) = \begin{cases} \dfrac{-i_0(\tau - z/v)}{v} & , H \geq z > vt \\ \dfrac{i_0(t - z/v)}{v} - \dfrac{i_0(\tau - z/v)}{v} & , z \leq vt. \end{cases} \tag{3.2}$$

In the Fig. 3.4 line charge density into the lightning channel versus height is shown. At the end of the lightning discharge, the total amount of the electricity in the channel should be zero.

If it is assumed this model of the atmospheric discharge with the lumped circuit as in the electric circuit theory, the channel-base current would be model with a fixed current generator in the base of the channel. The internal resistance of the source is infinity, so the grounding resistance is also infinity.
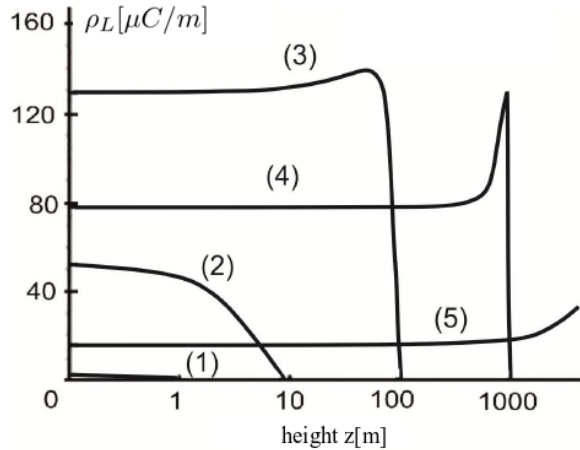
Figure 3.4: Line charge density put into the lightning channel depending on height. Standard parameters for negative cloud to ground lightning current according to Eq. (3.2) are used. The time is parameter whose values are: (1) $t = 10^{-8}$ s, (2) $t = 10^{-7}$ s, (3) $t = 10^{-6}$ s, (4) $t = 10^{-5}$ s, (5) $t = 10^{-4}$ s. Adapted from [60].

Briefly, this model is very simple, but it contains many flaws and some uncertainties. The Fig. 3.4 shows the line charge density in the lightning channel at different heights. The current parameters are given in the Tab. 3.6.

3.4.2   Master-Uman-Lin-Standler (MULS) Model

After the first measurements of magnetic field and the current magnitudes on the high towers, the first data indicated that multiple components in the channel-base current exist. Lin et al. defined three components at the striking point [61]. He started from the TL model with an ideal current generator in the channel base and suggested the first modification of the TL model. According to the modified model of the discharge, the channel-base current can be separated into three component, the breakdown impulse current i_p , the corona current i_c and the uniform current I_u, Fig. 3.5. Each of these components can be separated from the measurements of the near and far fields performed simultaneously.

3. The Physics of the Lightning discharge and lightning channel modeling

1. The breakdown current i_p. The breakdown current is the current of the electric breakdown on the place of the current wave front of the return stroke. This current is established in a channel previously created by a leader and it is responsible for the peak of the electric and magnetic fields in the first microseconds. The relation between these components of the current and the radial component of the magnetic induction on the large distance from the striking point is given by the expression (the arc approximation is used $r >> H$) [53]:

$$i_p = \frac{2\pi cr}{\mu_0 v} B_\phi\left(t + \frac{r}{c}\right) \tag{3.3}$$

where: v the speed of the return stroke wave front, c the speed of the light, B_ϕ magnetic induction and r is distance from the striking point. In the literature, it is considered that the impulse of the pulse current is moving with a constant speed. The shape of this impulse does not change, but maximum decreases with the altitude [62]:

$$i_p(z,t) = \begin{cases} i_p(0, t - z/v) \cdot e^{-z/\lambda_p}, & H > z > vt \\ \\ 0, & z \leq vt. \end{cases} \tag{3.4}$$

2. The corona current i_c. The corona current is the component of the current that is established in the corona sheath with the direction towards to core and further towards to ground. It is caused by the discharge of the charge which is deposited in the corona sheath and flowing after the breakdown current i_p. This current due to the corona source at altitude z is:

$$i_c = I_0(e^{\alpha t} - e^{\beta t}) \tag{3.5}$$

where: z is the altitude of the observed part of the channel, t the moment of time (must be $z \leq vt$) and v the speed of the wave front (the wave front must reach a certain height in order to establish the corona current). Parameters in Eq. (3.4) are: $I_0 = 21$ A, $\lambda = 1500$ m, $\alpha = 10^5$ s^{-1} and $\beta = 3 \times 10^6$ s. The total charge deposited in the corona envelope of the lightning channel which generates the current is about 0.3 mC. The height of the channel is 7.5 km.

3. The uniform current I_u . The uniform current I_u is most likely a continuation of the continuous current of the previous leader. This component is responsible for the constant increase in the electric field observed in measurements. This current can be expressed in the form:

$$I_u = \frac{2\pi\varepsilon_0 \cdot (H^2 + r^2)^{3/2}}{H} \cdot \frac{dE_{close}(r,t)}{dt} \tag{3.6}$$

where: H altitude of the channel, t a moment of time, r radial distance from the channel and E_{close} close electric field (r is equal from 1 to 10 km) as reported in [61]. The magnitude of the continual current is 3.1 kA.

The overview of the current component is given in the Fig. 3.5.
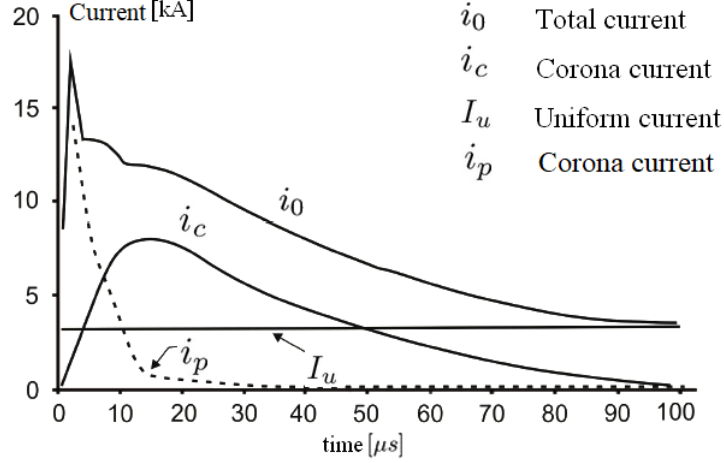
Figure 3.5: Components of the channel-base current in the striking point estimated from the measured fields from typical return strokes according to Lin et al. model from 1980 [61].

Lin et al. model has the same disadvantage as the TL model. This modifications is very important because of the splitting the current in the components. These separations are also accepted in some other models.

3.4.3   MTLL, MTLE and MTLP models

Uman and Jordan show that the impulse breakdown decreases with height. Following this result, Rakov and Dulson made modification of the TL model, proposing the TL model with linear decrease of the current with height - **MTLL model** [49]. The current magnitude was expressed mathematically in the form:

$$i(z,t) = \begin{cases} P(z) \cdot i(0, t - z/v) & , H > z > vt \\ 0 & , z \leq vt. \end{cases} \tag{3.7}$$

where H is the total channel height. In the Eq. (3.7), parameter $P(z)$ is the current attenuation factor and its value is $P(z) = 1 - z/H$.

After this model, Nuci et al. proposed modified TL model with the exponential attenuation current versus height - **MTLE model** [50]. The current magnitude is the same as in Eq. (3.7), but with the different atenuation factor $P(z) = e^{-z/\lambda}$.

The last model from the TL family of engineering return stroke models is the model proposed by Rakov and Dulson - **MTLP model** [51]. The current attenuation factor for this model is $P(z) = (1 - z/H)^2$.

3.4.4 Overview of the TL models

In the Table 3.1, an overview of the current for all mentioned TL models is given. The current attenuation factor $P(z)$ is noted in the table with blue color. Also, in the Table 3.2 it is given an overview of the line charge density for all mentioned TL models. It is adopted the following expression in these tables:

$Q(z,t) = \int_{z/v}^{t} I(0, \tau - z/v) d\tau$, $v = v_f = const$, $H = const$ and $\lambda = const$.

Table 3.1: The current along the channel according to the TL models, $t \geq z/v$.

Model	Current
TL Model Uman and McLain (1969)	$i(z,t) = i(0, t - z/v)$
MTLL model Rakov and Dulzon (1987)	$i(z,t) = i(0, t - z/v) \cdot (1 - z/H)$
MTLE model Nucci et al. (1989)	$i(z,t) = i(0, t - z/v) \cdot e^{-z/\lambda}$
MTLP model Rakov and Dulzon (1991)	$i(z,t) = i(0, t - z/v) \cdot (1 - z/H)^2$

Table 3.2: The line charge density along the channel according to the TL models, $t \geq z/v$.

Model	Line charge density
TL Model Uman and McLain (1969)	$\rho_L(z,t) = \dfrac{i(0, t - z/v)}{v}$
MTLL model Rakov and Dulzon (1987)	$\rho_L(z,t) = (1 - z/H) \cdot \dfrac{i(0, t - z/v)}{v} + \dfrac{Q(z,t)}{H}$
MTLE model Nucci et al. (1989)	$\rho_L(z,t) = e^{-z/\lambda} \cdot \dfrac{i(0, t - z/v)}{v} + e^{-z/\lambda} \cdot \dfrac{Q(z,t)}{H}$

3.5   Traveling-current-source-type of models (TCS)

The TCS models represent the return stroke process as a current source that propagates upwards, injecting the current pulse on its way into the channel. In other words, the channel itself produces the current pulse as a product of charge neutralization in the corona sheath, positioned around the central core of the leader channel. The models from this category are:

- Bruce-Golde Model - **BG model** (proposed by Bruce and Golde [52]);

- Original travelling current source model - **TCS model** (proposed by Heidler [55]);

- Diendorfer-Uman Model - **DU model** (proposed by Diendorfer and Uman [57]).

In addition to these, the generalized lightning travelling current source return stroke model (GTCS) was established as a generalization of all TCS models [58]. The BG, TCS, DU and the MDU models result from the GTCS, as its distinct subvariants. Within the GTCS model, the channel-base current, the leader line charge distribution, and the return stroke speed are known (can be measured) functions. These functions determine the so-called channel discharge function [59].

3.5.1   Bruce-Golde Model - BG Model

This is the first model that was successfully used for the return stroke modeling and the calculation of the lightning electromagnetic impulse. This model can be classified in the TCS model group, and its modified version is a precursor of the TCS model. The BG model is proposed by Bruce and Golde (1941) based on the experimental observation of the lightning return strokes [52]. This model proposes analytical expression for the current and the velocity of the first return stroke.

BG model suggests the double exponential form of the current at ground:

$$i(t) = i_0 \big[e^{-\alpha t} - e^{-\beta t} \big], \tag{3.8}$$

where $i(t)$ is the current at the base of the return stroke at instant of time t. The constants have the values: $i_0 = 30000$ A, $\alpha = 4.4 \times 10^4 \mathrm{s}^{-1}$ and $\beta = 4.6 \times 10^5 \mathrm{s}^{-1}$. In order to simplify the approach, the authors used a simple expression for the current along the channel in the BG model:

$$i(z,t) = \begin{cases} i(0,t), & z \le vt \\ i(0,t), & z > vt. \end{cases} \tag{3.9}$$

From the Eq. (3.9), it can be concluded that the current bellow the wave front is the same as in the striking point of the first return stroke. This is very simplified, but therefore this model is not physically reasonable. Also, current has the discontinuity at the place of the wave front. The current that characterized the BG model along the channel is shown in Fig. 3.9.

The velocity of the first return stroke is representing by:

$$V_t = V_0 \cdot e^{-\gamma t}, \tag{3.10}$$

where $V_0 = 8 \times 10^7 \text{m/s}$ and $\gamma = 3 \cdot 10^4 \text{s}^{-1}$ [53]. This velocity profile was recorded by Schonland [54]. The model is very simple and it is not useful for the calculation of the LEMP (Lightning electromagnetic pulse). As a result of this assumption, there is an instantaneous charge transfer from the base of the channel to the tip of the return stroke. Also, Bruce and Golde introduce of the dipole moment M as:

$$\frac{dM}{dt} = 2i_t \int_0^t V_t dt = \frac{2i_0 V_0}{\gamma} \cdot \left[e^{-\alpha t} - e^{-\beta t}\right] \cdot \left[1 - e^{-\gamma t}\right], \tag{3.11}$$

From the Eq. (3.11), the spectrum of the first and subsequent return strokes can obtained. The resulting spectra peak for the first return stroke is 9 kHz for the first stroke and 7 kHz for second return stroke [63].

Dennis and Pierce (1964) modified the BG model developing the DP model [64]. They assumed the current bellow the wave front in the form:

$$i = i_0 \left[e^{(-\alpha(t-z/u))} - e^{(-\beta(t-z/u))}\right], \tag{3.12}$$

where z is the altitude of the channel and v is the velocity of the current wave front. Also, they assumed that the current above wave front is equal to zero. Within the DP model there is no a discontinuity of the current at the place of the wave front like in the BG model (expect for $u = V$). This model can be reduced to BG model if $u \Rightarrow \infty$. Dennis and Pierce speculated with values $u = V_0$ ($V_0 = 8 \cdot 10^7 \text{m/s}$), $u = \text{c}$ ($\text{c} = 3 \cdot 10^8 \text{m/s}$) and $u \Rightarrow \infty$. In their final model, they adopted $u = \text{c}$ and they used values $\gamma = 3 \cdot 10^4 \text{ s}^{-1}$ (for the first return stroke) and $\gamma = 0$ (for subsequent return strokes). It is very important to mention that the measured radiated field is different for the TL, the BG and the DP models [53]. Because of that, these models are improved through different modified return stroke models.

3.5.2 Traveling Current Source Model - TCS Model

The TCS Model of the return stroke was developed by Heidler in 1985 [55]. According to this model, the current is generated along the channel at the place of the wave front, so that the channel is electrically discharged during the return stroke. Electric discharge of the part of the corona sheath at a certain height z occurs when a small amount of electricity from that part of the channel activates when the return stroke comes. It directs the charge to the core of the channel and from there the charge flows to the ground. The part of the channel above this current source is not discharged and the part of the channel bellow this current source, towards to ground becomes highly conductive. According to the TCS model, the current wave from the source moves to the ground without attenuation, with the speed of the light c. In this model, the generation of the current is instant, and the time discharge constant is equal to zero.

According to the TCS model, the current magnitude on some height z and in the time moment t is expressed by means of:

$$i(z,t) = i_0(t + z/\text{c})u(t - z/\text{c}), \tag{3.13}$$

where i_0 is the magnitude of the channel-base current, u is the Heaviside unit function and v is the speed of the current source.

The time needed for the wave to come from height z to the ground is z/c, while the current source needs the time z/v to reach the same height. On the basis of this attitude and Eq. (3.13), it can be concluded that the current function at the same height z, has a different form in relation to the channel-base current at $z = 0$. From the Eq. (3.13) it can be also seen that the current has a discontinuity at the place of the current source. Just before the arrival of the return stroke wave front at the moment of time $\tau = z/v$ the current magnitude is zero, and after the return stroke wave front had passed, the current is $i_0(\tau + z/\text{c})$. The time derivative of current is a Dirac delta function due to this discontinuity are outing one of the disadvantages of the derived TCS model. This derivative is used for the calculation the radiation components of the electric and magnetic field.

From the continuity equation and the expression for the current according the TCS model, the expression for the line charge density is obtained:

$$\rho_L(z,t) = \begin{cases} \dfrac{i_0(\tau + z/\text{c})}{\text{c}} - \dfrac{i_0(z/v^*)}{v^*}, & H > z > vt \\[2mm] \dfrac{i_0(\tau + z/\text{c})}{\text{c}} - \dfrac{i_0(t + z/\text{c})}{\text{c}}, & z \leq vt. \end{cases} \tag{3.14}$$
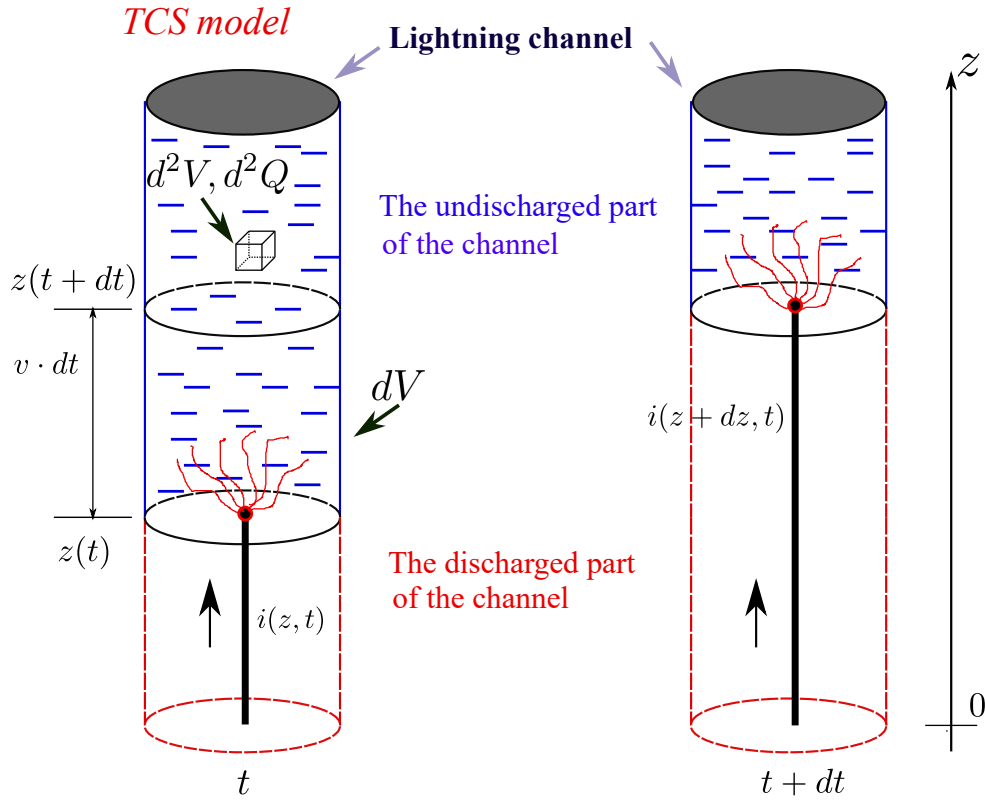
Figure 3.6: Lightning channel discharge during return stroke according to the TCS model. Adapted from [60].
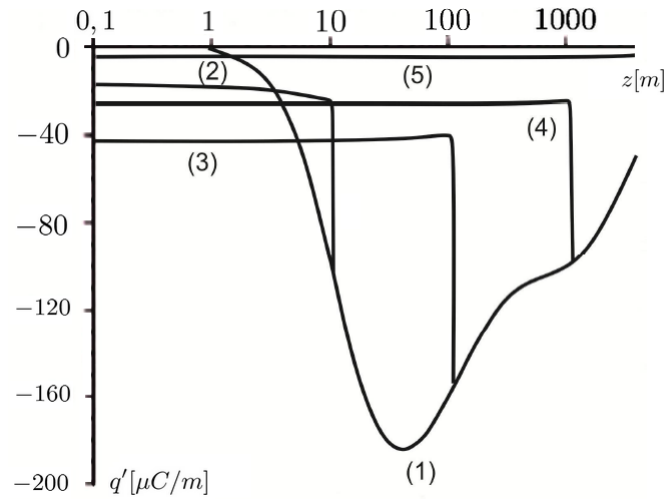
Figure 3.7: Line charge density function versus height in the lightning channel during the return stroke phase according to the TCS model. Time is taken as a parameter: (1) $t_1 = 10^{-8}$ s, (2) $t_2 = 10^{-7}$ s, (3) $t_3 = 10^{-6}$ s, (4) $t_4 = 10^{-5}$ s, (5) $t_5 = 10^{-4}$ s. Adapted from [60].

It can be concluded from Eq. (3.14) that the line charge density function and the current function have a discontinuity at the moment $t = z/v$. This is clearly shown in Fig. 3.7. The current parameters are given in the Tab. 3.6.

Compared to the TL model, the TCS model has the following advantages:

1. *Physical explanation of the processes in the channel during discharge*;

2. *Line charge density is in a better agreement with the experiments*;

3. *Maximum of the breakdown current decreases with height*;

4. *It enabls the modeling of the current reflections from the ground. This is not possible in TL type of models.*

Disadvantages of the the TCS model are:

1. *Discontinuities of the line charge density function and the current function at the place of the wave front exists. The current discontinuities cause the terms with the Dirac delta function in the expressions for electric and magnetic field in the far field zone*;

2. *The maximum of the line charge density moves with the return stroke wave front during the return stroke phase*;

3. *The absolute maximum of the line charge density in the channel is about* 0.2 *mC/m which is much lower than the experimental average value of the* 1 *mC/m* .

3.5.3 Diendorfer-Uman Model (DU Model)

In order to avoid the discontinuities of the current, it was necessary to modify the TCS model. Modification of the TCS model was carried out in [56]. The modification consists of introducing the time-discharge constant. That time is denoted as τ_d and it is considered as depended from the height of the channel.

Two components of the channel-base current are introduced in this model: breakdown i_{bd} and the corona current i_{co}. The breakdown time discharge constant is also defined as $\tau_{d_{bd}}$. This constant is of the order of magnitude lower than the corona time discharge constant $\tau_{d_{co}}$.

Discharging of the line channel charge in the channel takes place according to the following exponntial decay:

$$q'_{DU}(z,t) = q'_0(z,t) \cdot \mathrm{e}^{-\frac{t-z/v}{\tau_d}},\qquad(3.15)$$
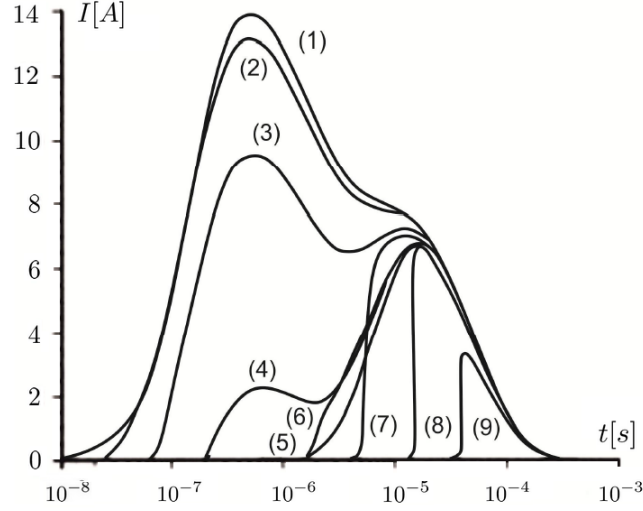
Figure 3.8: Current versus time according to the DU model. Height z is taken as a parameter: (1) $z_1 = 0, 1$ m, (2) $z_2 = 2, 4$ m, (3) $z_3 = 6, 9$ m, (4) $z_4 = 20$ m, (5) $z_5 = 58$ m, (6) $z_6 = 167$ m, (7) $z_7 = 480$ m, (8) $z_8 = 1386$ m, (9) $z_9 = 4000$ m. The current parameters are given in the Tab. 3.6. Adapted from [65].

where q'_0 is the line charge density immediately prior to the beginning of the discharge. Using the equation of continuity, the time and height dependence of the current is obtained:

$$i(z,t) = \left[i_0(t + z/\text{c}) - i_0(z/v^*) \cdot e^{-\left(\frac{t - z/v}{\tau_d} \right)} \right]. \tag{3.16}$$

It can be seen From Eq. (3.16) that there is an additional current component compared to the current predicted by TCS model in Eq. (3.13). The current discontinuities in terms that existed in the original TCS model are eliminated. The expression for the current is the continuous function at the place of the wave front. Fig. 3.12 shows the dependence of the current magnitude versus time for different channel heights. The current consists of the breakdown and the corona current. The magnitude of the breakdown current is dominant up to 10 meters height. At altitudes above 50 meters, breakdown current practically disappears and at these heights the corona current is dominant.

3.5.4   Overview of the TCS models

An overview of the current for all mentioned TCS models is presented in the Table 3.3. Also, in the Table 3.4, the overview of the line charge density for all mentioned TCS models is given. The so-called reduced speed is given by: $v^* = v_f/(1 + v_f/\text{c})$, $v = v_f{=}const$ and $\tau_D{=}const$.

Table 3.3: The current along the channel according to the TCS type of models, $t \geq z/v$.

Model	Current
BG Model Bruce and Golde 1941	$i(z,t) = i(0,t)$
TCS model Heidler 1987	$i(z,t) = i(0, t + z/\text{c})$
DU model Diendorfer and Uman 1990	$i(z,t) = i(0, t + z/\text{c}) - e^{-(t-z/v_f)\tau_D^{-1}} i(0, z/v^*)$

Table 3.4: The line charge density along the channel according the TCS type of models, $t \geq z/v$.

Model	Line charge density
BG Model Bruce and Golde 1941	$\rho_L(z,t) = \dfrac{i(0, z/v_f)}{v_f}$
TCS model Heidler 1987	$\rho_L = -\dfrac{i(0, t + z/\text{c})}{\text{c}} + \dfrac{i(0, z/v)}{v^*}$
DU model Diendorfer and Uman 1990	$\rho_L = -\dfrac{i(0, t + z/\text{c})}{\text{c}} +$ $e^{-(t-z/v_f)\tau_D^{-1}} \left[\dfrac{i(0, z/v^*)}{v_f} + \dfrac{\tau_D}{v_f} \dfrac{i(0, z/v^*)}{v_f} \right] +$ $\dfrac{i(0, z/v^*)}{v^*} + \dfrac{\tau_D}{v^*} \dfrac{di(0, z/v^*)}{dt}$

3.6   Overview of the engineering models

In this chapter, several different models of the return stroke are presented. The main disadvantages of these models are:

1. *The line charge density in the channel depends on the channel-base current. In order to properly analyze the processes in the channel, it is necessary to separate these quantities. After that, these functions should be independently modeled according to the experimental data;*

2. *In previous models discontinuities appear in the radiated electromagnetic field;*

3. *The assumption of instant discharge (TCS model) and exponential discharge (DU model) of the channel part are not physically real;*

4. *It is not possible to take into account the affects of the ground conductivity and ground proximity during the discharge;*

5. *It is not possible to distinguish the first from the subsequent return strokes.*

Three simplest return stroke models having the same shape of the current function at the striking point are shown in the Fig 3.9. Rakov (1997) gave generalized expression for the current magnitude which can be applied on multiple models:

$$i(z,t) = u(t - z/v_f) \cdot P(z) \cdot i(0, t - z/v), \tag{3.17}$$

where u the Heaviside unit function, v_f the upward velocity of the return stroke which travels to the cloud, v the downward speed of the current wave and $P(z)$ the current attenuation factor which depends on the height.

Table 3.5: Overview of the return stroke models.

Return stroke models	$P(z)$	v
BG model (1941)	1	∞
TL model (1969)	1	v_f
TCS model (1985)	1	$-c$
MTLL model (1987)	$1 - z/H$	v_f
MTLE model (1987)	$e^{-z/\lambda}$	v_f

In the Table 3.5 the expressions for the attenuation factor $P(z)$ and the velocity of the current wave v for different return stroke models are presented.
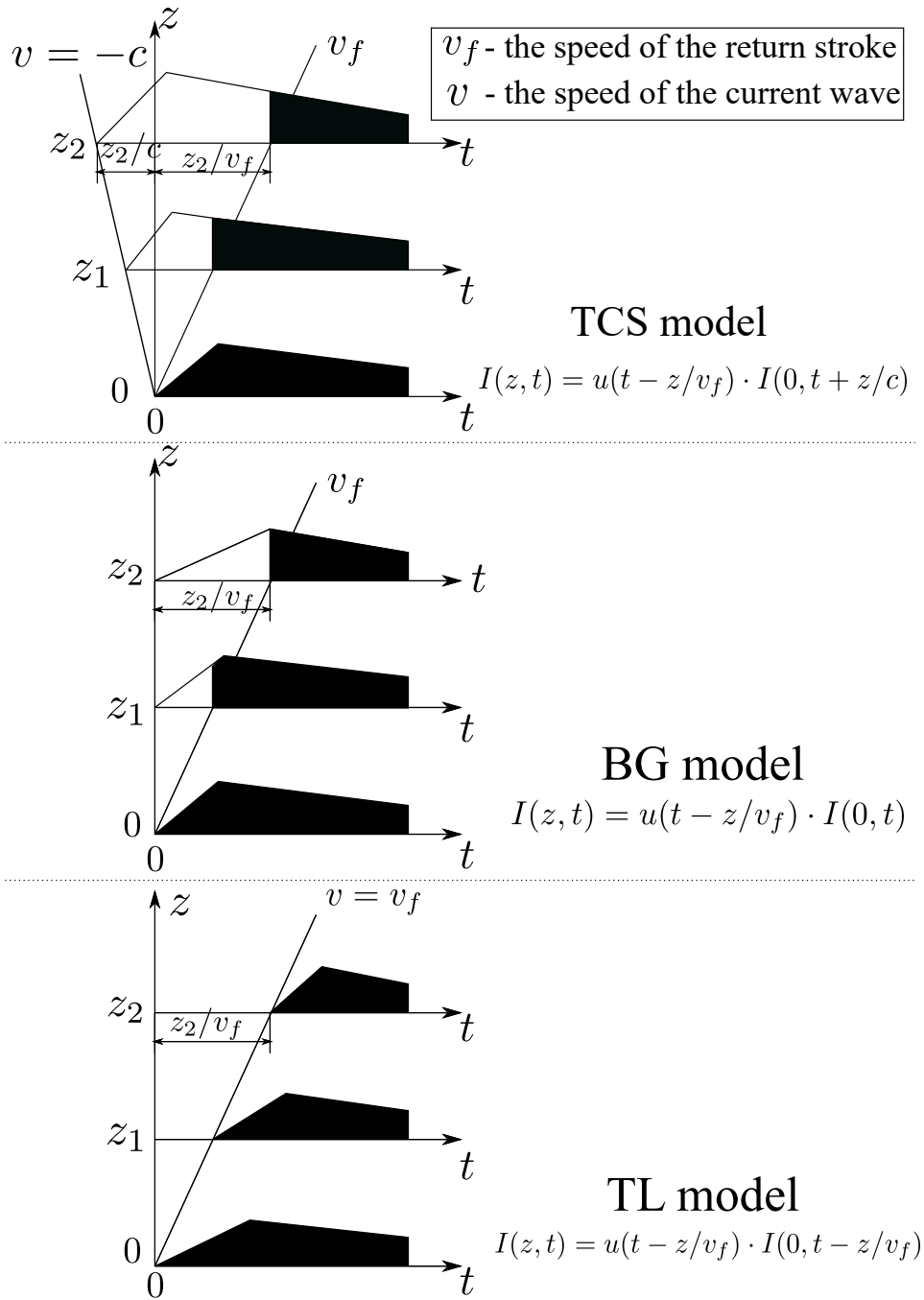
Figure 3.9: Current versus time waveforms at ground ($z = 0$) and at two heights z_1 and z_2 above ground for the TCS, the BG, and the TL return strokes model. Slanted lines labeled v_f and represent the upper speed of return-stroke wave front and the lines labeled v represent the speed of the current wave. The dark portion of the waveform indicates the downward current that actually flows through a given channel section. Note that the channel-base current $I(z_0, t)$ and v_f are the same for all three models. Adapted from Rakov [69].

3.7 Generalized Traveling Current Return Stroke Model - GTCS model

The GTCS model was introduced in order to eliminate the disadvantages of the previous models. Let's assume that the channel is vertical, straight, azimuthally symmetrical and charged with line charge density $\rho_{GTCS}(z)$. A new label for the line charge density for the GTCS model $\rho_{GTCS}(z) = q_0'(z)$ is adopted . The charge in the channel was created by the current of the stepped or dart leader. The charge generation and its previously maintenance can be explained by the existence of an inhomogeneous conductive environment and the transport of the charge along its axis. Thus, the distribution of the longitudinal charge along the channel is not in equilibrium along a vertical conductor above the conductive ground [65]. Possible distribution of charge over the ground was presented in Fig. 3.7.

The process of the lightning discharge proposed by the GTCS model is similar as in the TCS model. In original TCS model it is postulated that the deposited leader charge is removed instantaneously at the moment when the return stroke wave front reaches the height $z = v \cdot t$. It injects source current pulse into the channel core, which travels to the ground with the speed of the light. In the DU model, the removal of the discharge is modeled with exponentially decreasing function defined by the time-discharge constant. Both models have shortcomings in terms of either current or the first derivative discontinuity.

In the GTCS model, the situation is different. When leader charge is deposited on a thin channel core, the deposited charge will create a radial electric field that exceeds the breakdown value pushing the charge away from the core. As a result, the leader channel consists of a thin core surrounded by a radially formed corona sheath as shown in Fig. 3.10.

The corona sheath expands outwards from the channel core due to the repulsive electrostatic forces while the radial electric field is less than the breakdown value field, which assumed to be 2 MV/m by Baum and Baker [66] and 1 MV/m by Kodali et al. [67]. It is generally thought, that the bulk of the leader charge was stored in the corona sheath whose radius is on the order of meters, whereas the highly conducting channel core (with the radius estimated to about 0.5 cm) essentially carries all the axial current [68], [69].

The basis of the GTCS model is the finding of a suitable function that describes realistically the initial line charge density $q_0'(z)$ in the channel according to the experimental observations, as well as the channel-base current i_0.

It is assumed that the line charge density in the corona sheath on the some height
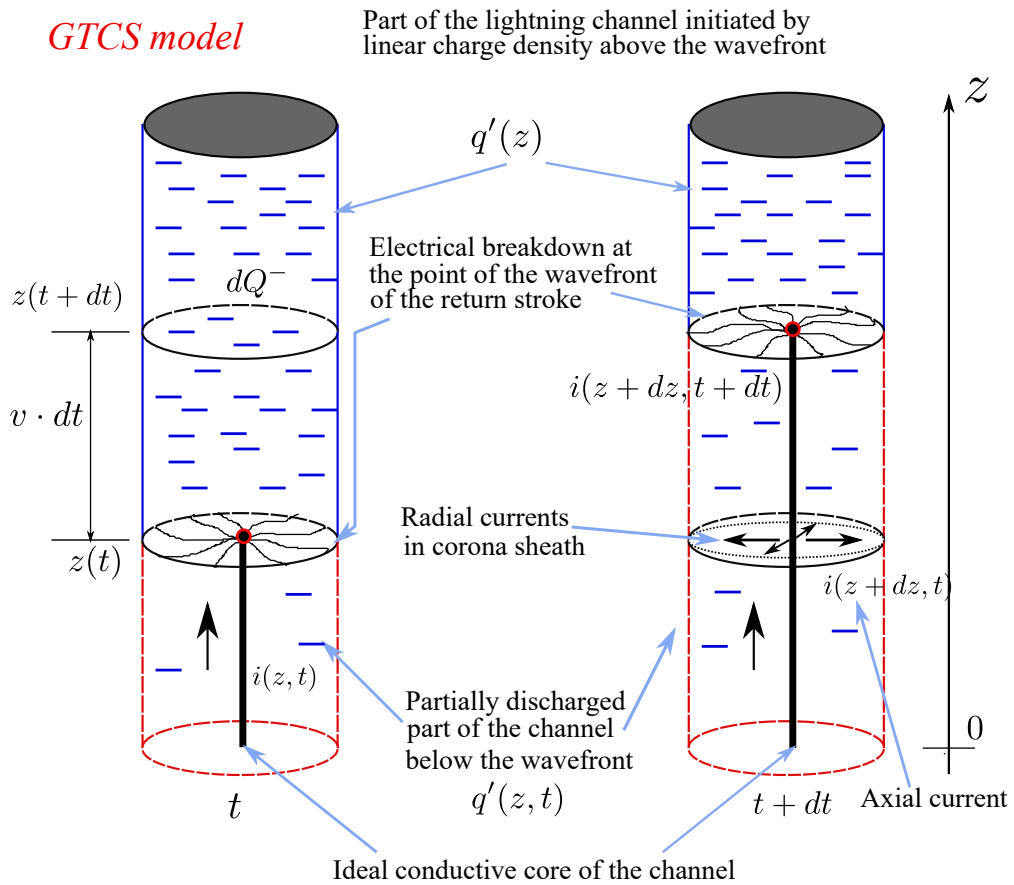
Figure 3.10: Electrical processes in the lightning channel during a return stroke phase according to the GTCS model. Apapted from [65].

z and at some moment of time t is:

$$q'(z,t) = q'_0(z) \cdot f(z,u), u = t - z/v_f, \tag{3.18}$$

where the $q'_0(z)$ is initial charge density in the channel at the time instant $t = 0$. This function is chosen independently of the channel-base current. The function $f(z,u)$ is the scalar channel discharge function. Both functions in Eq. (3.18) are different for the first and subsequent strokes.

It can be seen from the Eq. (3.18) that the channel discharge function $f(z,u)$ in general case depends on the height of the channel z. In the further work it was assumed that $f = f(u)$ in order to simplify the calculation. Since the existence of two currents at the striking point was experimentally confirmed [61], the channel discharge function was separated into two components $f_{bd}(u)$ and $f_{co}(u)$:

$$f(u) = f_{bd}(u) + f_{co}(u). \tag{3.19}$$

Functions $f_{bd}(u)$ and $f_{co}(u)$ can be calculated from the GTCS model, but due to the complexity of the processes it is impossible to determine their dependence on the channel height. The function $f(t - z/v) = f(u)$ is suitable to describe the processes in the channel during the return stroke phase. The channel discharge function is dimensionless physical quantity and for now its native is still unknown from the physical aspect. It is proposed that this function represents the result of all physical process in the lightning channel.

According to the features of the GTCS model, the function f should satisfy the following conditions:

$$f(0) = 0, \tag{3.20}$$

$$f(u) \geq 0 : u \geq 0, \tag{3.21}$$

$$\lim_{n \to \infty} f(u) = 0, \tag{3.22}$$

$$\frac{df(u)}{du} \leq 0 : u \geq v_f, \tag{3.23}$$

for some $z/v_f > 0$.

The GTCS model can be viewed as involving many current sources distributed along the lightning channel that are progressively activated by the upward-moving return stroke wave front. The current wave is generated from the leader charge deposited in the corona sheath. The upward velocity v of the return stroke wave front as well as the downward discharge current-wave speed are assumed to be constant.
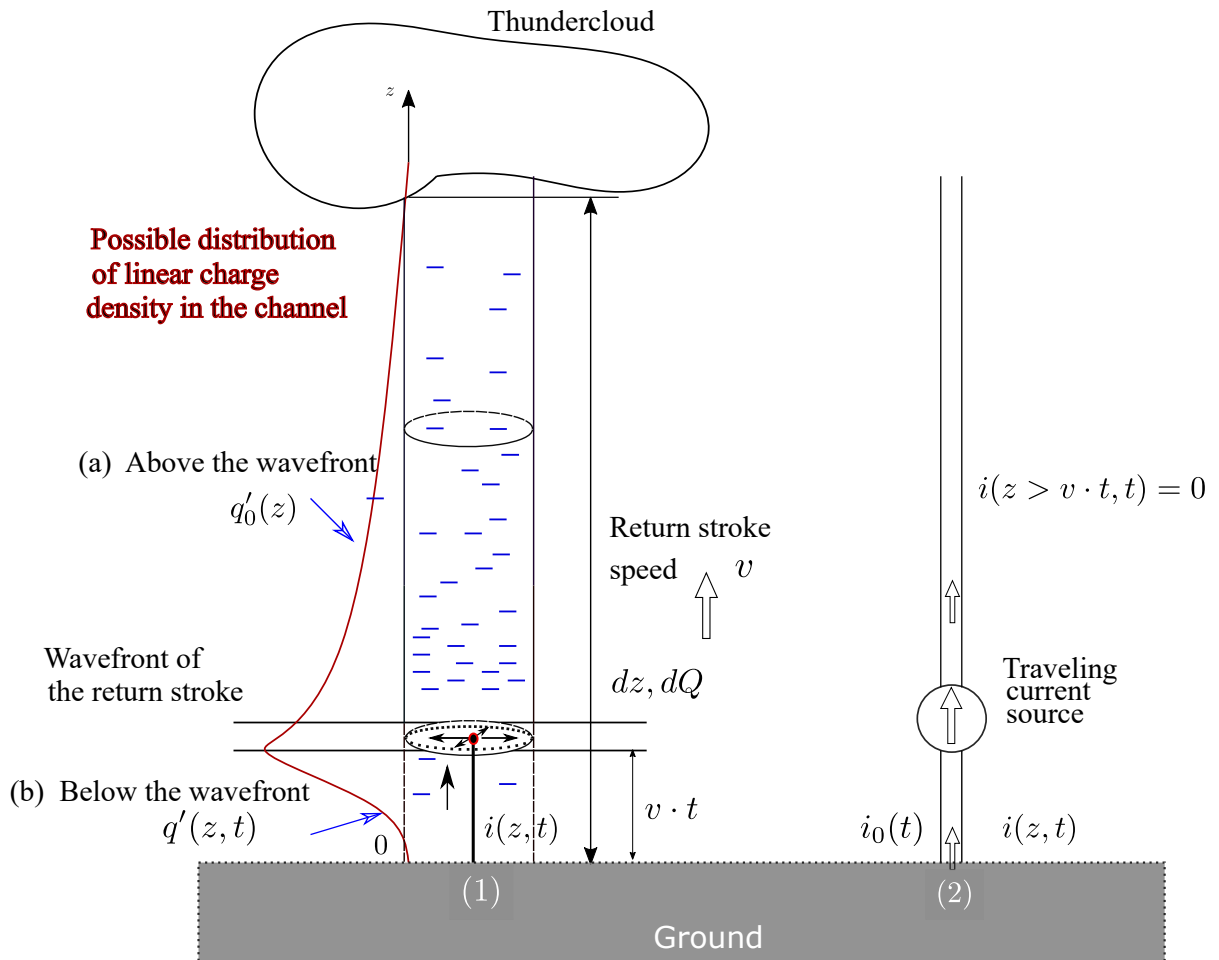
Figure 3.11: (1) Process of the lightning discharge (return stroke) with a possible distribution of the line charge density $q'_0(z)$ along the channel above and below of the wave front according to the GTCS model.
(2) Equivalent circuit.
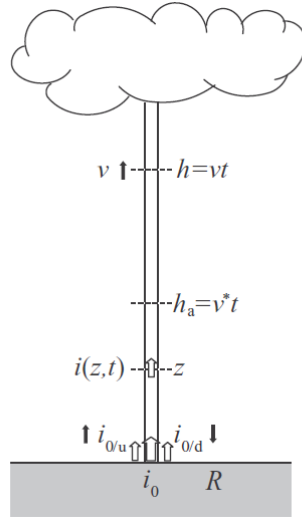
Figure 3.12: Schematic view of the lightning channel with current reflection [65].

In the calculation, the value of $v_f = c/3$ is most often adopted, but practically the upward velocity of the return stroke wave front is an input parameter estimated usually from optical measurements.

The GTCS model enables the examination of the influence of different line charge distribution along the channel [65] and the influence of the current reflections from ground [70] on the processes inside the corona sheath as well as on the radiated lightning electromagnetic pulse. The channel-base current $i_0(t)$ and the initial (negative) leader line charge density $q'_0(z)$ were considered to be known. They are connected through the charge conservation law, and this relation was given by Volterra integral equation of the first kind:

$$i_0(t) = \int_0^{v^*t} q'_0(z) \frac{\partial}{\partial t} f(t - z/v^*) \, \mathrm{d}z, \qquad (3.24)$$

where $v^* = v_f \cdot c/(v_f + c)$ is the so-called *reduced return stroke speed.*

As already state before, the advantage of model compared to the others is that it is possible to take into account the current reflection from the ground (Fig. 3.12).

The downward moving current at the channel-base is the integral of all current pulses coming downward from differential segments over the activated part of the channel:

$$i_{0/d}(t) = \int_0^{h_a} q'_0(z) \frac{\partial}{\partial t} f(t - z/v^*) \, \mathrm{d}z. \qquad (3.25)$$

where is $h_a = v^* \cdot t$. Note that the direction of the current pulse is upwards.

Similarly, the downward moving current $i_d(z, t)$ at the some altitude z was expressed as:

$$i_d(z, t) = \int_0^{h_{az}} q'_0(z) \frac{\partial}{\partial t} f(t - z/v^* + z/c) \, dz, \tag{3.26}$$

where the "activated" channel altitude is defined by $h_a z = v_f \cdot (t + z/c)$.

The total channel-base current i_0 is composed of the downward moving current wave $i_{0/d}$ and the reflected current wave $i_{0/u} = R \cdot i_{0/d}$, that is:

$$i_0(t) = i_{0/d}(t) + i_{0/u}(t) = \frac{(1 + R) \cdot i_{0/d}}{R}. \tag{3.27}$$

Since (the upward) reflected current pulse delays for z/c to the reflected pulse at the ground level, using Eq. (3.25), one obtains:

$$i_u(z, t) = i_{0/u} \left(\frac{t - z}{c} \right) = \frac{R \, i_0(t - z/c)}{1 + R}. \tag{3.28}$$

The channel core current at some altitude is composed of two components, the downward moving component (Eq. (3.26)) and the upward moving component (Eq. (3.28)), that is:

$$i(z, t) = i_d(z, t) + i_u(z, t). \tag{3.29}$$

The values of the ground reflection factor R are known from the lightning current measurements at tall towers [71]. There are two extreme cases. If one neglect the current reflections assuming the grounding impedance is equal to the characteristic impedance of the lightning channel (of the order of a few hundreds of ohms), it follows $R = 0$. If the current waves reflect from the perfectly conducting ground then $R = 1$.

3.7.1 Modeling of the channel-base current and the distribution of the line charge along the channel

The functions $i_0(t)$ and $q'_0(z)$ in the Eq. (3.24) are real physical quantities and represent the channel-base current and the charge distribution along the vertical and straight lightning channel. The Heidler function is used for the channel-base current modeling as it is common in the literature [65]. Its shape is given by:

$$i_{cb}(t) = \frac{I_0}{\eta} \cdot \frac{(t/\tau_1)^n}{1 + (t/\tau_1)^n} \cdot e^{-\frac{t}{\tau_2}}. \tag{3.30}$$

The unknown parameters in Eq. (3.30) are: I_0 - the current peak, n - maxi-

mum of the current steepness, η - correction factor of the current peak, τ_1 and τ_2 - time constants which determines current rise and decay-time. The values of the parameters in the Eq. (3.6) can be obtained from the measurements [72].

During the modeling process, it can be considered that the channel-base current consists of two components: the corona $i_{0c}(t)$ and the breakdown current $i_{0bd}(t)$. The total channel-base current is:

$$i_0(t) = i_{0c}(t) + i_{0bd}(t). \tag{3.31}$$

The parameters for the channel-base current are given in Tab 3.6.

Table 3.6: The parameters of the channel-base current according to [60].

Current	I_0 (kA)	η	τ_1 (µs)	τ_2 (µs)	τ_d (µs)
Breakdown current $i_{0bd}(t)$	13	0.73	0.15	3	0.6
Corona current $i_{0c}(t)$	7	0.64	5	50	5

The function that models the charge in the lightning channel $q'_0(z)$ was introduced in reference [65]. Namely, starting from the Heidler function, it was assumed that the basic function for the line charge density has the form:

$$g(z) = \frac{z^m}{\lambda_1 + z^m} e^{-z/\lambda_2}, \tag{3.32}$$

with the parameters given by $m = n$, $\lambda_1 = v^*\tau_1$ i $\lambda_2 = v^*\tau_2$, while the variable z represents the height of the channel.

Knowing the shape of the basis function (3.32), in a general case the function of the line charge density is the sum of the basis function and the perturbation of its derivatives:

$$q'_0(z) = Q'_0 \left\{ g(z) + \lambda_{d_1} \frac{\mathrm{d}g(z)}{\mathrm{d}z} + \lambda_{d_2} \frac{\mathrm{d}^2 g(z)}{\mathrm{d}z^2} \right\}. \tag{3.33}$$

The parameters λ_{d_1} and λ_{d_2} can be written in the form $\lambda_{d_1} = v^*\tau_{d_1}$ and $\lambda_{d_2} = (v^*\tau_{d_2})^2$, where τ_{d_1} and τ_{d_2} are time discharge constants assumed in the GTCS model. The parameter Q'_0 is the maximum value of the line charge density. The biggest advantage of the function for the modeling the charge in the lightning channel (Eq. (3.33)) compared to other functions is that it could take into account the influence of different charge distribution on physical processes in the lightning channel and on the radiated lightning electromagnetic pulse. The speed of the return stroke v_f that appeared in the previous expressions is constant. It is accepted from optical measurements.

Chapter 4

Modeling of the lightning channel dynamics and its effects

For a detail study of lightning channel dynamics, it is it is necessary to know the basic issues about the structure and physical processes within the channel. In this dissertation, an overview of two models of corona sheat dynamics is given: lightning channel corona sheath model suggested by Maslowski et al. [77] and the lightning channel corona sheath model suggested by Tausanovic et al. [78]. It is important to notice that the first model represents a simplified electrostatic model of corona sheath, while the second model represents, basically, an engineering model that can include different physical effects (not only an electrostatic mechanism) via the channel discharge function. Both models are in agreement with the measurements of the horizontal (radial) electric field measured in the vicinity of triggered lightning channel. Also, in this chapter a short overview of experiments used to verify the calculation of internal electric field and conductivity of the lightning channel is given.

4.1 Experimental techniques

In order to provide better modeling of physical processes in the corona envelope, a brief overview of the experiments and results used to obtain a complete evolution overview of the lightning channel it is given. However, the triggered lightning discharges are taken into account. It was done since at the beginning of the theoretical consideration of the problem, experimental data were available only for this type of lightning discharge. Experimental data, related to the lightning discharge in nature, have been published in the final phase of the research.

The results of both experiments are used, although there are disagreement about the similarity of physical processes in the triggered lightning discharges and in the

discharges in nature. The results of the experiments in nature refer to the integral structure of the lightning channel, while in the triggered discharges, the physical picture is similar to the lightning initiated from tall objects. The difference would arise in the case of the analyzing process at a certain height of the lightning channel.

4.1.1 Triggered lightning discharges

In addition to lightning modeling and understanding the processes in the lightning channel, it is also important to experimentally verify obtained data. One of the world's best centers for lightning experiments is located in north-central Florida, at the International Center for Lightning Research and Testing (ICLRT).

The process of artificial initiation of lightning by rocket-and-wire triggering is shown in Fig. 4.1 in a sequence of 6 figures [79]. When the rocket raises wire to a height of several hundred meters in a time of 2 or 3 s, electrical breakdown occurs at the top of the wire. When the grounded wire has a length of several hundred meters, electric field at the top of the rocket exceeds some critical value and the upward propagating, positively-charged leader (UPL) start moving from the rocket to the cloud. The triggered wire is a Kevlar-covered copper wire with diameter of 0.2 mm. This wire is at one end connected to the ground, and the other end is bound to the bottom of the rocket. Wire generally explodes or melts 10 ms after of the start propagation of the upward positive leader.
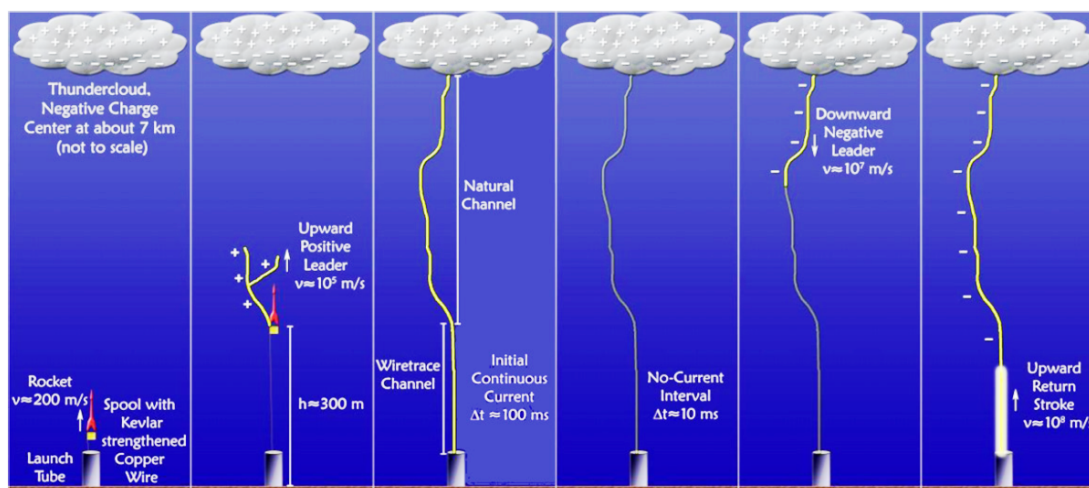
Figure 4.1: Rocket triggered lightning. Adapted from [79].

In one of such experiments, Miki et al. [80] measured horizontal electric field waveforms with Pockels sensors for electric-field measurements at radial distances from 0.1 to 1.6 m from the triggered lightning channel at the International Center for

Lightning Research and Testing at Camp Blanding, Florida. The dynamics range of the measuring system was in the range from the 20 kV/m to 5 MV/m and with the bandwidth from 50 Hz to 1 MHz. Also, the corresponding channel base currents and the vertical electric field at 5, 15, and 30 m from the lightning channel were also measured using a current viewing resistor and flat-plate antennas, respectively.

In this chapter, the most important experimental results which will be used for further modeling are presented. Using experimental measurements at Camp Blanding, Florida [80] and theoretical assumptions in the study [78], the measuring channel-base current and corresponding fitted curve are shown in Fig. 4.2.
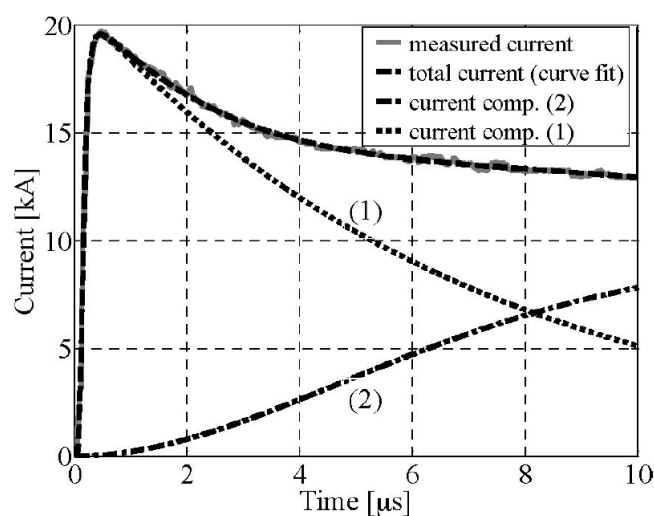
Figure 4.2: Measurement and fitted channel base current according to the [80].

The trailing edge of the radial electric field during the return stroke phase is shown in Fig 4.3. The radial distance for stroke 1 in flashes S0033 was 0.1 m measured by Miki et al. [80]. Time onset is set to be at the instant of time when the electric field has its maximum. The corresponding channel-base current is shown in Fig. 4.2.
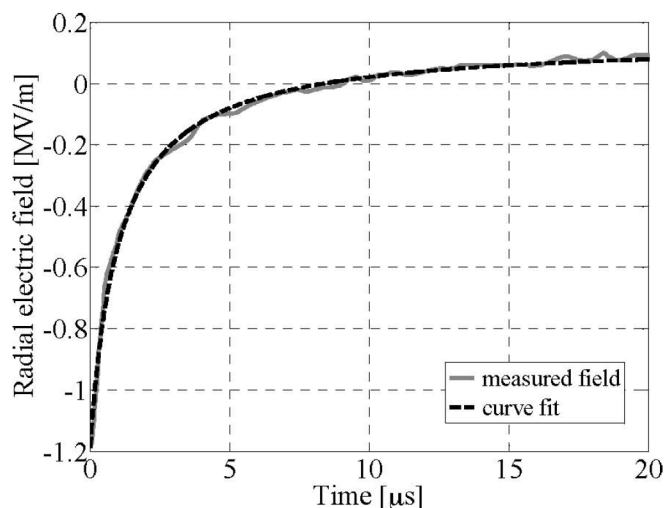
Figure 4.3: Measurement and fitted radial electric field according to the [80].

4.1.2 Lightning discharge in nature

One of the rare measurements of natural lightning are presented in the experiment performed in Qinghai Plateau of China [81]. The distance from the observation site to the cloud-to-ground (CG) lightning was about 7.14 km. The CG lightning consisted of six return strokes and the spectrum of every return stroke is captured. CG lightning with six return strokes has been recorded by slitless spectrograph and the system of fast antenna and slow antenna.

Slitless spectrograph consists of high-speed camera (this camera was operated at 9110 fps with the exposure time of 109 μs) and a plane transmission grating of 600 lines mm^{-1} putting in front of the object lens. The recorded spectrum has a wavelength range from 400 to 1000 nm. Wave resolution is about 1.1 nm. The equipment that is used in this experiment was high-speed and high-sensitivity imaging equipment. The synchronous radiated electric field of lightning was measured with fast antenna and slow antenna systems.

The spectrum of six return strokes is shown in Fig. 4.4. R0 represents the first return stroke and R1 to R5 represent the corresponding subsequent return strokes. The radiated electric field recorded by slow and fast antenna is recorded and depicted in Fig. 4.5.

There were two assumptions in their analysis:

1. Lightning channel during return stroke phase is very thin;

2. The channel is in the local thermodynamic equilibrium (LTE).
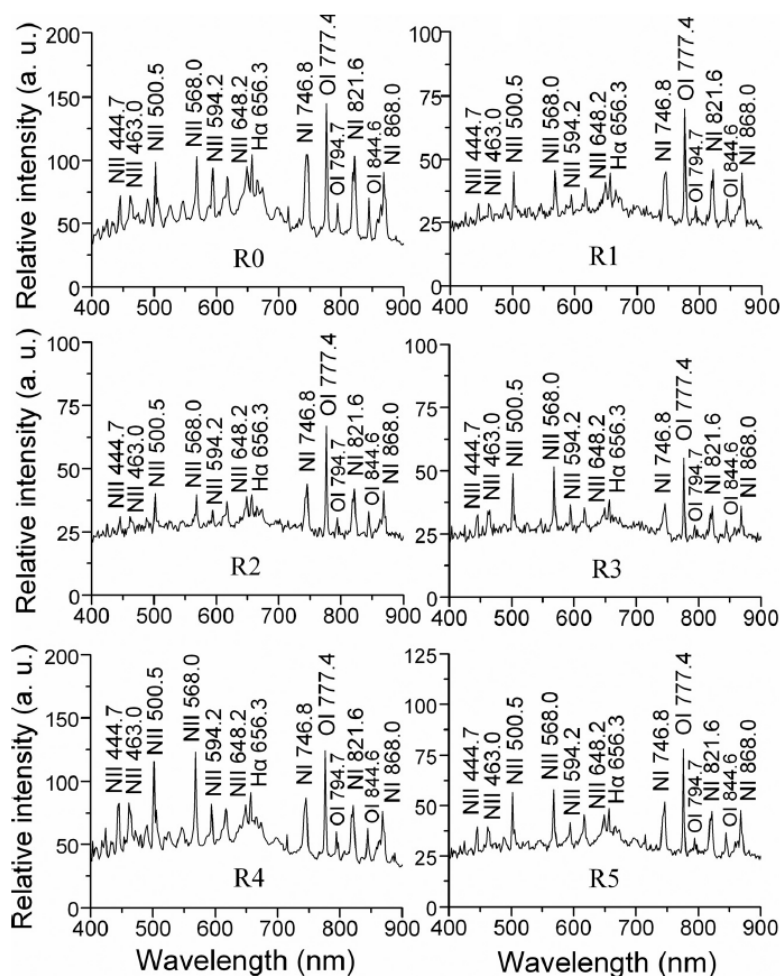
Figure 4.4: Spectrum of six return strokes [81].

It can be seen from the assumptions that the experiment refers to the analysis of the lightning channel as an integral structure, but this experiment enables to verification of all important physical quantities related to the lightning channel.

Combination of recorded lightning spectra and the radiated electric field will give more information about the characteristic of the lightning channel. Moreover, the temperature of the channel, the electron density, the electrical conductivity and the resistance of lightning plasma channel are obtained. On the other hand, the current is estimated on the base of simultaneosy measured radiated electric field. The internal electric field is calculated by Ohm's law.

Fundamental formulas for calculation the important parameters during the evolution of lightning channels based on experimental data are presented in this chapter, according to the [81]. Temperature can be obtained by the slope parameter of a
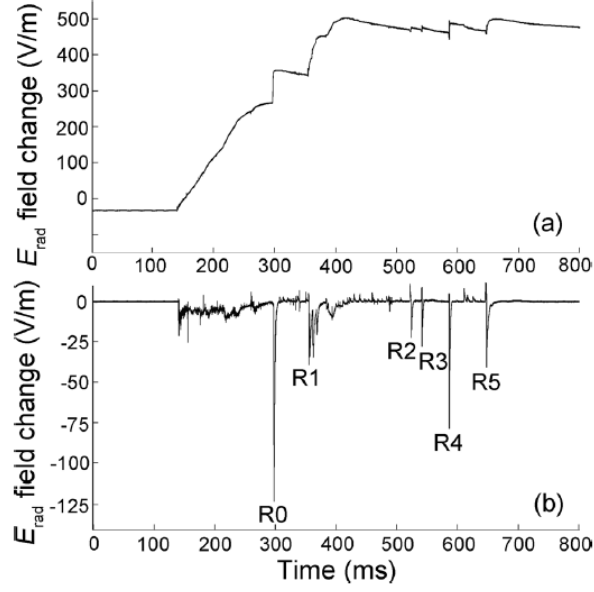
Figure 4.5: Waveforms of radiated electric field recorded by: (a) *slow* antenna, (b) *fast* antenna. Adapted from [81].

linear fitting of the following equation:

$$\ln\left(\frac{I\lambda}{gA}\right) = -\frac{E}{kT} + C,$$ (4.1)

where I is the relative intensity of lines, λ is the wavelength, g and A are the statistical weight and transition probability, k is the Boltzmann's constant, E is the upper excitation energy of corresponding transition, T is the temperature, and C is the constant.

The electron density can be obtained using ionic and atomic lines from the same element:

$$n_e = 2 \times \frac{(2\pi mkT)^{3/2}}{h^3} \cdot \left(\frac{I_a}{I_i}\right) \times \left(\frac{gA}{\lambda}\right)_i \times \left(\frac{\lambda}{gA}\right)_a,$$
$$\times \exp\left(-(V + E_i - E_a)/(kT)\right),$$ (4.2)

where n_e is the electron density, V is the ionization energy, I_a and I_i are the relative intensity of atomic and ionic lines, respectively and E_a and E_i are the upper level of those lines.

Discharge current $i(t)$ and radiation field E_{rad} is related through following expression as in the TL model:

$$i = \frac{2\pi\varepsilon_0 c^2 \cdot D}{v} \cdot E_{rad} , \qquad (4.3)$$

where c is the speed of the light, v is the speed of the return stroke (in this case return stroke speed is $v = 1 \times 10^8$ m/s) and D is the distance between the lightning channel and observation side.

In the study [81], electrical conductivity of the channel, σ, the resistance of the plasma channel per the length R and the internal electric field in the channel E_{int} are expressed as:

$$\sigma = \frac{1}{m_e \cdot \nu_{ei} \cdot \alpha}, \qquad (4.4)$$

$$R = \frac{1}{\sigma \cdot \pi \cdot r^2}, \qquad (4.5)$$

$$E_{int} = i \cdot R, \qquad (4.6)$$

where $\alpha = 0.51$ is the correction factor for the conductivity of the fully ionized plasma and ν_{ei} is the electron-ion collision frequency given by Maxwell distribution.

4.2 Model of lightning channel corona sheath suggested by Maslowski et al.

The models of corona envelope during the return stroke process used in this dissertation is based on theoretical and experimental studies of corona discharges in coaxial geometry performed in laboratory.

In the study [77], Maslowski and Rakov considered lightning channel corona sheath dynamics in triggered lightning. The basic assumption is that the lightning channel consists of very conductive channel core, whose diameter is about 1 cm and carries all the longitudinal current. Lightning corona sheath stretches around the central core and its diameter is the order of several meters. Leader charge deposited on a thin and long lightning channel will create a electric field in a predominantly radial direction [77]. The corona envelope extends outward until the value of the radial electric field reaches the value of breakdown electric field. The value of the breakdown field is assumed to be 2MV/m by Baum and Baker [66] and 1 MV/m by Kodali et al. [67].

Detailed information about the role of corona envelopes in various lightning processes is given by Heckman and Williams [82]. According to them, the region of the corona envelope with an electric field higher than 1 MV/m becomes conductive in

nanoseconds at 500 mbar pressure. This is the region where the uniform breakdown occurs. A detailed description of so-called *reverse, or back corona* associated with the return stroke process is given by Gorin [83]. Practically, the most important input parameters for the detailed analysis of the corona sheath dynamics are the line charge density $\rho^-(z,t)$ and the current versus height $i(z,t)$.

The important equations for corona sheath dynamics are derived using the simplified model representation of the lightning channel [77], as shown in Fig. 4.6. From the gas discharge physics follows that the leader charge is stored in corona sheath. At the moment in which return stroke becomes active, this charge collapses into the channel core and transfers to the ground. Based on that fact, the return stroke in negative lightning can be represented as positive current wave that propagate upward along the previous formed leader channel and injects positive charge into the corona sheath. At the end of the return stroke process, the negative charge in the corona sheath is neutralized. It is assumed that longitudinal current flowing in the channel core and decreases with increasing height. Also, it is assumed that conduction current is much greater than the displacement current. In the first stage of the return stroke process, previous mentioned condition is not satisfied (in the first microseconds where the radial electric field change rapidly), but after that stage, mentioned condition is satisfied during the first of the process.

In the Fig. 4.6 core radius is noted as r_{core} and corona sheath radius is noted as r_{outer}. For a channel segment of length dz at height z, the charge conservation principle can be expressed as:

$$dQ_{leak} = dQ_{in} - dQ_{out}, \tag{4.7}$$

where dQ_{in} is the input positive charge at the bottom of the segment, dQ_{out} is the output positive charge at the top of the segment and dQ_{leak} is the leakage positive charge. The positive leak charge can be expressed as a function of corresponding longitudinal current components in the channel core:

$$dQ_{leak} = i(z,t)dt - i(z+dz, t+dz/v)dt, \tag{4.8}$$

where v is the return stroke speed, so the propagation time of the current wave from the bottom to the top of the segment is $dt = dz/v$.

For transmission-line-type of models, the longitudinal current distribution along the channel is given by:
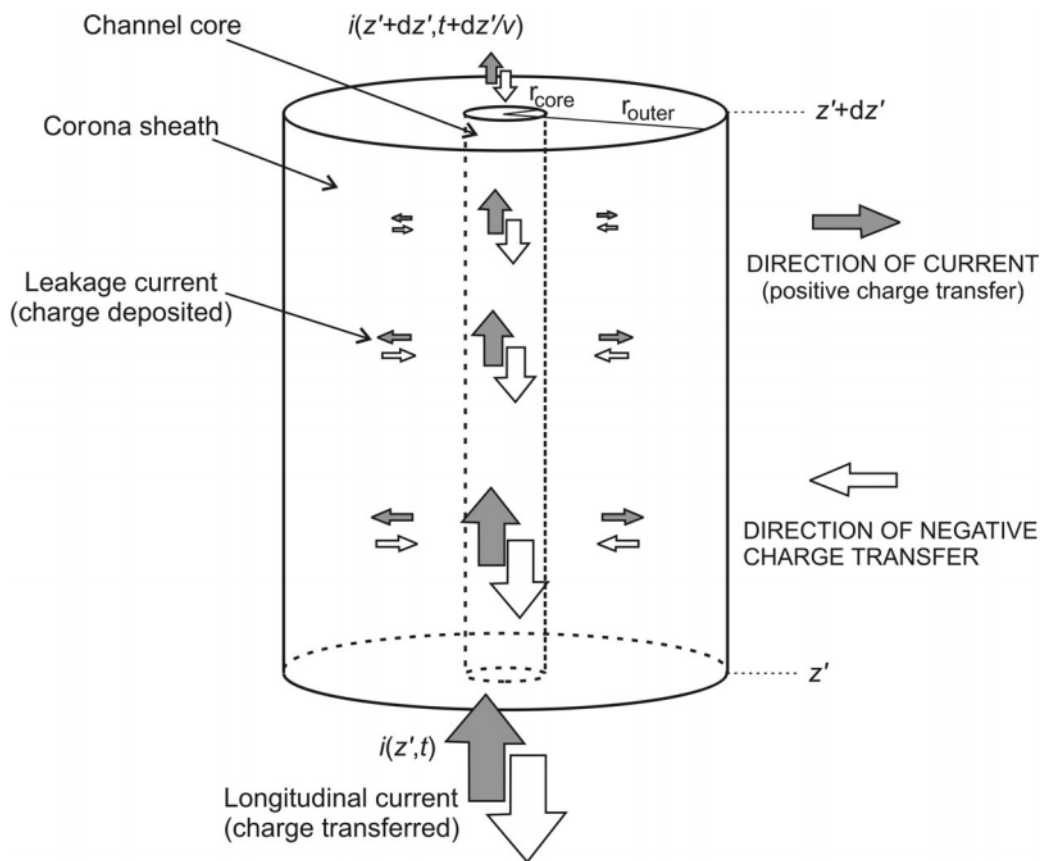
Figure 4.6: The model of lightning channel suggested by Maslowski et al. [77].

$$i(z,t) = \begin{cases} P(z) \cdot i(0, t - z/v), & t \geq z/v. \\ \\ 0, & t < z/v. \end{cases} \tag{4.9}$$

where $i(0, t - z/v)$ is the channel-base current, and $P(z,t)$ is the current attenuation factor (the value of the current attenuation factor for different models is given in the Tab. 3.1). After this explanation, the expression for leak positive charge is:

$$dQ_{leak} = \Big[P(z) - P(z + dz) \Big] i(0, t - z/v)dt. \tag{4.10}$$

Expression for conduction current is obtained from Eq. (4.10), which flows radially from the lightning channel core:

$$i_{leak}(z,t) = \frac{dQ_{leak}}{dt} = P(z) \cdot i(0, t - z/v) - P(z + dz) \cdot i(0, t - z/v). \tag{4.11}$$

Using approximation $P(z + dz) \cong P(z) + \dfrac{dP(z)}{dz} \cdot dz$, the Eq. (4.11) can be expressed in the form:

$$i_{leak}(z,t) = -\frac{P(z)}{dz} i(0, t - z/v). \tag{4.12}$$

Starting from Eq. (4.12), equation for the line charge density ρ_{leak} deposited on channel by the return stroke is expressed by:

$$\rho_{leak}(z,t) = -\frac{P(z)}{dz} \int_{z/v}^{t} i(0, \tau - z/v) \cdot d\tau. \tag{4.13}$$

This model implies the constant space charge density inside both zones of corona sheath with the constant outer radius of zone 2. In the TLM the line charge density in the channel sheath is given by Eq. (4.13). Negative line charge density just prior to the return stroke $q_{leak\infty}^{-}$ is obtained by changing the sign in Eq. (4.13) and assuming $t \to \infty$ in the upper limit of the integral:

$$q_{leak\infty}^{-} = \frac{dP(z)}{dz} \int_{z/v}^{\infty} i(0, \tau - z/v)d\tau. \tag{4.14}$$

Note that $dP(z)/dz < 0$. The space charge density of the deposited charge in zones 1 and 2 (negative charge is distributed evenly in zones) can be expressed as:

$$\rho_{TLM}^{-} = \frac{q_{leak\infty}^{-}}{(r_{outer}^{-})^2 \pi}, \tag{4.15}$$

where r_{outer}^- is constant.

The space charge density of the positive amount of deposited charge in zone 1 can be expressed as:

$$\rho_{TLM}^+ = \frac{Q^+/dz}{(r_{outer}^+)^2 \pi}, \tag{4.16}$$

where the values for r_{outer}^+ and Q^+ are taken from the study [77].

Maslowski and Rakov deduced the existence of two zones around the lightning channel core during the return stroke stage based on the electric field measurements [80], and the consideration of the lightning channel corona sheath dynamics [77], which is displayed in Fig. 4.7. The zone 1 has net positive charge (positive charge is deposited by radial conduction current flowing during the return stroke stage). Zone 2 contains negative charge. In the references, this model of corona sheath dynamics is known as model with exponential charge decay in zone 2 ($r_{outer}^- = const$). Namely, during the return stroke phase negative charges drift from zone 2 to zone 1, so the charge in zone 2 exponentially decreases, while $r_{outer}^- = const$. In the study [77], authors consider that the final neutralization of the corona charge occurs after the return stroke stage.

An improved model of corona sheath was suggested by Maslowski et al. [84]. Maslowski et al. proposed two different models: (1) the model with exponential decay of the charge ($R_{outer}^- = r_{outer}^- = const$, the same model is applied in the study of Maslowski et al. [77]) and (2) the model with decrease of zone 2 ($R_{outer}^- \neq const$, the same model is applied in the study of Tausanovic et al. [78]). Maslowski [84] demonstrated that these two models give similar results when the charge decay constant is on the order of a few hundreds of microseconds in both models. That study includes the calculation of the corona sheath radius and the velocity of expansion and shrinkage of the corona sheath. The velocity of the corona sheath expansion is 10^6 m/s at the beginning and of the order of 10^4 m/s at the end of the return stroke stage. The average velocity of the corona sheath expansion is 10^5 m/s. This velocity is approximately equal to the speed of the streamer propagation in laboratory experiments [85].
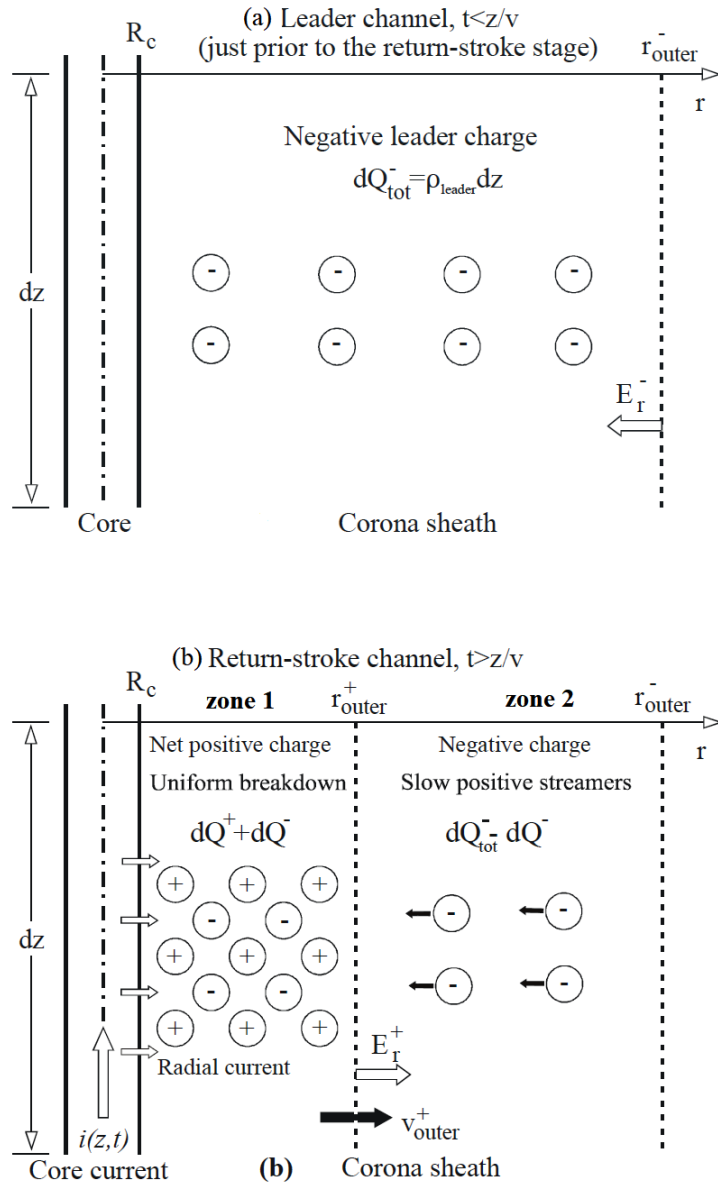
Figure 4.7: (a) Leader channel just prior the return stroke stage. (b) Lightning channel dynamics during the return-stroke phase according to the [84].

4.3 Model of lightning channel corona sheath suggested by Tausanovic et al.

Using cylindrical model of lightning channel, Tausanovic et al. [78] postulated the existence of three zones that surrounds the lightning channel core. Zone 1 is surrounding channel core, zone 2 is surrounding zone 1 containing negative charge, while zone 3 is surrounding zone 2. This is zone without charge, Fig. 4.8. As a

result of the attractive forces on the negative charges in zones 1 and 2, charges move to the core and increase the charge density in zone 1. In this model, it is supposed that the space charge density is constant inside both zones of the corona sheath, but zone 2 shrinks as negative charges move toward the core, so that $R_{outer}^- \neq const$. It is also assumed that the electric fields at the boundary of zone 1, E_r^+ has constant value during the return stroke stage, as well as the electric field at the boundary of zone 2, E_r^-.
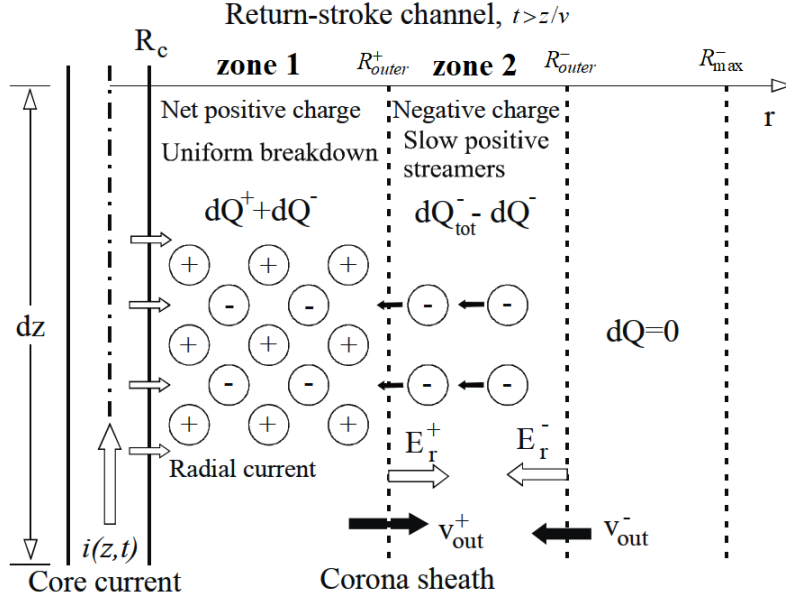
Figure 4.8: Corona sheath dynamics suggested by Tausanovic et al. [78].

For the detail study of the corona sheath dynamics, calculating characteristic quantities as in Maslowski model, it was necessary to calculate channel discharge function versus time $f(u)$ by semi-empirical method (or the channel charging function $f^+(u) = 1 - f(u)$). Tausanovic et al. calculated $f(u)$, using the theoretical expression for the radial electric field in the immediate vicinity of the channel core derived from the Gauss' law applied to the GTCS model and the measured electric field waveforms of Miki et al. [80] (Fig. 4.9).

Both radii of corona sheath zones and their velocities versus time in the bottom part of the channel have been calculated based on measured channel-base current $i_0(t)$ and the calculated channel discharge function $f(u)$. Maximum radius of zones 1 and 2 at 2 m above ground are less than 1.5 and 6 cm, respectively [78]. Corresponding radial corona sheath velocities are less than 6×10^4 m/s.

The space charge density of the negative charge deposited in zones 1 and 2 are:
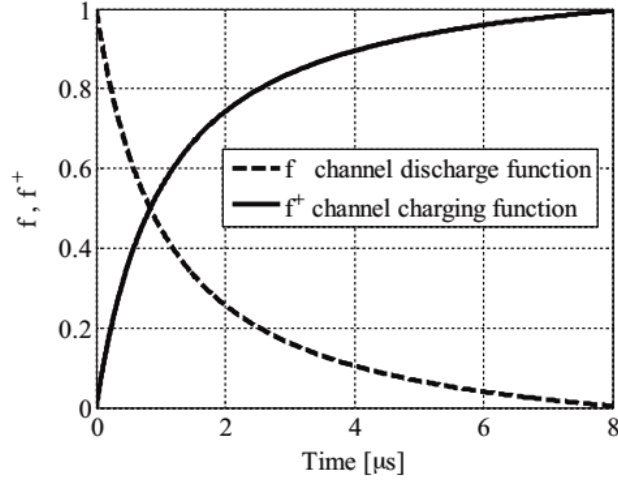
Figure 4.9: Channel discharge function versus time in the GTCS model. Adapted from [78].

$$\rho_{GTCS}^{-} = \frac{-q_0^{+}}{(R_{out}^{-})^2 \cdot \pi}, \tag{4.17}$$

where $-q_0^{+}$ is the initial charge density in the channel and R_{out}^{-} is the radius of zone 2 during the discharge. The space charge density of the deposited charges in zone 1 is:

$$\rho_{GTCS}^{+} = \frac{q_0^{+} \cdot f^{+}}{(R_{out}^{+})^2 \cdot \pi}. \tag{4.18}$$

where R_{out}^{+} is the radius of zone 2, $q_0^{+} f^{+}$ is the positive charge deposited charge in zone 1 and f^{+} is the channel charging function calculated in [78].

Distribution of the lightning charge along the channel prior to return stroke play a crucial role in the generation of the channel-base current. Experimental physicists usually measure the electric and magnetic fields from the lightning channel. These field waveforms are used for examination the dynamics of the corona envelope during the discharge.

Chapter 5

Evolution of the lightning channel

The lightning channel consists of high conductive channel core that carries total axial current with a diameter about 1 cm and the corona sheath with a storage charge from the cloud with a diameter of about several meters. Despite the importance, physical mechanism and formation of the corona sheath are relatively poorly understood. The corona can be modeled in various ways using the engineering models that describe the dynamics of the process. The corona sheath plays an important role in the lightning channel dynamics. The longitudinal electric field along the axis and the channel core conductivity of a straight, vertical lightning channel above ground has been calculated. Also, the contribution of current reflections from the ground on the corona sheath dynamics during the return stroke has been considered. Due to the comparison, the same channel-base current for all models has been assumed.

5.1 Vertical electric field inside the lightning channel

The lightning channel is modeled by a negatively charged corona sheath that stretches around a thin, very conductive central core. It is commonly held that the majority of the leader charge is located within the corona sheath radius, which is in the order of meters, while the highly conductive channel core, with a diameter assessed at around 1 cm, in effect transports total axial current. The channel charge generates a strong radial as well as vertical electric field inside the corona sheath.

Vertical electric field inside the channel sheath is calculated assuming the straight, vertical channel above perfectly conducting ground. This implies the existence of image charges which greatly contribute to the field, especially near the ground. It is assumed that the charge distribution has a dominant influence on the field ma-
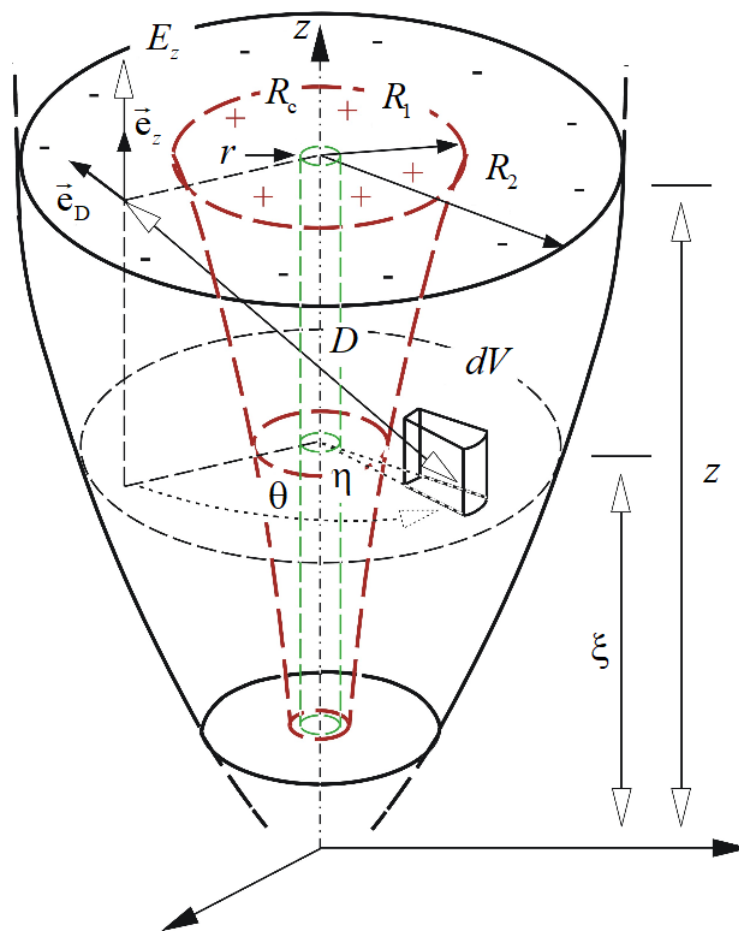
Figure 5.1: Schematic representation of the part of the lightning channel during return stroke. Adapted from [73].

gnitude in the corona sheath. Note that all other effects such as diffusion of charges, kinetic pressure in the channel sheath and magnetic field due to the longitudinal (core) and radial current and thus causing additional (rotational) electric field have been neglected. Additionally, it is neglected all other effects caused by the existing magnetic field in the channel sheath, for example Lorentz force, charge drifts, magnetic pressure, etc.

The geometry of the problem is shown in Fig. 5.1. The channel core with a negligible diameter is assumed to be straight and vertical above perfectly conducting ground. Infinitesimally small channel-core diameter simplifies the geometry of channel structure facilitating the computation. However, it will be shown in this chapter that the vertical electric field in the channel sheath will not be significantly changed across its diameter, especially not if the distance is a few centimeters from the channel axis [73]. The vertical electric field due to the charges (positive and negative) in zone 1 is given by:

$$E_{z1}(z,r) = \frac{1}{4\pi\varepsilon_0} \int_{\xi=0}^{H} \int_{\theta=0}^{2\pi} \int_{\eta=0}^{R_1} \frac{(dq^- + dq^+)}{D^2} \vec{e}_z \cdot \vec{e}_D, \tag{5.1}$$

where $\vec{e}_z$ and $\vec{e}_z$ are the unit vectors of z-axis and distance, respectively. Other terms in Eq. (5.1) are:

$$D^2 = r^2 + \eta^2 - 2r\eta\cos\theta + (z-\xi)^2, \xi \geq 0 \tag{5.2}$$

where $dq^- = \rho^- dV$, $dq^+ = \rho^+ dV$ and $dV = \eta d\eta d\theta d\xi$. For the TL models, ρ^- and ρ^+ are given in Eq. (4.15) and (4.16), respectively, whereas the upper limit of integral $R_1 = r_{out}^+$ is adopted from the study [77]. For the GTCS model, ρ^- and ρ^+ are defined by Eq. (4.17) and (4.18), respectively, whereas $R_1 = r_{out}^+$ is adopted from the study [78]. Variables in Eq. (5.1) and (5.2) should be a function of ξ, that is $R_{out}^-(\xi)$ and $R_{out}^+(\xi)$. In the previous expressions, the channel charging function $f^+(t - \xi/v)$ is used.

Vertical electric field due to the negative charge in zone 2 is given by:

$$E_{z2}(z,r) = \frac{1}{4\pi\varepsilon_0} \int_{\xi=0}^{H} \int_{\theta=0}^{2\pi} \int_{\eta=R_1}^{R_2} \frac{dq^-}{D^2} \vec{e}_z \cdot \vec{e}_D, \tag{5.3}$$

For the TL models, the upper limit of integral in Eq. (5.3) is $R_2 = r_{outer}^-$ [77] and for the GTCS model $R_2 = R_{out}^-$ [78].

According to the theorems of the images, the contribution to the strength of the electric field that arises from the charge of images must be taken into account given the fact that the channel with a large amount of charge is located above the highly conductive ground. The channel image has the same shape as the original one and is placed just below the ground. It is electrically charged with the same amount of electricity as the original, only the opposite sign. The vertical electric field due to the presence of channel image of zone 1 is expressed as:

$$E_{z1L}(z,r) = \frac{1}{4\pi\varepsilon_0} \int_{\xi=-H}^{0} \int_{\theta=0}^{2\pi} \int_{\eta=0}^{R_1} \frac{(dq_I^+ + dq_I^-)}{D_I^2} \vec{e}_z \cdot \vec{e}_{DI}. \tag{5.4}$$

The terms in Eq. (5.4) are: $dq_I^+ = -\rho^- dV$ and $dq_I^- = -\rho^+ dV$, ρ^- and ρ^+ as well as R_1 have the same values as explained in the calculation of the Eq. (5.4). Distance from the elementary volume element of the image from the point of the calculated is:

$$D_I^2 = r^2 + \eta^2 - 2r\eta\cos\theta + (z-\xi)^2, \xi \leq 0. \tag{5.5}$$

The vertical electric field due to the positive image charge in zone 2 is given by:

$$E_{z2L}(z,r) = \frac{1}{4\pi\varepsilon_0} \int_{\xi=-H}^{0} \int_{\theta=0}^{2\pi} \int_{\eta=R_1}^{R_2} \frac{dq_I^+}{D_I^2} \vec{e}_z \cdot \vec{e}_{DI}. \tag{5.6}$$

According to the law of electrostatics, the total electric field inside the corona sheath is obtained by the sum of all components of the electric field:

$$E = E_{z1} + E_{z1L} + E_{z2} + E_{z2L}. \tag{5.7}$$

5.1.1 Results of the calculation of the vertical electric field

Using Eq. (5.7) the vertical field components generated by charges in zones 1 and 2 and the total vertical field for three transmission-line-type models are calculated. That is made for the MTLL, the MTLP and the MTLE model as well as for the GTCS model. All calculations are performed at $t = 0.2$ µs of the discharge when the return stroke wave front has reached 33.6 m above the ground since the return stroke velocity is set to $v = 0.56c$ ($v = 1.68 \times 10^8$ m/s). It is slightly higher than the value accepted in [77] ($v = 1.3 \times 10^8$ m/s), but this causes no significant changes in quantitative and qualitative analyses given in this study. In all cases, the magnitude of the critical radial electric field on the boundary of zones 1 and 2 that is $E_r^+ = 1$ MV/m and $\left|E_r^-\right| = 1$ MV/m , respectively, are assumed. All other values of the parameters regarding TLM are overtaken from [77].

Total vertical electric fields along the channel axis for the MTLL, the MTLP and the MTLE model, respectively, are shown in Fig. 5.2. The contributions of both zones including their images are also depicted. It is obvious that the field of the negative charges in zone 2 is always positive, while the one of net positive charges in zone 1 is negative up to 5 m and then changes the sign. The strongest electric field (about 1.8 MV/m) is found for the MTLE model, whereas the field intensities for the MTLP and the MTLL are about 1.5 MV/m and 1 MV/m, respectively.

Total vertical electric fields along the channel axis at $t = 0.5$ µs for the MTLL, the MTLP and the MTLE model are shown In Fig. 5.3. At this moment, the return stroke wave front was at 84 m above the ground. In that case, at the very bottom of the channel, negative electric field is calculated for the MTLL model and to some small extent for the MTLP model. This negative field is constantly present during the discharge. This behavior can be explained by a strong influence of the net positive charges in zone 1 which overrides the influence of the negative charge in zone 2.

Total vertical electric field and its components along the channel axis for the GTCS model for coefficient of reflection $R = 0$ and $R = 1$ are shown in Fig. 5.5. In
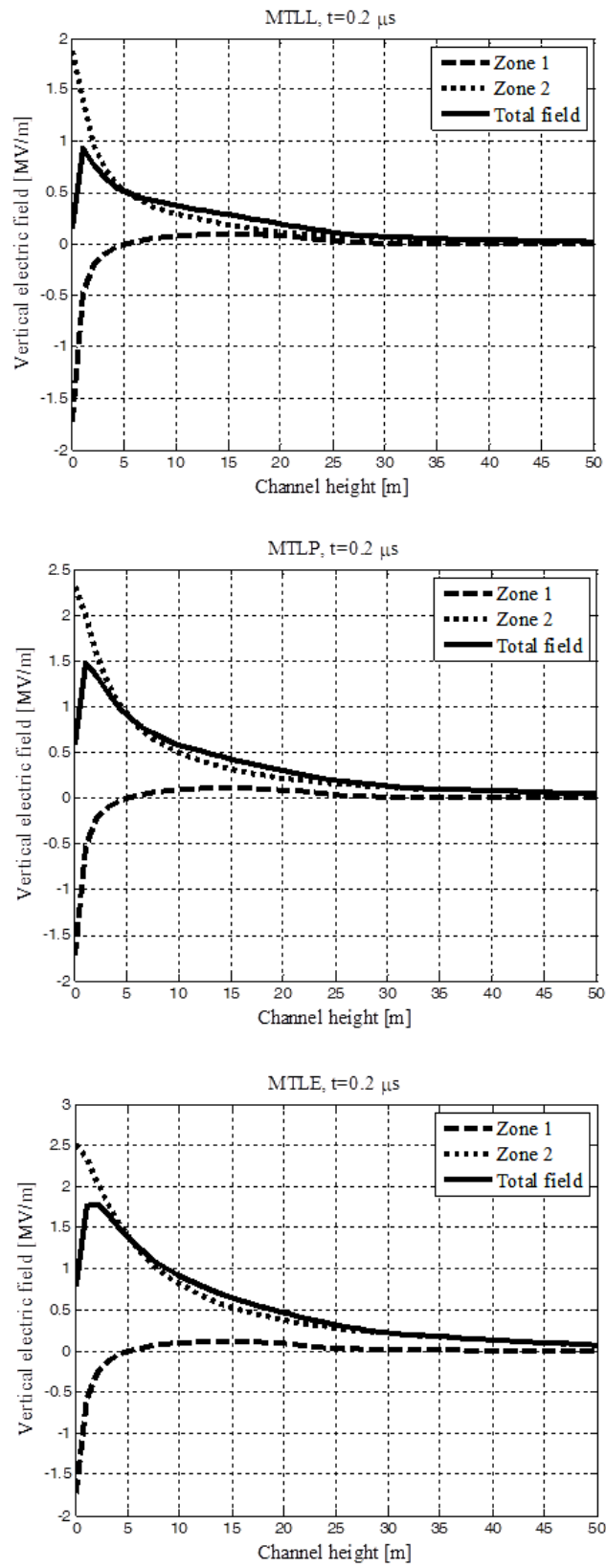
Figure 5.2: Vertical electric field along the channel axis at $t = 0.2$ µs of the discharge for MTLL, MTLE and MTLP models. All other values of parameters are overtaken from [77].
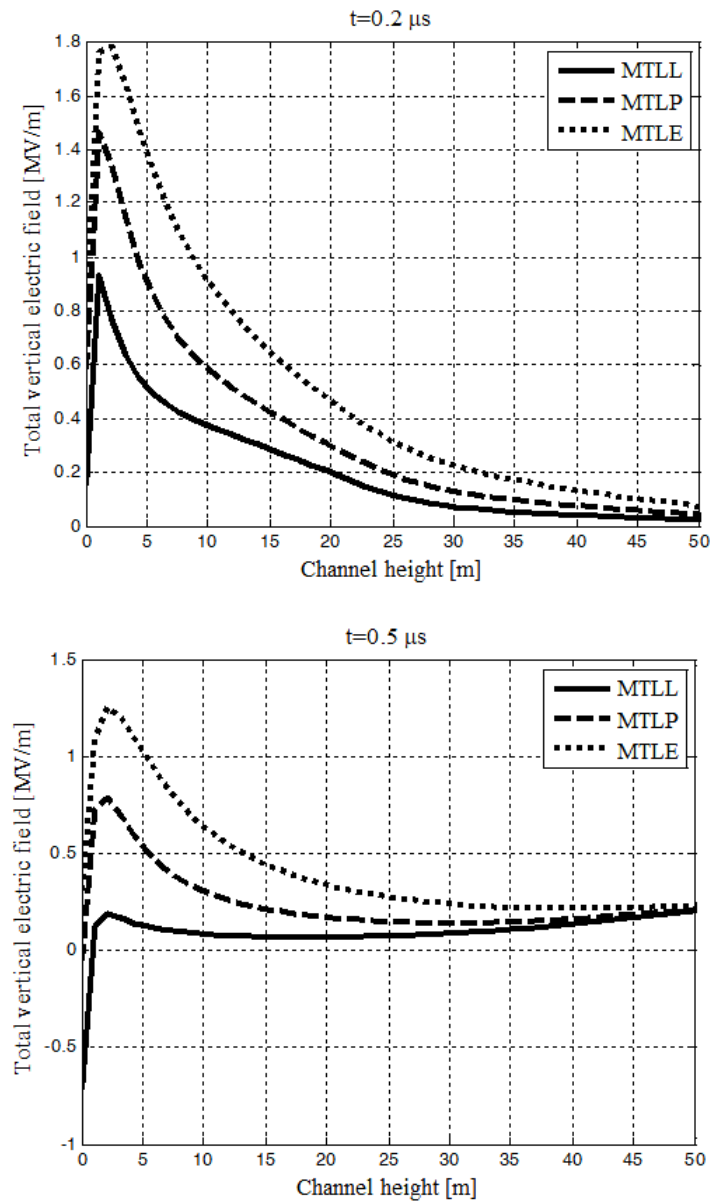
Figure 5.3: Total vertical electric field along the channel axis at $t = 0.2$ µs and $t = 0.5$ µs. Adapted from [73].
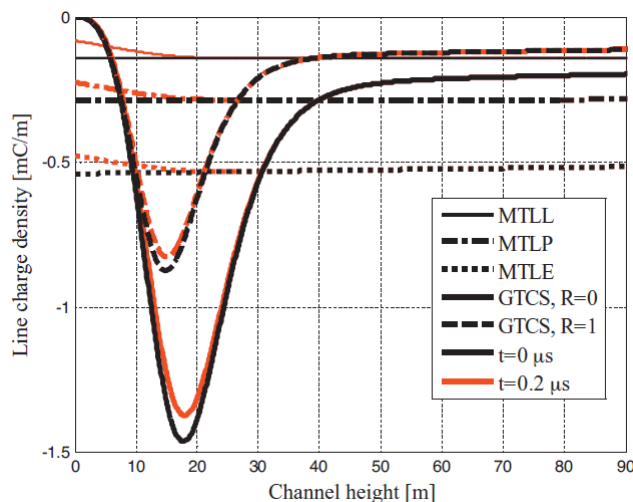
Figure 5.4: The line charge density versus height according to various return stroke models. Adapted from [73].

the case for $R = 0$, the return stroke velocity is set to $v = 0.56c$ (1.68×10^8 m/s) and the return stroke wave front is at 33.6 m. In the case for $R = 1$, the return stroke velocity is set to $v = 0.43c$ (1.29×10^8 m/s) and the return stroke wave front is at 25.8 m. The channel discharge function is adopted from [78]. It can be observed that the total electric field has the zero-crossing at about 33 m (in the case for $R = 0$) and at about 25 m (in the case for $R = 1$). In both cases it is just below the return stroke wave front. As expected, the graphs of the total field in both figures are similar in size and shape. Due to something greater return stroke velocity, the total electric field is a little greater in the case of $R = 0$. The zero-crossing of the field can be qualitatively described as follows: above the big charge accumulation depicted in Fig. 5.4, there is the point on the axis where the field generated by this charge accumulation equals the field generated by the rest of the channel charge above that point. The existence and the development of the net positive charge in zone 1 in time will not significantly change the z-coordinate of this point as it will be shown later. Further, the zero-crossing of the electric field will cause the infinite value of the channel core conductivity or even its negative value in the immediate vicinity above that point.

Magnitude of the vertical field at any point on the horizontal cross section of the corona sheath near channel base is shown in the Fig. 5.6. For the calculation, the GTCS model was used, and it was assumed that $R = 0$ and $t = 0.2$ µs from the time onset of the return stroke. In these two cases for this calculation, the observed channel height is 5.1m and 20m, the return stroke velocity is 0.56c and the return stroke wave front is at 33.6m.
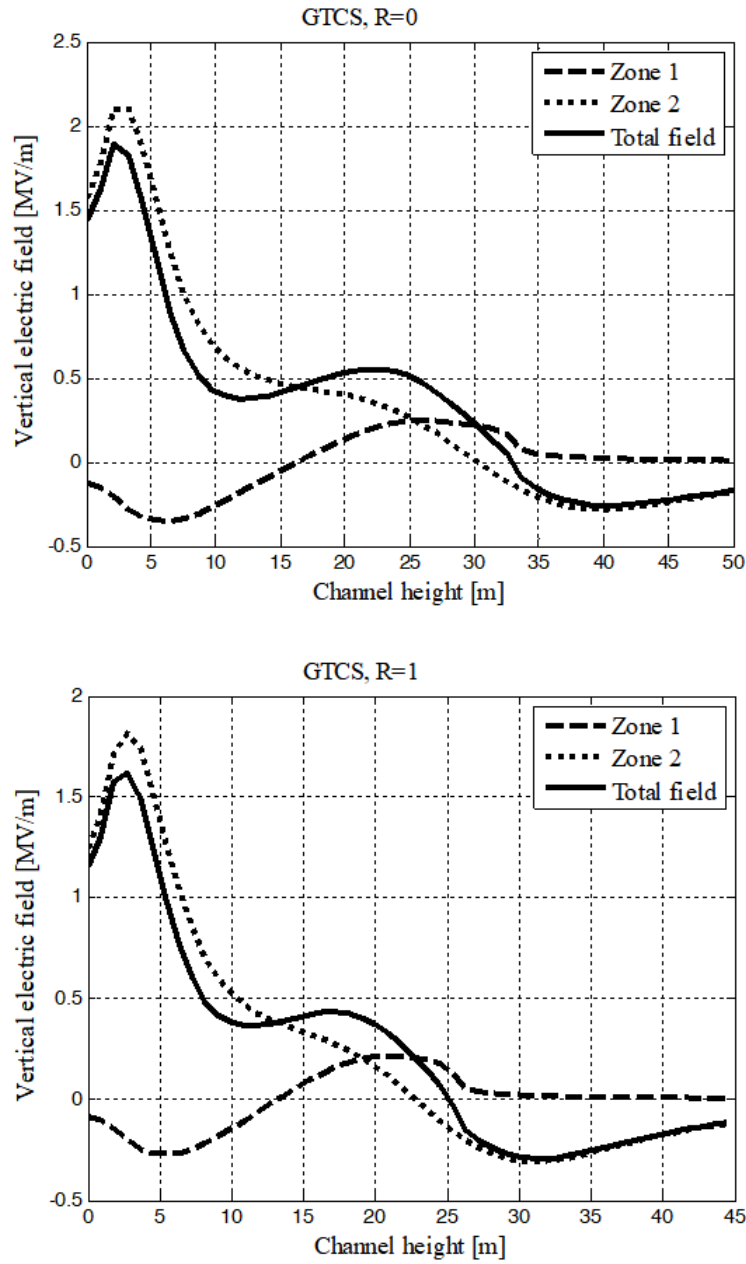
Figure 5.5: Vertical electric field along the channel axis at $t = 0.2$ µs of the discharge for the GTCS model for the ground reflection factors $R = 0$ and $R = 1$. The return stroke velocity isset to $v = 0.56$c ($v = 1.68 \times 10^8$) m/s. The data for the calculation are overtaken from [78].
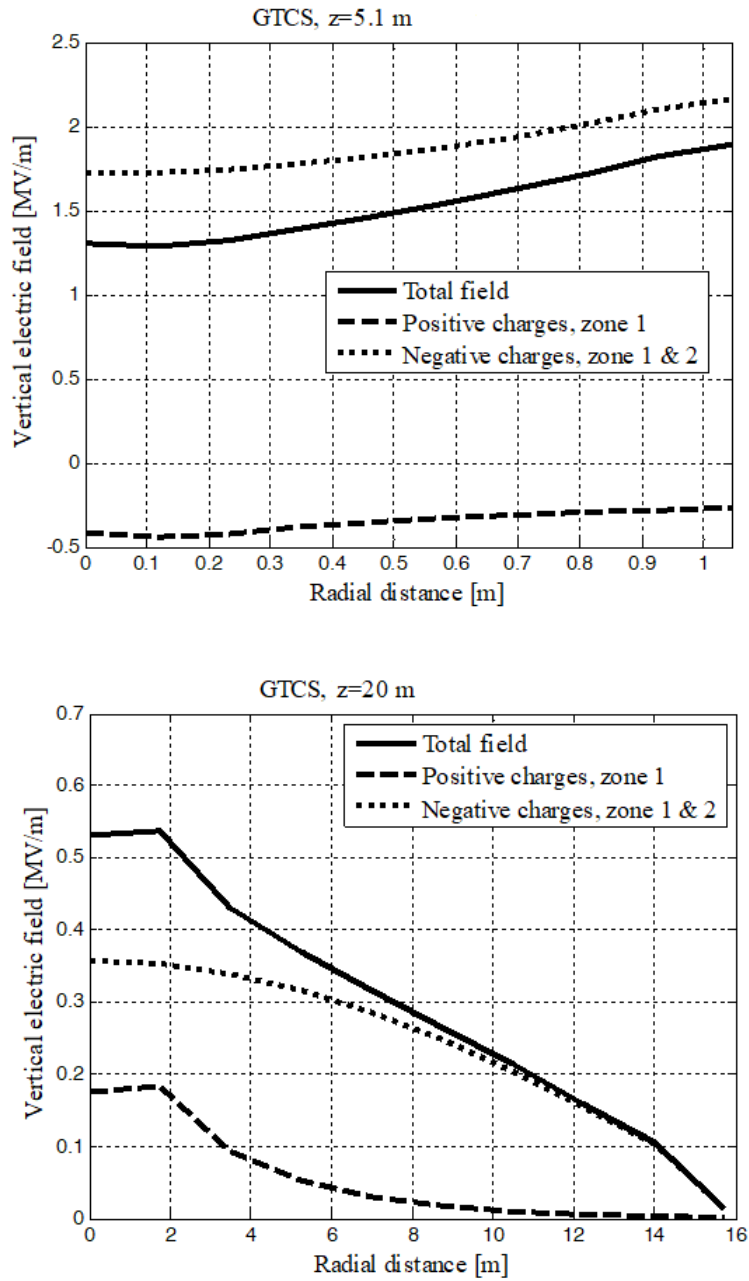
Figure 5.6: Vertical electric field inside the channel sheath versus radial distance from the core of the GTCS model. The current reflection factor is $R = 0$ and $R = 1$, $t = 0.2$ µs from the time onset of the return stroke. The return stroke velocity isset to $v = 0.56c$ ($v = 1.68 \times 10^8$) m/s. The data for the calculation are overtaken from [78].

However, at a distance of few centimeters from the channel axis, the total vertical field is very nearly constant in both cases. This can be explained, because the vertical electric field mainly depends on longitudinal charge distribution. Since the longitudinal channel dimension is much greater than the channel radius, the radial charge distribution does not significantly affect the change of the intensity of the vertical field. In general, this is no longer valid for higher altitude of the channel. It can be explained since the selected channel height was 20 m (very close to the maximum of the line charge density in the channel, Fig. 5.4). In this case, the magnitude of the vertical field strongly decreases with the radial distance. This behavior can be explained by the presence of the big accumulation of charge in the lower parts of the channel sheath.

5.2 Conductivity of the channel core

It is generally accepted that the temperature of lightning is around 30000 degrees centigrade that is about five times as hot as the surface of the Sun, while the electron densities in the channel core may exceed 10^{24} m^{-3} [34]. The lightning channel diameter can be measured by many experimental methods. In practice, there are several experimental methods for estimating the diameter of the lightning channel: photographic observation [74], measuring the diameters of fulgurites [75], measuring the dimensions of holes made by lightning flashes in metals [76], etc. The results obtained with these experiments show that the minimal value of the channel core diameter is estimated to be from 0.03 to 0.33 cm, while the maximal value of the channel core diameter is estimated to be from 0.3 to 3.5 cm.

The conductivity [1] of the lightning channel core is estimated to be of the order of 10^4 S/m, comparable to that of carbon [69]. Since the channel core represents the plasma column, its conductivity is, generally taken, function of numerous factors. Among many, the temperature (connected with the degree of ionization and the collision frequency), the kinetic pressure, the cross section for collisions, the concentration of charge, etc. should be mentioned. Moreover, it is well known that the magnetized plasmas are highly anisotropic i.e., the conductivity is in tensor form.

In the dissertation, it is calculated the longitudinal channel conductivity along the channel axis (in the center of the channel core) using the known current density distribution according to the corresponding return stroke model (for assumed channel core diameter) and the longitudinal (vertical) electric field caused by the transferred and the deposited charges during the discharge. The channel diameter

---

[1]in this calculation refers longitudinal channel conductivity along the channel axis

is assumed to be 1 cm. Therefore, the channel-core conductivity has a simple scalar form and it is calculated using well known relation between the electric field and the current density:

$$\sigma(z,t) = \frac{E_z(z,t)}{j_z(z,t)}.$$

(5.8)

5.2.1 Results of the calculation of the conductivity of the channel core

The results for the TLM are given in Figs. (5.7 - 5.10). As stated before, the magnitude of the critical radial electric field on the boundary of zones 1 and 2, respectively, in all cases are assumed. Leaving aside the negative value of the channel core, conductivity in the very base of the channel for the MTLL and the MTLP models (due to the negative vertical electric field mentioned in the previous section), the results clearly show the maximum of the order of 10^4 S/m for conductivity at about after the return stroke onset. The place of the maximal conductivity quickly rises during the discharge achieving over 150 m. The MTLP and the MTLL predict some smaller values for the conductivity but still in the range of the estimation since the channel core diameter (assumed to be 1 cm in this study) could be smaller increasing the channel core current density.

The GTCS model predicts similar results for the maximum conductivity for both values of the ground reflection factors. Excluding the unreal results for the conductivity at about 33 m and 25 m ($R = 0$ and $R = 1$, respectively) the maximum value of the order of 10^4 S/m for the conductivity is calculated. The height of the channel core with maximal conductivity is slightly greater than 50 m and it is more or less constant during the discharge. As stated before, the unreal results for the conductivity for the GTCS model are caused by the change of the field direction at the height located above the charge accumulation in the channel.
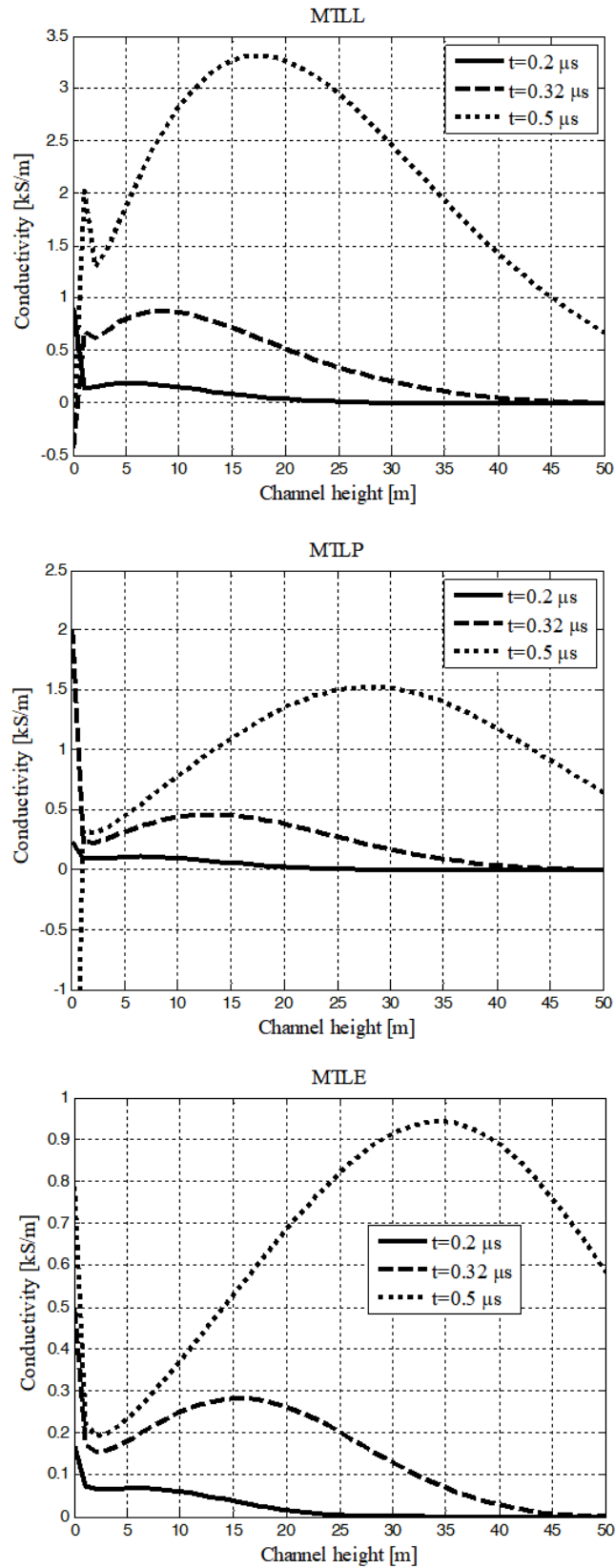
Figure 5.7: Conductivity along the channel core versus channel height for MTLL, MTLP and MTLE model in different instant of time 0.2 µs, 0.32 µs and 0.5 µs. The return stroke wave front was at 33.6, 53.8 and 84 m, respectively. Adapted from [73].
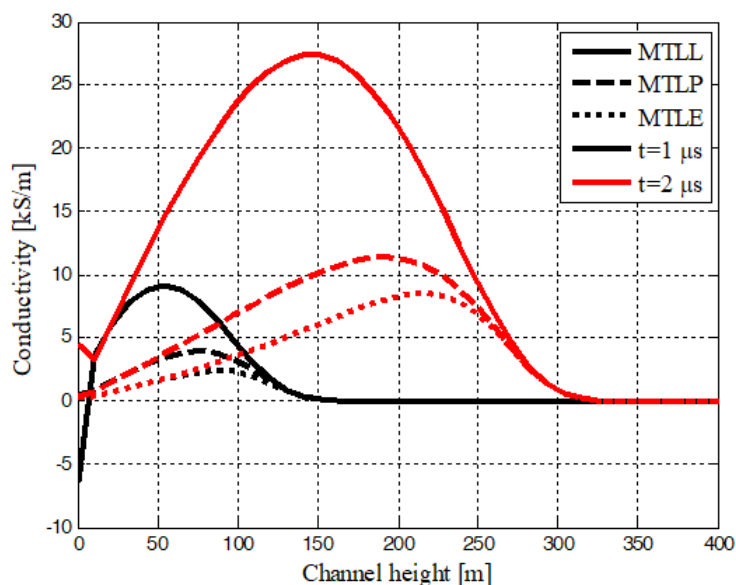
Figure 5.8: Conductivity of the channel core versus channel height for MTLL, MTLE model in different instants of time, at 1 μs and 2 μs. The return stroke wave front at $168, 336$m, is calculated respectively. Adapted from [73].

5.3 Influence of current reflections from the ground on corona sheath dynamics

The effect of the ground reflection coefficient, $\Gamma = R$, on the dynamics of the lightning channel is considered. Also, it was adopted the assumption from literature that ground coefficient depends on current magnitude and that is time-dependent:

$$\Gamma_i(t) = \Gamma_{0i} \cdot \exp(-k_i \cdot t), i = 1, 2, ... \tag{5.9}$$

where $\Gamma_{0i}(i_{0i})$ is the ground reflection coefficient at the striking point which is non-linear and depends on the current magnitude, and k_i is the exponential current decay constant [88].

Behavior of ground reflection coefficients takes into account the change of ground resistance during the return stroke. The channel-base current is separated into two components:

1. **first component** - this is a fast current component with a peak value over 15 kA, which reflects from the ground with current reflection coefficient $\Gamma = 1$;

2. **second component** - this is a slower current component with current reflection coefficient $\Gamma < 1$.
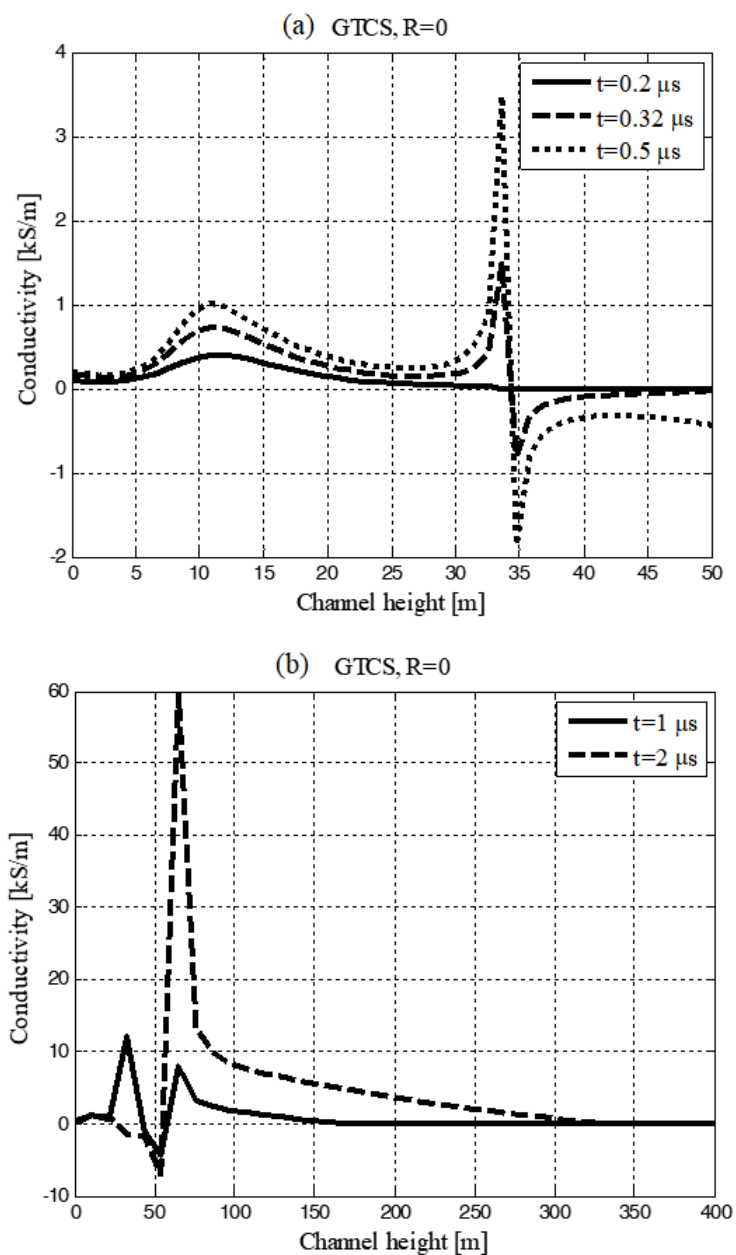
Figure 5.9: Conductivity along the channel core versus channel height for the GTCS model ($R = 0$) at various instants of time. The return stroke velocity is 0.56c (1.68×10^8m/s). (a) The conductivity at 0.2 µs, 0.32 µs and 0.5, µs, the return stroke wave front was at 33.6, 53.8 and 84m, respectively. (b) The conductivity at 1 µs and 2 µs, the return stroke wave front was at 168m and 336m, respectively. Adapted from [73].
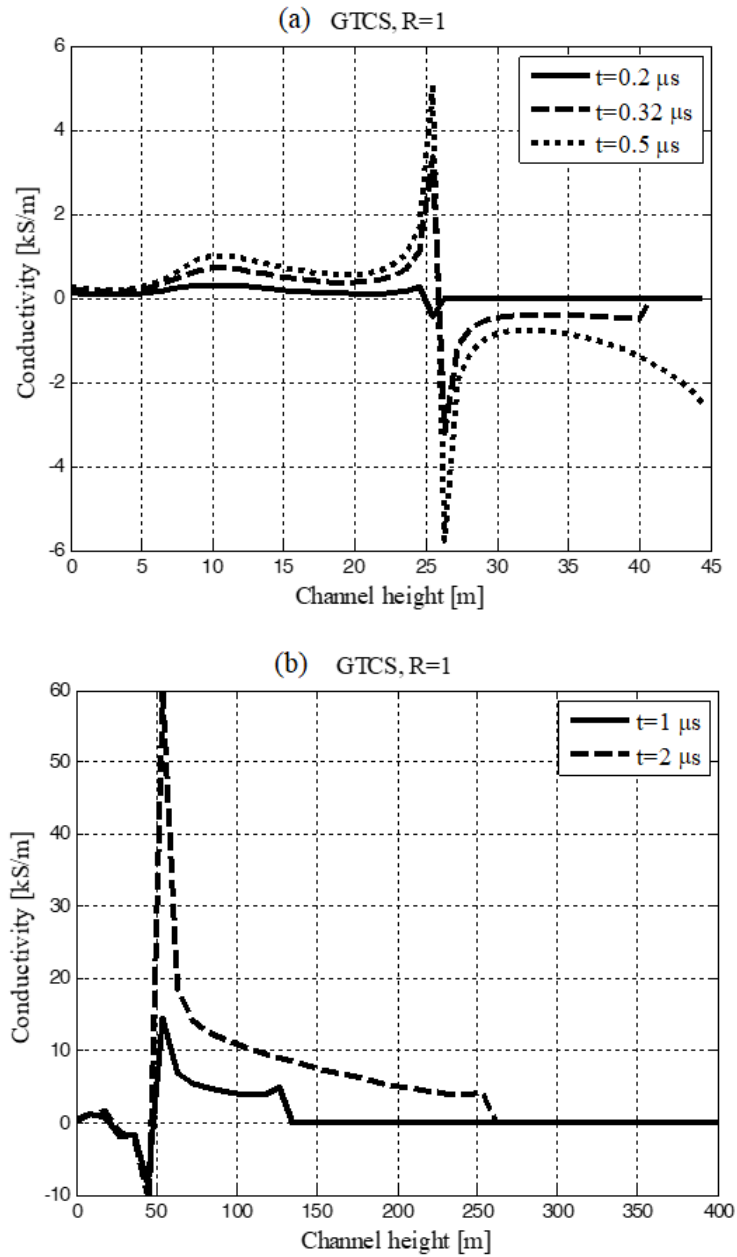
Figure 5.10: Conductivity along the channel core versus channel height for the GTCS model ($R = 1$) at various instants of time. The return stroke velocity is 0.43c (1.29×10^8m/s). (a) The conductivity at 0.2 µs, 0.32 µs and 0.5, µs , the return stroke wave front was at 33.6, 53.8 and 84m, respectively. (b) The conductivity at 1 µs and 2 µs, the return stroke wave front was at 129m and 258m, respectively. Adapted from [73].

These two components are reflected from perfect ground. The component with current reflection coefficient $\Gamma < 1$ produces transient negative line charge density along the channel core at the bottom of the lightning channel. According to the studies of Thottappillil et al. [87], the transition line charge densities for TCS-type models, along the channel core, are:

$$q_{tr}(t) = -\frac{1-\Gamma}{1+\Gamma} \cdot \frac{i_0(t)}{c}, \tag{5.10}$$

where, in practice, the coefficient $0 \leq \Gamma < 1$. From this follows that the total transition line charge given by Eq. (5.10) is negative. For the extended GTCS model, transition line charge is given by:

$$q_{tr}(t) = -\frac{1}{c} \cdot \sum_{n=1}^{2} i_{0i}(t) \cdot \frac{1-\Gamma_i(t)}{1+\Gamma_i(t)}, \tag{5.11}$$

$q_{tr}(t)$ enhances the negative radial electric field in the channel sheath [88]. This field forces the overcompensated positive charges to move into the corona sheath, so as to satisfy the boundary conditions between the channel core and the ground. The excess of positive charge generates the overcompensated positive electric field in most horizontal electric field measurements performed close to the channel core. Since $q_{tr}(t)$ is directly proportional to the channel-current, it disappears when the return stroke process is completed.

A new charging function f^+, according to complex iterative procedure [88] is calculated:

$$f^+ = f_0^+ + f_{ad}^+, \tag{5.12}$$

where f_0^+ is the channel charging function without the influence of transition charge, while the f_{ad}^+ is channel charging function due to the influence of transition charge.

The best way to determine the validity of the new approach, is to replace the expression for the new function f^+ in the formula for close electric field:

$$E = \frac{q_0^+}{2\pi\varepsilon_0 r} \cdot (f^+ - 1) - \frac{q_{tr}}{2\pi\varepsilon_0 r}, \tag{5.13}$$

and compare calculated and measured data. Total electric field near the channel is produced by transition charge located at the channel core and the charges in the corona sheath.

A comparison of close electric fields, calculated on the basis of the Eq. (5.13) and measured in experiments, is shown in the Fig. 5.11. The results for return stroke 1 shows very good matching with experimental results. In contrast to this,

more discrepancies are seen for stroke 3.
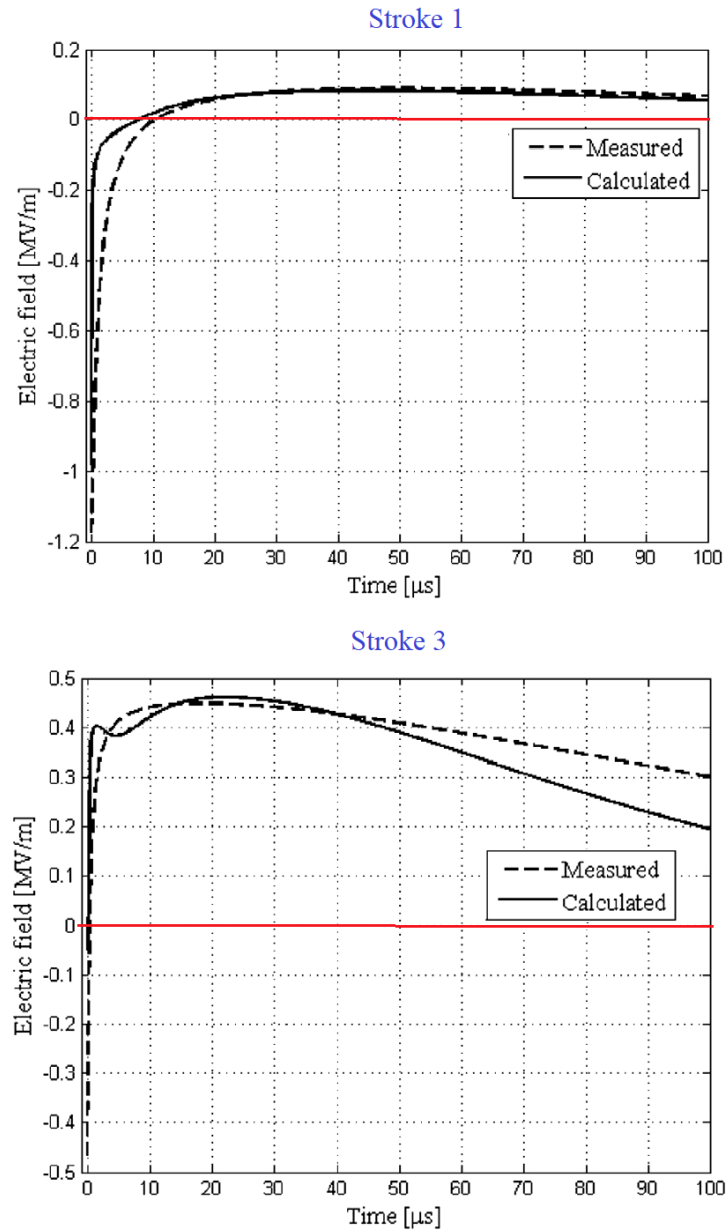
Figure 5.11: Measured and calculated curves of electric field versus time during return strokes 1 and 3 in flash S0033. Adapted from [88].

5.4 Experimental results

The experimental results from studies [80] and [81] are used to verify calculation results. It is important to note that plasma satisfies the LTE condition in the

channel when the electron density range is $(10^{17} - 10^{18})$ cm^{-3}.

First, the internal electric field and conductivity of lightning are studied in detail. The theoretical results are in good agreement with experiment. Based on the experimental results and Eqs. 4.1, 4.3, 4.4, 4.5 and 4.6, all based physical quantities that monitor the evolution of lightning channel are calculated and shown in Tab 5.1. In the Tab 5.1, T is the temperature of the channel, E_{int} is the average internal field in the channel, σ represents the conductivity of lightning channel, i represents the peak current, R is the longitudinal resistance [2] and r is the radius of lightning channel.

Table 5.1: Lightning channel parameters in six return strokes [81].

Stroke	T (K)	σ ($\times 10^4$S/m)	i (kA)	r (cm)	R (Ω/m)	$E_{int}(\times 10^4$ V/m)
R_0	27480	2.123	43.59	1.59	0.059	2.57
R_1	26140	2.085	13.56	0.94	0.172	2.33
R_2	26670	2.238	8.21	0.84	0.201	1.65
R_3	26560	2.172	9.66	0.87	0.194	1.87
R_4	26860	1.964	28.22	1.50	0.072	2.03
R_5	26860	1.964	28.22	1.50	0.072	2.03

Longitudinal resistance can be calculated based on calculated conductivity, radius of the lightning channel and Eq. (4.5). From the Tab. 5.1 it follows that the mean value of resistance longitudinal resistance for the six return strokes is 0.15 Ω/m. By comparison, longitudinal resistance of copper wire is about 5×10^{-3} Ω/m, provided the radius r is 1 cm and the temperature is 293 K [81]. This result is two orders of magnitude lower than the lightning channel. The internal electric field inside the lightning channel is of the order of 10^4 V/m, which is much lower than the breakdown electric field in the air (this value is approximately about 10^6 V/m). The length of the lightning channel is 3 - 4km, the resistance of the channels is measured by hundreds of ohms, and the voltage between the two ends of the lightning is 100 MV.

Another contribution is reflected in the fact that it is shown the horizontal electric field along a certain intersection is constant, Fig. 5.6, as Baum [28] assumed in the theoretical study.

Based on the obtained results and characteristic physical parameters, lightning discharge could be compared to arcs. But, unlike the electric arc, all the physical mechanisms that take role inside the lightning channel during discharge are not yet known. The dynamics of the lightning channel can be studied in detail using the

---

[2]longitudinal resistance is the resistance of lightning channel per unit length

GTCS model (only this model from a group of engineering models allows studying these phenomena). The first step towards this study is the precise calculation of channel discharge function, because in this model all important physical quantities are expressed through this function.

Chapter 6

Algorithms for the calculation of the channel discharge function

For studying the lightning channel dynamics according to the GTCS return stroke model, it is necessary to calculate the channel discharge function precisely. In contrast to the previous procedures, where channel discharge function was obtained based on the experiment and simplified electrostatic formulas, in this procedure, the channel discharge function is calculated from Volterra integral equation of the first kind. This function derives from the GTCS model. For the calculation, three methods are proposed.

6.1   Volterra Integral Equation

From a mathematical point of view, this procedure represents a study of nonlinear, nonhomogeneous Volterra integral equation of the first kind. Problems with these equations are classical problems in numerical analysis and many authors have solved it, but only a small number of them succeeded in the process of solving of such an equation with impulse function. Volterra integral equations of the first kind (first-kind VIE) are inherently ill-posed problems, meaning the equation solutions are generally unstable. It means that a small error in the input data can lead to a divergent solution, which significantly complicates the numerical solution of integral equations. First-kind VIE provides the description of the time evolution of lightning channel on a micro-second time scale following a dynamic of a physical process.

First of all, the basic things about integral equations will be mentioned. In mathematics theory, integral equations are equations in which an unknown function appears under the integral sign. If one limit of integration is variable, the equation is called VIE. If the unknown function is only under integral, the equation is called

first-kind VIE and it can be written in the following form:

$$f(t) = \int_a^t K(t,s) \cdot x(s)ds, \tag{6.1}$$

where $f(t)$ is known function, $x(s)$ is unknown function to be solved and $K(t,s)$ is another function of two variables (often called Kernel). If the function $f(t)$ is identically zero, the equation is called a homogeneous integral equation and if it is nonzero, it is called an inhomogeneous integral equation [90]. VIE was introduced by Vito Volterra and studied by Traian Lalescu in his dissertation in 1908. The title of this dissertation is "Sur les équations de Volterra" and it is written under the supervision of Charles Émile Picard.

It starts from the first-kind VIE, as shown in Chapter 3 in Eq. (3.25):

$$i_{\text{cb}}(t) = \int_0^{v^*t} q_0'(z) \frac{\partial}{\partial t} f(t - z/v^*) \, \mathrm{d}z, \tag{6.2}$$

where $f(t - z/v^*)$, while the other functions are known and presented in the Eqs. (3.24), (3.30), (3.32) and (3.33). According to the physics of electrical discharges, solution must satisfy the following physical conditions which are given in Eqs. (3.20), (3.21), (3.22) and (3.23).

According to Eq. (6.2), this is a inhomogeneous first-kind VIE. It can be simplified by introducing the following transformation $f_1(t - z/v^*) = \frac{\partial}{\partial t} f(t - z/v^*)$ in the equation (6.2), in which Eq. (6.2) becomes:

$$i_{\text{cb}}(t) = \int_0^{v^*t} q_0'(z) f_1(t - z/v^*) \mathrm{d}z. \tag{6.3}$$

The shift $z = v^*\tau$ is introduced, taking $q_0'(z) = q_0'(v^*\tau) = q(\tau)$ and $i(t) = i_{cb}/v^*$. The integration over $[0, v^*t]$ reduces to the interval $(0, t)$ and Eq. (6.3) becomes an equation on convolution type:

$$i(t) = \int_0^t q(\tau)f_1(t-\tau)\mathrm{d}\tau = \int_0^t q(t-\tau)f_1(\tau)\mathrm{d}\tau, \quad t > 0. \tag{6.4}$$

6.2 Overview of methods

As will be seen bellow, analysis of VIE of the convolution type shows that these equations model ill-posed problems. The mathematical term **well-posed problem** was defined by Jacques Hadamard [94]. According to Hadamar, the problem is well-posed if: it has a solution (**existence**), the solution is unique (**uniqueness**) and the solution depends continuously on given data (**stability**). The condition

of stability is the small changes in data will produce small changes in the solution. These problems can be described as "natural".

If one of three conditions is not met, the problem is **ill-posed**. In ill-posed problems, it is necessary to find some distribution from the final solution and its solution is indeed very sensitive to disturbances of the final state. Inverse problems are often ill-posed. Although they are typically continuous in terms of functional analysis, the search for a numerical solution using discrete methods ("discretization" of space and time) proves intrinsically unstable. For example, simple rounding errors in the data or increasing the accuracy of the method exert a "considerable" effect on the results. An unstable solution is much dependent on the input data and it is totally inadequate for most practical problems. A satisfactory solution must be stable even if the input data is changed.

If the problem is ill-posed, then its formulation needs to be changed; usually some additional assumptions are introduced for this, such as the smoothness assumption of the solution. This procedure is called regularization, with the most widely used Tikhonov regularization [91]), applicable to linear ill-posed problems. The Eq. (6.4) is very sensitive to perturbations in the parameters. Therefore, its solving is not easy and requires a special treatment. Sometimes, it is necessary to divide the interval into several sub-segments.

Three methods for solving the VIE of convolution type Eq. (6.4) are proposed in this dissertation ([92], [93]):

- Modified composite trapezoidal formula-MCTF;

- Laplace transform method;

- Convolution quadrature method.

Each physical event can be modeled mathematically in applied science. So, it is very important to have analytical solutions of the models, because these solutions give information about the character of the modeled event. On the other hand, when there is an analytical solution, the absolute error of each method can be determined.

In order to investigate the accuracy and stability of VIE solutions, numerical solution (Modified composite trapezoidal formula) is compared with analytical solution (Laplace transform method) and Convolution quadrature method. It was tested how the solution changes with increasing and decreasing the number of points, and whether the solution converges or not. Another very important characteristic is the speed of the convergence solutions.

6.2.1   Modified composite trapezoidal formula - MCTF

The direct discretization and applications of quadrature formulas that are modified according to the needs of problems are used. The choice of quadrature formulas is quite large, but there is a certain limit. However, only low-order quadrature formulas (midpoint quadrature or trapezoidal quadrature) give an algorithm that is not divergent [89]. In this dissertation, the trapezoidal rule was use. As a result, core and corona channel discharge function are obtained. However, from a mathematical point of view there are two cases. However, the most important thing is whether the line charge density function at the initial moment is equal to zero or different from zero, i.e. whether it is ($q_0' = 0$) or ($q_0' \neq 0$). Depending on this, various methods for problem solving have been applied.

- **Quadrature method (type of function $q'(0) \neq 0$)**

In this approach, it starts from the Eq. (6.4). It will be performed on the interval $[0, T_{max}]$ to construct a solution of equation. The values of independently variable t are in the interval $t \in [0, T_{max}]$ and the maximum number of points is N_{max}, so the step can be obtained as $h = \frac{T_{max}}{N_{max}}$ (the mesh is uniform over the whole interval). The Eq. (6.4) can be written in the discrete form as:

$$i_k = i(kh) = \int_0^{t_k} q(t_k - \tau) \cdot f_1(\tau) \mathrm{d}\tau. \tag{6.5}$$

When the integral from the Eq. (6.5) is replaced with trapezoid quadrature formulas, it was obtained the system of linear equation in the matrix form:

$$I = \frac{h}{2} \cdot Q \cdot \widetilde{F}_1, \tag{6.6}$$

wherein the matrices in the Eq. (6.6) have the form:

$$
Q = \begin{bmatrix}
q(0) & 0 & 0 & 0 & \cdots & 0 \\
q(h) & q(0) & 0 & 0 & \vdots & 0 \\
q(2h) & q(h) & q(0) & 0 & \vdots & 0 \\
q(3h) & q(2h) & q(h) & q(0) & \vdots & 0 \\
\vdots & \vdots & \vdots & \vdots & \ddots & \vdots \\
q(N_{max}h) & 2q((N_{max}-1)h) & \cdots & \cdots & \cdots & q(0)
\end{bmatrix},
$$

$$
\widetilde{F}_1 = \begin{bmatrix}
\widetilde{f}_0 \\
\widetilde{f}_1 \\
\widetilde{f}_2 \\
\widetilde{f}_3 \\
\widetilde{f}_4 \\
\vdots \\
\widetilde{f}_n
\end{bmatrix}, \qquad
I = \begin{bmatrix}
i_0 \\
i_1 \\
i_2 \\
i_3 \\
i_4 \\
\vdots \\
i_n
\end{bmatrix}, \qquad
J = \begin{bmatrix}
J(t_0) \\
J(t_1) \\
J(t_2) \\
J(t_3) \\
J(t_4) \\
\vdots \\
J(t_n)
\end{bmatrix}. \tag{6.7}
$$

System of Eq. (6.7) is simplify solved, because its matrix is the lower triangular matrix [100]. In this way, the matrix of discrete solutions $\widetilde{F}_1$ is given, and it is obtained the final result by interpolation.

• Quadrature method (type of function $q'(0) = 0$)

These problems are solved using a modified quadrature method. At the beginning of the interval, condition $q'_0 = 0$ converts the VIE of the convolution type into identity $0 = 0$. In this case, the solution is presented as a sum of two components:

- **approximate component** - the solution is given in the form of the Taylor series;

- **regular component** - the solution is obtained by the method of trapezoidal quadrature as in the method when the type of function is $(q'_0 \neq 0)$.

The approximate component of the solution exists in the interval, that is very close to zero, i.e. $\tau \in [0, \widehat{\tau}]$:

$$
f_1(\tau) = \sum_{\nu=1}^{N_{max}} a_\nu \tau^{\nu-1}. \tag{6.8}
$$

Number of terms in the Eq. (6.8) is determined according to the needs of calculation, although it should not be more than 10 members. The values of unknown

coefficients in Taylor's series are obtained by proceeding from Eq. (6.8) and obtaining system of linear equations that can be easily solved. This solution will be used to solve the Eq. (6.4) on the whole interval ($0 \leq t \leq T_{max}$). The following equation is obtained by integrating the equation over the entire interval:

$$i(t) = \int_0^{\widehat{\tau}} q(t - \tau) \cdot f_1(\tau) \mathrm{d}\tau + \int_{\widehat{\tau}}^t q(t - \tau) \cdot f_1(\tau) \mathrm{d}\tau. \tag{6.9}$$

The first integral on the right-hand side of the Eq. (6.9) can be calculated for each t, in the label $J(t)$, because it is known the analytical expression for $q_0'(z)$ for any argument (in our example the argument is $(t - \tau)$) and expression (6.8) for $f_1(\tau)$ when $\tau \in [0, \widehat{\tau}]$. On the second interval, numerical integration was applied, as before, from $\widehat{\tau}$ to some vale $t = \widehat{\tau} + kh$. The next expression is obtained when Replacing the term from the Eq. (6.8) to Eq. (6.4):

$$J(t) = \int_0^{\widehat{\tau}} q(t - \tau) \cdot \left(\sum_{\nu=1}^{N_{max}} a_\nu \tau^{\nu-1} \mathrm{d}\tau \right) = \sum_{\nu=1}^{N_{max}} a_\nu \left(\int_0^{\widehat{\tau}} q(t - \tau) \tau^{\nu-1} \mathrm{d}\tau \right). \tag{6.10}$$

Adopting $\widehat{\tau} = t_0$, based on the Eq. (6.9), it is obtained:

$$i_k = i(t_k) = J(t_k) + \int_{t_0}^{t_k} q(t_k - \tau) \cdot f_1(\tau) \mathrm{d}\tau. \tag{6.11}$$

When generalization is made, a linear system of equations is obtained:

$$I = J + \frac{h}{2} \cdot Q \cdot \widetilde{F}_1. \tag{6.12}$$

Matrix representation is given in the Eq. (6.6). The system of equations is easily solvable. The discrete values are obtained as the solution of the equation on the second interval. Since the VIE is solved at both intervals, these data will be used to solve the equation over the entire interval. At the first interval there is a solution that is approximately. The analytical part of the solution will be sampled with a certain step to to obtain a discrete data set P_1. From the second interval, the discrete points obtained as the solution of the system 6.12 and will be put in the set P_2. A discrete solution on the whole interval will be given as a data union $P = P_1 \cup P_2$. The continuous solution can be obtained with interpolation discrete data and mark it with $f_1(t)$.

- **Final solution**

The continuous function $f_1(u)$ is obtained as a result of calculation. However, in some calculations it passes through the zero before the end of the interval T_{max},

The cause of this behavior is (probably) numerical instability, but this problem will be the subject of some future theoretical work. It is introduced a small modification in the final result and it is used it in the calculation.

For some high value of T, for example $T_{max} - h$, numerical derivate is calculated as:

$$f'_{1N} = \frac{f_1[T_{max} - h] - f_1[T_{max} - 2h]}{h}. \tag{6.13}$$

For $t > T_{max} - h$, the continual function $f_1(t)$ is approximated with:

$$f_{1A} = f_1[T_{max} - h] \cdot e^{-[\alpha \cdot (u - (T_{max} - h))]}, \tag{6.14}$$

and at this interval, the first derivative at a point $u = T_{max} - h$ is known:

$$f'_{1A} = -\alpha \cdot f_1[T_{max} - h]. \tag{6.15}$$

Parameter α can be obtained from identity $f'_{1A}(T_{max} - h) = f'_{1N}$:

$$\alpha = (f_1[T_{max} - 2h]/f_1[T_{max} - h] - 1)/h. \tag{6.16}$$

When the parameter α is calculated, the final solution can be expressed as:

$$f_{1rez} = \begin{cases} f_1(t) & , u \le T_{max} - h \\ f_1(T_{max} - h) \cdot e^{-[\alpha \cdot (u - (T_{max} - h))]} & , u \le T_{max} - h. \end{cases} \tag{6.17}$$

6.2.2   Laplace transform method

The theoretical approach in solving VIE implies the application of Laplace transformation. This is the standard method for finding the solution of the VIE of convolution type. The Laplace transform of a function $f_1(t)$ is the function $F_1(s)$ given by:

$$F_1(s) = \mathcal{L}[f_1(t)](s) = \int_0^\infty e^{-st} f_1(t) \, dt. \tag{6.18}$$

Its application to the convolution equation gives:

$$I(s) = Q(s)F_1(s), \tag{6.19}$$

where $I(s)$ and $Q(s)$ are Laplace transforms of $i(t)$ and $q(t)$.

For given function, direct Laplace transform is not possible. Because of this reason, it is used the Meijer G-function (Appendix A). To determine the required transformations, it is necessary to know the following integral:

$$G_k(\alpha) = \int_0^\infty e^{-\alpha x} \frac{x^k}{1+x^k}\, dx \qquad (\mathrm{Re}\,\alpha > 0,\; k \in \mathbb{N}). \qquad (6.20)$$

If the integral 6.20 is expressed over Meijer G-function, it is obtained:

$$G_k(\alpha) = \int_0^\infty e^{-\alpha x} \frac{x^k}{1+x^k}\, dx = \frac{1}{\sqrt{k(2\pi)^{k-1}}} G_{1,k+1}^{k+1,1}\left(\frac{\alpha^k}{k^k} \;\middle|\; \begin{matrix} -\frac{1}{k} \\ -\frac{1}{k}, 0, \frac{1}{k}, \frac{2}{k}, \ldots, \frac{k-1}{k} \end{matrix}\right). \qquad (6.21)$$

In fact, this result represents the Laplace transform of the function $\mathcal{L}[\psi_k(t)](s) = G_k(s)$. According to properties of the Laplace transform, it gets:

$$\mathcal{L}\left[\psi_k(t)e^{-\gamma t}\right](s) = G_k(s+\gamma). \qquad (6.22)$$

Thus, Laplace transformations can be found for functions $i(t)$ and $q(t)$, respectively. So, it gets (Appendix B):

$$I(s) = \mathcal{L}[i(t)](s) = A\tau_1 G_n\left(\tau_1\left(s+\tau_2^{-1}\right)\right), \qquad (6.23)$$

where G_n is given by Eq. (6.20) and the constant A is $A = I_0/(\eta \cdot v^*)$.

Laplace transformation for $q(t)$, $Q(s) = \mathcal{L}[q(t)](s)$ is given by (Appendix B):

$$Q(s) = \mathcal{L}[q(t)](s) = Q_0'\left\{\left(1 + \frac{\lambda_{d_1}}{v^*}s + \frac{\lambda_{d_2}}{v^{*2}}s^2\right)\hat{\tau}_1 G_m\left(\hat{\tau}_1\left(s+\hat{\tau}_2^{-1}\right)\right) - \frac{\lambda_{d_2}}{v^{*2}\hat{\tau}_1}\delta_{m,1}\right\}, \qquad (6.24)$$

where $\delta_{m,1}$ is Kronecker's delta symbol.

According to Eq. (6.19) and expressions for Laplace transformations (6.23) and (6.24), Laplace transform of the solution is obtained:

$$F_1(s) = \mathcal{L}[f_1(t)](s) = \frac{I(s)}{Q(s)} = \frac{A\tau_1 G_n\left(\tau_1\left(s+\tau_2^{-1}\right)\right)}{Q_0'\left\{\left(1+\frac{\lambda_{d_1}}{v^*}s + \frac{\lambda_{d_2}}{v^{*2}}s^2\right)\hat{\tau}_1 G_m\left(\hat{\tau}_1\left(s+\hat{\tau}_2^{-1}\right)\right) - \frac{\lambda_{d_2}}{v^{*2}\hat{\tau}_1}\delta_{m,1}\right\}}. \qquad (6.25)$$

As before, it can be can put $\lambda_{d_1} = v^*\tau_{d_1}$ and $\lambda_{d_2} = (v^*\tau_{d_2})^2$, where τ_{d_1} and τ_{d_2} are time discharge constants for given GTCS model. Then, it gets [92]:

$$F_1(s) = \frac{K\, G_n\left(\tau_1(s+\tau_2^{-1})\right)}{\left(1+\tau_{d_1}s+\tau_{d_2}^2 s^2\right)G_m\left(\hat{\tau}_1(s+\hat{\tau}_2^{-1})\right) - \left(\frac{\tau_{d_2}}{\hat{\tau}_1}\right)^2 \delta_{m,1}}, \qquad (6.26)$$

where $K = A(\tau_1/\hat{\tau}_1)/Q'_0 = I_0(\tau_1/\hat{\tau}_1)/(\eta v^* Q'_0)$.

Then, the inverse transforms of $F_1(s)$ can be done by:

$$f_1(t) = \mathcal{L}^{-1}[F_1(s)](t) = \frac{1}{2\pi i} \int_\Gamma e^{st} F_1(s) \, \mathrm{d}s, \qquad (6.27)$$

where Γ is a curve locates in the analytic region of $F_1(s)$ and can be chosen as running from $\infty \cdot e^{-i(\pi-\varphi)}$ to $\infty \cdot e^{i(\pi-\varphi)}$ [102]. It is important to note that the Laplace transform $F_1(s)$ is an analytic function in the region $|\arg(s - \sigma)| < \pi - \varphi$, with $\varphi < \pi/2$ and $\sigma \in \mathbb{R}$, and satisfies the condition $|F_1(s)| \leq M/|s|^\mu$ for some positive constants M and μ.

In general case, this complex integral cannot be computed in analytic form. In such cases it must be use some methods for its approximate computation for given $t > 0$. In the literature, there are several different methods for calculating inverse Laplace transformation ([95], [96], [97], [98]). By determining the values $f_1(t_\nu)$ on a particular discrete set $T = \{t_\nu\}_\nu$, the approximation formula can usually be obtained by interpolation (cf. [99], [101]), for the inverse transform of $F_1(s)$. Such solution will be called as the "exact" solution of the Volterra integral equation of convolution type, Eq. (6.4).

6.2.3   Convolution quadrature method

This method was developed by Austrian mathematician *Lubich* ([102], [103]) for integral equation of the convolution type. Thus, Lubich's convolution quadrature method can be expressed in the form:

$$\int_0^t q(\tau)f_1(t-\tau)\mathrm{d}\tau = \sum_{0 \leq jh \leq t} \omega_j(h)f_1(t-jh) + R(t; f_1), \quad t \geq 0, \qquad (6.28)$$

where $h > 0$ is the step size, $\omega_j(h)$ is the quadrature weights and it can be calculated numerically, while $R(t; f_1)$ is the corresponding remainder term. A detailed explanation of the Lubich method is given in the literature [104], [105]. Generally speaking, Lubich's convolution quadrature rule provides efficient approximations to integrals with a specific kernel type. In practice, when this quadrature is applied to the calculation of high oscillatory integrals, numerical tests show that the results are not good. For this reason, it is used an alternative method for calculating the convolution quadrature proposed in the study [106].

An alternative method for calculating quadrature weights $\omega_j(h)$ can be done in the following form:

$$\omega_j(h) = \int_0^\infty q(t)\phi_j(t/h)\mathrm{d}t, \tag{6.29}$$

using basis functions $\phi_j(t)$, $j = 0, 1, 2, \ldots$, given by the generating function. Backward differentiation formula (BDF) (Appendix C) is used to determine these functions. For example, the backward differentiation formula of order 1, (BDF1) is $\phi_j(t) = \mathrm{e}^{-t} \cdot \dfrac{t^j}{j!}$ and the backward differentiation formula of order 2, (BDF2) is $\phi_j(t) = \dfrac{H_j(\sqrt{2t})}{j!}\left(\dfrac{t}{2}\right) \cdot \mathrm{e}^{-3t/2}$, where $H_j(\cdot)$ denote the j-th Hermite polynomial. Recurrence relations for the CQ basis functions are given in the next scheme:

- **BDF1**

  Initial Basis function: $\phi_0(t) = \mathrm{e}^{-t}$

  Recurrence for Basis Function: $j\phi_j(t) - t\phi_{j-1}(t) = 0$

- **BDF2**

  Initial Basis function: $\phi_0(t) = \mathrm{e}^{-3t/2}$

  Recurrence for Basis Function: $j\phi_j(t) - 2t\phi_{j-1}(t) + t\phi_{j-2}(t) = 0$

- **BDF3**

  Initial Basis function: $\phi_0(t) = \mathrm{e}^{-11t/6}$

  Recurrence for Basis Function: $j\phi_j(t) - 3t\phi_{j-1}(t) + 3t\phi_{j-2}(t) - t\phi_{j-3}(t) = 0$

- **BDF4**

  Initial Basis function: $\phi_0(t) = \mathrm{e}^{-25t/12}$

  Recurrence for Basis Function: $j\phi_j(t) - 4t\phi_{j-1}(t) + 6t\phi_{j-2}(t) - 4t\phi_{j-3}(t) + t\phi_{j-4}(t) = 0$

In Eq. (6.6), it is used the basic functions $\phi(t)$ that are generated by equality Eq. (3.1) in study [107]:

$$\mathrm{e}^{-\delta(\zeta)t} = \sum_{j=0}^\infty \phi_j(t)\zeta^j,$$

where $\delta(\zeta) = \sum_{j=1}^k \frac{1}{j}(1-\zeta)^j$, $k = 1, \ldots, 6$.

Explicit formulas for $\omega_j(h)$ based on the backward difference formulas of the first and second order (BDF1 and BDF2) have been used in [108]:

$$\mathrm{e}^{-(1-\zeta)t} = \sum_{j=0}^\infty \phi_j(t)\zeta^j,$$

In particular, for BDF 1 (k=1) it gives:

$$e^{-(1-\zeta)t} = e^{-t} \sum_{j=0}^{\infty} \frac{t^j \zeta^j}{j!},$$

i.e., $\phi_j(t) = e^{-t} t^j / j!$, $j = 0, 1, 2, \ldots$ (known as Erlang functions in statistics). For BDF2 ($k = 2$), it gives:

$$e^{-\frac{1}{2}(3 - 4\zeta + \zeta^2)t} = e^{-3t/2} \sum_{j=0}^{\infty} \frac{H_j(\sqrt{2t})}{j!} \left(\frac{t}{2}\right)^{j/2} \zeta^j,$$

where $H_j(\sqrt{2t})$ is the Hermite polynomial of degree j. The basic functions are:

$$\phi_0(t) = e^{-3t/2}, \quad \phi_1(t) = 2e^{-3t/2}t, \quad \phi_2(t) = \frac{1}{2}e^{-3t/2}t(4t - 1),$$

$$\phi_3(t) = \frac{1}{3}e^{-3t/2}t^2(4t - 3),$$

$$\phi_4(t) = \frac{1}{24}e^{-3t/2}t^2\left(16t^2 - 24t + 3\right), \quad \phi_5(t) = \frac{1}{60}e^{-3t/2}t^3\left(16t^2 - 40t + 15\right),$$

$$\phi_6(t) = \frac{1}{720}e^{-3t/2}t^3\left(64t^3 - 240t^2 + 180t - 15\right),$$

$$\phi_7(t) = \frac{1}{2520}e^{-3t/2}t^4\left(64t^3 - 336t^2 + 420t - 105\right),$$

$$\phi_8(t) = \frac{1}{40320}e^{-3t/2}t^4\left(256t^4 - 1792t^3 + 3360t^2 - 1680t + 105\right),$$

$$\phi_9(t) = \frac{1}{181440}e^{-3t/2}t^5\left(256t^4 - 2304t^3 + 6048t^2 - 5040t + 945\right),$$

$$\phi_{10}(t) = \frac{1}{3628800}e^{-3t/2}t^5\left(1024t^5 - 11520t^4 + 40320t^3 - 50400t^2 + 18900t - 945\right), \quad \text{etc.}$$

These basis functions $\phi_j(t)$, $j = 0, 1, \ldots, 8$, for $k = 1$ and $k = 2$, are resented in Fig. 6.1. In a similar way, the basic functions for $k \geq 3$ can be obtained.

The main problem in numerical computation of the quadrature weights $\omega_j(h)$ given by Eq. (6.5) there can be slow convergence of the corresponding quadrature rule, due to the proximity of the singularities of the function $q(t)$ around the origin $t = 0$. The extension of the function $\hat{g}(t)$ to the complex plane $\mathbb{C}$ has some singularities at the points $\hat{\tau}_1 \exp\left(i\frac{(2k+1)\pi}{m}\right)$, $k = 0, 1, \ldots, m - 1$. These singularities are also present in the function $q(t)$ (extended to $\mathbb{C}$), only with higher order. As a suitable transformation for the elimination of singularities in the integration process, it can be taken:
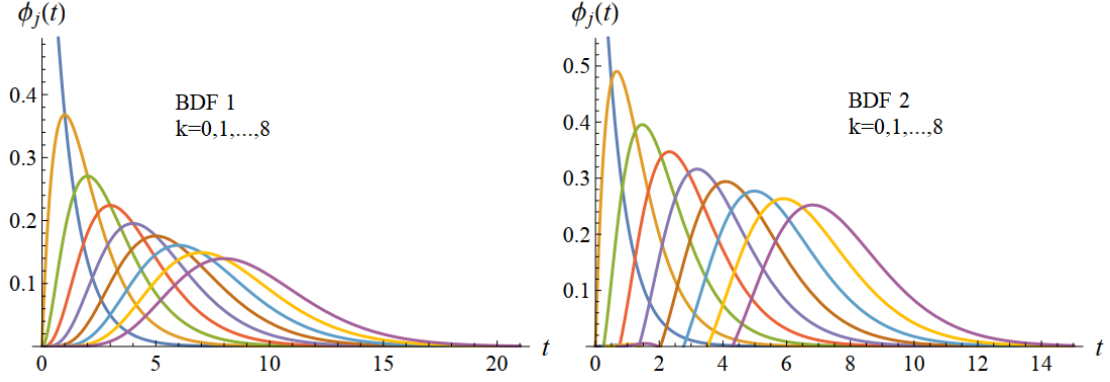
Figure 6.1: Basis functions according to the [92].

$$t = \hat{\tau}_1 \sinh^{2/m} \xi \qquad \left(dt = \frac{2\hat{\tau}_1}{m} \sinh^{2/m-1} \xi \cosh \xi d\xi \right). \qquad (6.30)$$

6.3   Results and discussion

In this section, the results of calculation will be given. Example 1 was done in detail with all three methods. The advantages and disadvantages of each method are described. For other examples, only the final results are given, which are the most important for further calculations.

- **Example 1**

  The example with the following data is considered:

- $I_0 = 13000 \, [\text{A}], \quad \tau_1 = 24 \times 10^{-8} \, [\text{s}], \quad \tau_2 = 3.4 \times 10^{-6} \, [\text{s}], \quad \eta = 0.87, \quad n = 5;$

- $Q_0' = -1.885 \times 10^{-4} \, [\text{C/m}], \quad \lambda_1 = 4.5 \, [\text{m}], \quad \lambda_2 = 255 \, [\text{m}], \quad \lambda_{d_1} = 45 \, [\text{m}],$
  $\lambda_{d_1} = 0 \, [\text{m}], \quad m = 4,$

  as well as

$$c = 3 \times 10^8 \, [\text{m/s}], \quad v = \frac{c}{3} = 10^8 \, [\text{m/s}], \quad v^* = \frac{v \, c}{v + c} = 7.5 \times 10^7 \, [\text{m/s}].$$

The problem will be considered on the interval $[0, T_{\max}]$, where $T_{\max} = 20 \times 10^{-6} \, [\text{s}]$.

- **Example 1 - Laplace transform method**

Thus, in this case, it gets

$$i(t) = \frac{I_0}{\eta v^*} \cdot \frac{t^5}{\tau_1^5 + t^5} \mathrm{e}^{-t/\tau_2} \quad \text{and} \quad q(t) = \widehat{Q}_0 \frac{t^3(t^5 + a_1 t + a_0)}{(t^4 + \hat{\tau}_1^4)^2} \mathrm{e}^{-t/\hat{\tau}_2}, \qquad (6.31)$$

where, $\hat{\tau}_1 = 6 \times 10^{-8}$ [s] and $\hat{\tau}_2 = 3.4 \times 10^{-6}$ [s], as well as:

$$\frac{I_0}{\eta v^*} = \frac{13}{65250} \, [\mathrm{C/m}] = 1.992337164750958 \times 10^{-4} \, [\mathrm{C/m}],$$

$$\widehat{Q}_0 = -1.552352941176471 \times 10^{-4} \, [\mathrm{C/m}],$$

$$a_1 = a_1 = 1.296 \times 10^{-29} \, [\mathrm{s}^4] \quad \text{and} \quad a_0 = 3.777 \times 10^{-35} \, [\mathrm{s}^5].$$

Using Eq. (6.26), the Laplace transform of $f_1(t)$ in terms of the Meijer function is obtained:

$$F_1(s) = \frac{C}{1 + \tau_{d_1} s} \cdot \frac{G_{1,6}^{6,1}\left(\frac{\tau_1^5}{3125}(s + \tau_2^{-1})^5 \,\middle|\, \begin{matrix} -\frac{1}{5} \\ -\frac{1}{5}, 0, \frac{1}{5}, \frac{2}{5}, \frac{3}{5}, \frac{4}{5} \end{matrix} \right)}{G_{1,5}^{5,1}\left(\frac{\hat{\tau}_1^4}{256}(s + \hat{\tau}_2^{-1})^4 \,\middle|\, \begin{matrix} -\frac{1}{4} \\ -\frac{1}{4}, 0, \frac{1}{4}, \frac{1}{2}, \frac{3}{4} \end{matrix} \right)}, \qquad (6.32)$$

where

$$C = \frac{K\sqrt{m}}{\sqrt{n(2\pi)^{n-m}}} = \frac{I_0}{\eta v^* Q_0'} \cdot \frac{\tau_1}{\hat{\tau}_1} \sqrt{\frac{m}{n(2\pi)^{n-m}}} = -\frac{6400}{7569} \sqrt{\frac{10}{\pi}} = -1.508573701067213$$

and

$$\tau_{d_1} = 6 \times 10^{-7} \, [\mathrm{s}], \quad \tau_1^5 = 7.962624 \times 10^{-34} \, [\mathrm{s}^5], \quad \hat{\tau}_1^4 = 1.296 \times 10^{-29} \, [\mathrm{s}^4],$$

$$\tau_2^{-1} = \hat{\tau}_2^{-1} = 294117.6470588235 \, [1/\mathrm{s}].$$

Applying the Gaver method [95], the numerical values of $f_1(t)$ is determined for given $t \in [0, T_{\max}]$. According to the behavior of the function $f_1(t)$, the interval $[0, T_{\max}]$ is diveded into six subintervals:

$$[0, T_{\max}] = \left[0, \tfrac{T_{\max}}{200}\right] \cup \left[\tfrac{T_{\max}}{200}, \tfrac{T_{\max}}{50}\right] \cup \left[\tfrac{T_{\max}}{50}, \tfrac{3T_{\max}}{50}\right] \cup \left[\tfrac{3T_{\max}}{50}, \tfrac{T_{\max}}{10}\right] \cup \left[\tfrac{T_{\max}}{10}, \tfrac{T_{\max}}{2}\right] \cup \left[\tfrac{T_{\max}}{2}, T_{\max}\right],$$

and take in each of these subintervals 6, 75, 40, 20, 40, 25 equidistant points, respectively. The obtained values of the function $f_1(\tau_\nu)$ in these points τ_ν (blue points), as well as the corresponding interpolation function, i.e., the "exact" solution (red line), are presented in Fig. 6.2 on interval $[0, T_{\max}/5]$.
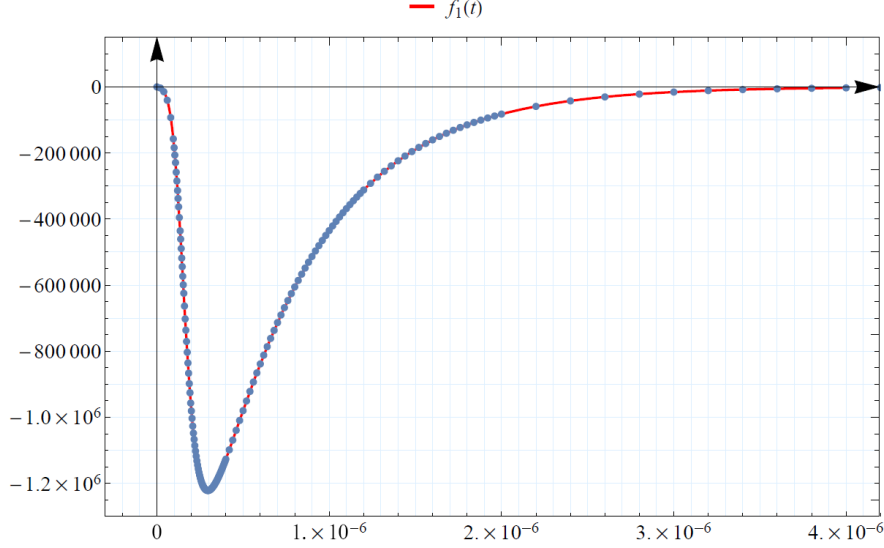
Figure 6.2: The solution $f(t)$ obtained by numerical inversion of Laplace transformation using Gaver method on interval $[0, T_{\max}/5]$. Adapted from [92].

Finally, it should be noted that this type of numerical inversion takes a long time. For example, procedure for the numerical inversion lasts 30 minutes. The inverse Laplace transform calculation for this example is performed in Wolfram Mathematica, Ver. 11.3, on the computer which has the following configuration: Intel Core i3-3220 CPU, 12GB RAM, 500 GB Sdd, Windows 10 Pro. This calculation is carried out in the double precision arithmetic.

- **Example 1 - Convolution quadrature method**

The example with convolution quadrature method is considered. Taking the simplest basis functions (BDF1) $\phi_j(t) = e^{-t}t^j/j!$, $j = 0, 1, 2, \ldots$. To determine the quadrature weights $\omega_j(h)$ should be calculated integral Eq. (6.29):

$$\omega_j(h) = \int_0^\infty \widehat{Q}_0 \frac{t^3(t^5 + a_1 t + a_0)}{(t^4 + \hat{\tau}_1^4)^2} e^{-t/\hat{\tau}_2} \left(\frac{t}{h}\right)^j \frac{e^{-t/h}}{j!} dt, \quad j = 0, 1, \ldots ,$$

i.e.,

$$\omega_j(h) = \frac{\widehat{Q}_0}{j! h^j} \int_0^\infty \frac{t^{j+3}(t^5 + a_1 t + a_0)}{(t^4 + \hat{\tau}_1^4)^2} e^{-(h^{-1} + \hat{\tau}_2^{-1})t} dt, \quad j = 0, 1, \ldots .$$

129

It is necessary to determine the quasi-singularities of the function $q(t)$. These are the points in which the denominator in $q(t)$ becomes zero. They are called quasi singularities, because they are complex. The quasi-singularities in the function $q(t)$ slow down the convergence of the quadrature process and must be eliminated in order to have a fast convergence of the process in numerical integration. In this case, quasi-singularities are the solutions of equation $t^4 + \hat{\tau}_1^4 = 0$:

$$
\begin{aligned}
t_1 &= -4.24264 \times 10^{-8} - 4.24264 \times 10^{-8}i, \\
t_2 &= -4.24264 \times 10^{-8} + 4.24264 \times 10^{-8}i, \\
t_3 &= 4.24264 \times 10^{-8} - 4.24264 \times 10^{-8}i, \\
t_4 &= 4.24264 \times 10^{-8} + 4.24264 \times 10^{-8}i.
\end{aligned}
\tag{6.33}
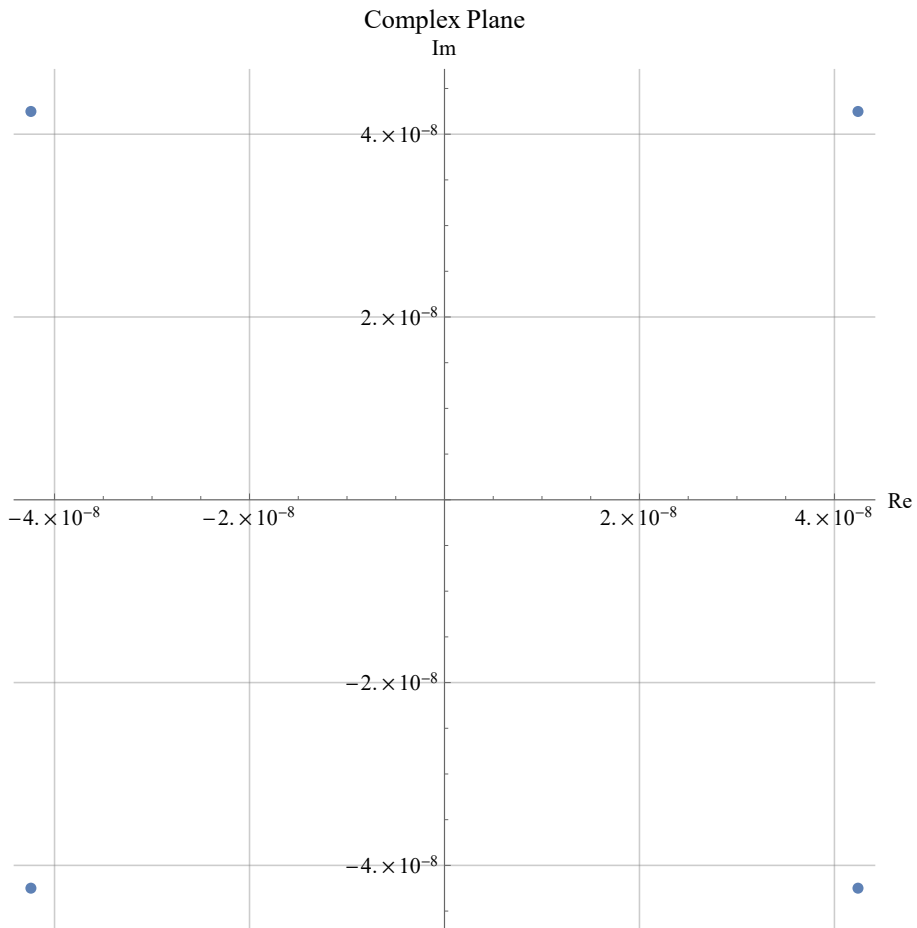$$

and are shown in the Fig. 6.3.

Figure 6.3: The quasi-singularities in the complex plane.

In other words, these are the points in the complex plane around the coordinate beginning that are on circle of radius 6×10^{-8}. These singularities are eliminated from the subintegral function using Eq. (6.30) and last integrals became:

$$\omega_j(h) = \frac{\widehat{Q}_0 \hat{\tau}_1^{j+1}}{2j!h^j} \int_0^\infty \frac{\Psi_j\left(\sqrt{\sinh \xi}\right)}{\cosh^3 \xi} \mathrm{e}^{-(h^{-1}+\hat{\tau}_2^{-1})\hat{\tau}_1\sqrt{\sinh \xi}} \mathrm{d}\xi,$$

$$\omega_j(h) = -\int_0^\infty \Phi_j(\xi; h)\mathrm{d}\xi, \quad j = 0, 1, \ldots \tag{6.34}$$

where

$$\Psi_j(z) = z^{j+2}(z^5 + b_1 z + b_0), \quad b_1 = \frac{a_1}{\hat{\tau}_1^4} = 1, \quad b_0 = \frac{a_0}{\hat{\tau}_1^5} = \frac{340}{7} = 48.57142857142857.$$

The functions $\Phi_j(\xi; h)$ is calculated for a different order j and a fixed $h = 1.5625 \times 10^{-8}$ [s] and presented in the Fig. 6.4. For calculating these integrals it can used the exponential transformation $\xi = \psi_{DE_3}$ ($\psi_{DE_3} = \exp\left(\frac{\pi}{2}\sinh x\right)$) to transform integrals over the interval $(0, \infty)$ and apply the composite trapezoidal rule on a finite interval [109]. In this calculation, the transformation rule is applied:

$$\int_0^\infty f(x)dx \approx h \sum_{k=-N}^{N} f(\psi_{DE_3}(kh))\psi'_{DE_3}(kh) \qquad (i = 1, 2, 3, 4, 5). \tag{6.35}$$
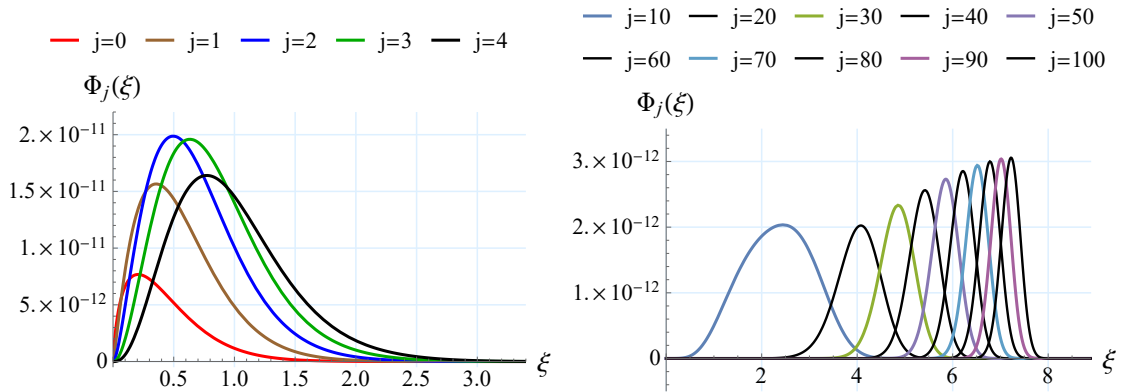

Figure 6.4: The functions $\Phi_j(\xi; h)$ for $j = 0(1)4$ (left) and $j = 10(10)100$ (right) and $h = 1.5625 \times 10^{-8}$ [s]. Adapted from [92].

In this problem, for calculating the integrals $\omega_j(h)$ in (33), it is used the command `NIntegrate` in MATHEMATICA, `Method->"DoubleExponential"` and `WorkingPrecision -> WP`.

For a given $h > 0$, it can computed the convolution weights $\omega_j(h)$, $j = 0, 1, \ldots, n$, and then it can be approximated the convolution integral in Eq. (6.34) at the points $t = t_k = kh$, $k = 0, 1, \ldots, n$, by the convolution quadrature 6.28. Result of this calculation is:

$$i_k = i(t_k) = \sum_{j=0}^{k} \omega_j(h) f_1(t_{k-j}) + R(t_k; f_1), \quad k = 0, 1, \ldots, n. \qquad (6.36)$$

Omiting $R(t_k; f_1)$ and puting $f_1(kh) \equiv \bar{f}_k$ ($k = 0, 1, \ldots, n$), the following triangular system of linear equations is obtained:

$$
\begin{aligned}
i_0 &= \omega_0(h) \bar{f}_0, \\
i_1 &= \omega_0(h) \bar{f}_1 + \omega_1(h) \bar{f}_0, \\
i_2 &= \omega_0(h) \bar{f}_2 + \omega_1(h) \bar{f}_1 + \omega_2(h) \bar{f}_0, \\
&\vdots \\
i_n &= \omega_0(h) \bar{f}_n + \omega_1(h) \bar{f}_{n-1} + \cdots + \omega_n(h) \bar{f}_0,
\end{aligned}
\qquad (6.37)
$$

from which follows the solution of system:

$$\bar{f}_0 = \frac{i_0}{\omega_0(h)}, \quad \bar{f}_k = \frac{1}{\omega_0(h)} \left(i_k - \sum_{j=1}^{k} \omega_j(h) \bar{f}_{k-j} \right), \quad k = 1, \ldots, n. \qquad (6.38)$$

Taking $n = 160$ equidistant points on $[0, T_{\max}/8]$, where $T_{\max}/8 = 2.5 \times 10^{-6}$ [s] and $h = 1.5625 \times 10^{-8}$ [s], and using equations 6.34 and approximate values of the solution $f_1(t)$ are obtained $\bar{f}_k$, $k = 0, 1, \ldots, n$, at the points $t_k = kh$, $k = 0, 1, \ldots, n$. Its interpolation function is shown in Fig. 6.5 (red line), together with the "exact" function obtained by the inverse Laplace transform (black line). Based on the Fig. 6.5, it can be noticed that the corresponding curves differ in their initial parts when t is small (before its minimum).

A few remarks about absolute error in this calculation are given. Absolute error in the approximate solution of $f_1(t)$ for BDF1 with $h_1 = 1.5 \times 10^{-8}$ [s], $h_2 = 3.9 \times 10^{-9}$ [s] and $h_3 = 10^{-9}$ [s] are given in the Fig. 6.6. Satisfactory result is obtained for $h_3 = 10^{-9}$ [s].

A better result is obtained when the BDF2 method is used. Absolute error is given in the interval $[0, T_{max}/8] = [0, 2 \times 10^{-7}]$ for two different values of h, $h_1 = 1.5 \times 10^{-8}$ [s] and $h_2 = 2 \times 10^{-9}$ [s] are given in Fig. 6.7.
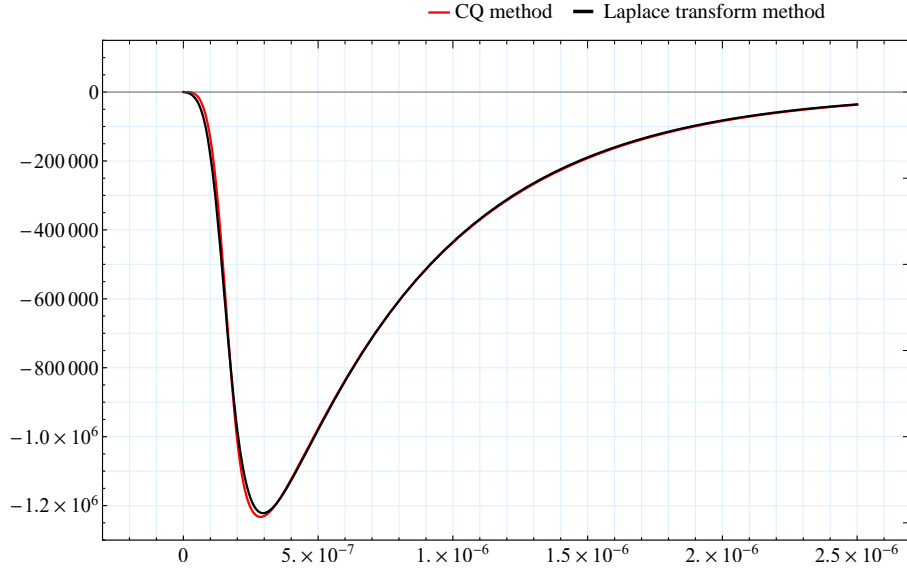
Figure 6.5: Approximate and "exact" solution of $f_1(t)$. Adapted from [92].

The deviations are greatest on the interval $[0, 3 \times 10^{-7}]$. This problem is considered on this interval. If the solution is denoted at interval obtained by the convolution quadrature formula (based on BDF1 with a step h) as $\bar{f}_h(t)$, the corresponding convolution integral denote by $i_h(t)$ is:

$$i_h(t) = \int_0^t q(t)\bar{f}_h(t - \tau)\mathrm{d}\tau. \tag{6.39}$$

The function $i_h(t)$ for three different values of h ($h_1 = 1.5625 \times 10^{-8}$ [s] (red line), $h_2 = 3.125 \times 10^{-9}$ [s] (blue line) and $h_3 = 1.875 \times 10^{-9}$ [s] (green line)), as well as $i(t)$ (black line), are presented in Fig. 6.8. It can be seen that the graphic of $i_h(t)$ for $h = h_2$ and $h = h_3$ is almost the same as one of $i(t)$. The corresponding residual function $R_h(t) = i_h(t) - i(t)$, which represent the difference between the approximate function $i_h(t)$ and given function $i(t)$, for three different values of h ($h_1 = 1.5625 \times 10^{-8}$ [s] (red line), $h_2 = 3.125 \times 10^{-9}$ [s] (blue line) and $h_3 = 1.875 \times 10^{-9}$ [s] (green line)) is shown in Fig. 6.9.

Finally, the channel discharge function is obtained as:

$$f(t) = 1 + \int_0^t f_1(\tau)\mathrm{d}\tau. \tag{6.40}$$

The graphic of this function is presented in Fig. 6.10.
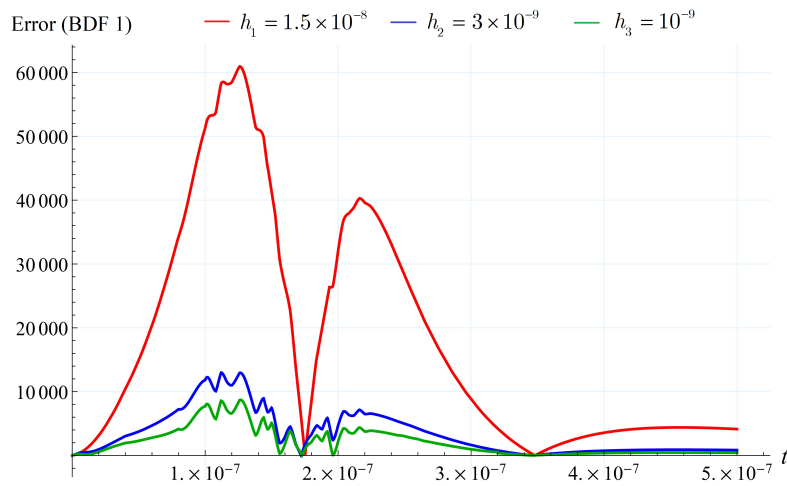
Figure 6.6: Absolute error in the solution $f_1(t)$ for BDF1. Adapted from [92].
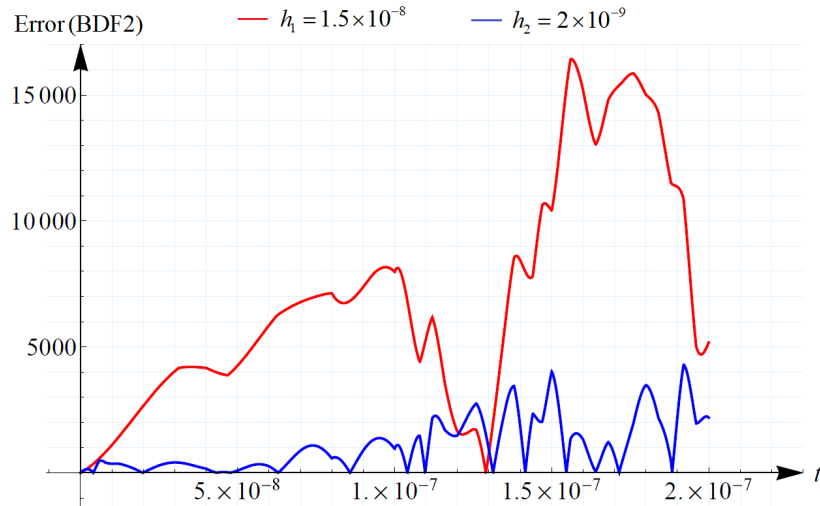
Figure 6.7: Absolute error in the solution $f_1(t)$ for BDF2. Adapted from [92].

- **Example 1 - MCTF**

In this case, this is the type of function $q'(0) = 0$. The equation is solved on two subintervals:

- subinterval $I_1 = [0, 3 \times 10^{-7}]$ with step size $h_1 = 5 \times 10^{-9}$. In this interval solution is given in the form of the Taylor series and this is the approximate component of the solution;

- subinterval $I_2 = [5 \times 10^{-8}, 2 \times 10^{-6}]$ with step size $h_2 = 3.9 \times 10^{-8}$. In this interval solution was obtained using the MCTF;
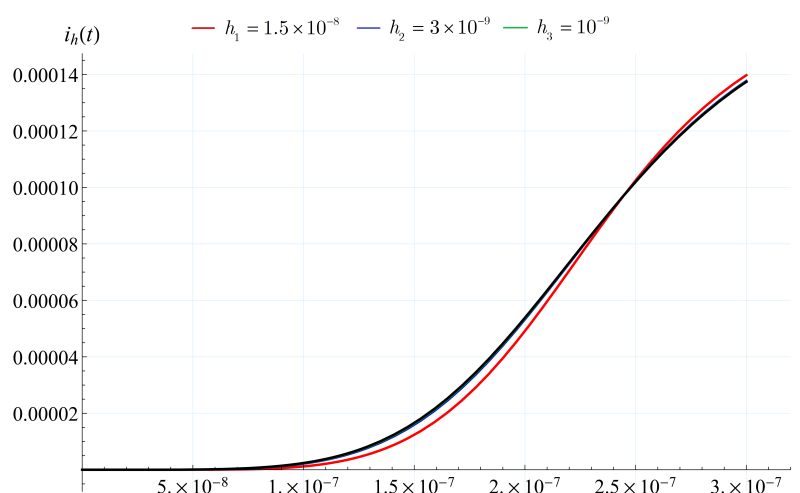
Figure 6.8: Graphics of the functions $i_h(t)$ for three different values of h and $i(t)$ (black line). Adapted from [92].
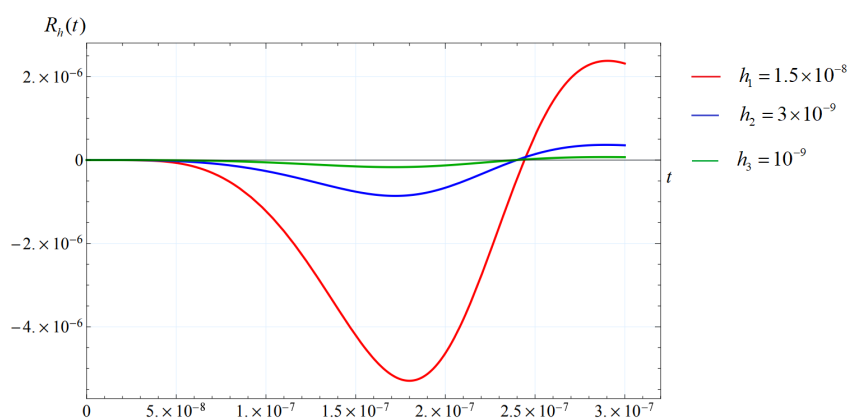
Figure 6.9: Residual function $R_h(t) = i_h(t) - i(t)$. Adapted from [92].

The solution on the whole interval is given in the Fig. 6.11.

Residual function $R_h(t) = i_h(t) - i(t)$ for this example is given in Fig. 6.12.

Other examples were solved using the MCTF method. This method is simplest for implementation and has the shortest execution time. Its disadvantage is that the function $R_h(t)$ has the biggest values.

- **Example 2**

The example with the following data is considered:

- $I_0 = 13000\,[\text{A}], \quad \tau_1 = 24 \times 10^{-8}\,[\text{s}], \quad \tau_2 = 3.4 \times 10^{-6}\,[\text{s}], \quad \eta = 0.87, \quad n = 5;$

Figure 6.10: Channel discharge function.

Figure 6.11: Solution f_1 obtained by the MCTF method for Example 1.
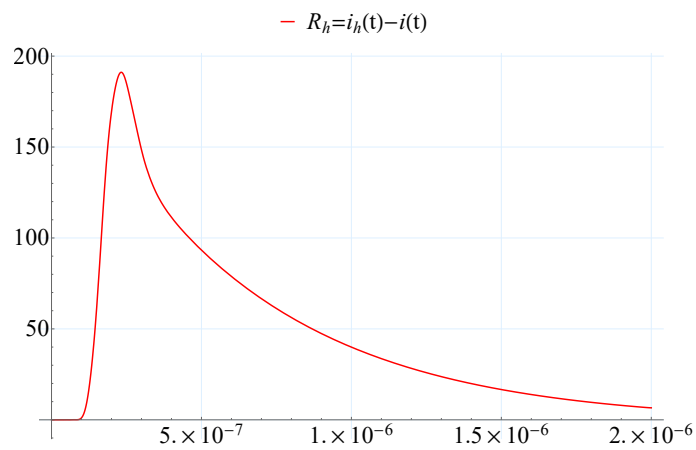
Figure 6.12: Residual function $R_h(t)$ for Example 1.

- $Q_0' = -4.39 \times 10^{-4}\,[\mathrm{C/m}], \quad \lambda_1 = 18\,[\mathrm{m}], \quad \lambda_2 = 125.5\,[\mathrm{m}], \quad \lambda_{d_1} = 45\,[\mathrm{m}],$
  $\lambda_{d_1} = 0\,[\mathrm{m}], \quad m = 4,$

as well as

$$c = 3 \times 10^8\,[\mathrm{m/s}], \quad v = \frac{c}{3} = 10^8\,[\mathrm{m/s}], \quad v^* = \frac{v\,c}{v+c} = 7.5 \times 10^7\,[\mathrm{m/s}].$$

The problem will be considered on the interval $[0, T_{\max}]$, where $T_{\max} = 20 \times 10^{-6}\,[\mathrm{s}]$.

Solution for Example 2 obtained by MCTF method is given in the Fig. 6.13. Residual function $R_h(t)$ for this example is given in Fig. 6.14.

Figure 6.13: Solution f_1 obtained by the MCTF method for Example 2.

Figure 6.14: Residual function $R_h(t)$ for Example 2.

• Example 3

The example with the following data is considered:

- $I_0 = 13000 \,[\text{A}], \quad \tau_1 = 24 \times 10^{-8} \,[\text{s}], \quad \tau_2 = 3.4 \times 10^{-6} \,[\text{s}], \quad \eta = 0.87, \quad n = 5;$

- $Q'_0 = -2.009 \times 10^{-4} \,[\text{C/m}], \quad \lambda_1 = 18 \,[\text{m}], \quad \lambda_2 = 255 \,[\text{m}], \quad \lambda_{d_1} = 45 \,[\text{m}],$
  $\lambda_{d_1} = 0 \,[\text{m}], \quad m = 3,$

as well as

$$c = 3 \times 10^8 \,[\text{m/s}], \quad v = \frac{c}{3} = 10^8 \,[\text{m/s}], \quad v^* = \frac{v\,c}{v + c} = 7.5 \times 10^7 \,[\text{m/s}].$$

The problem will be considered on the interval $[0, T_{\max}]$, where $T_{\max} = 20 \times 10^{-6} \,[\text{s}]$.

Solution for Example 3 obtained by MCTF method is given in the Fig. 6.15. Comparison between functions $i(t)$ and $i_h(t)$ for this example is given in Fig. 6.16.
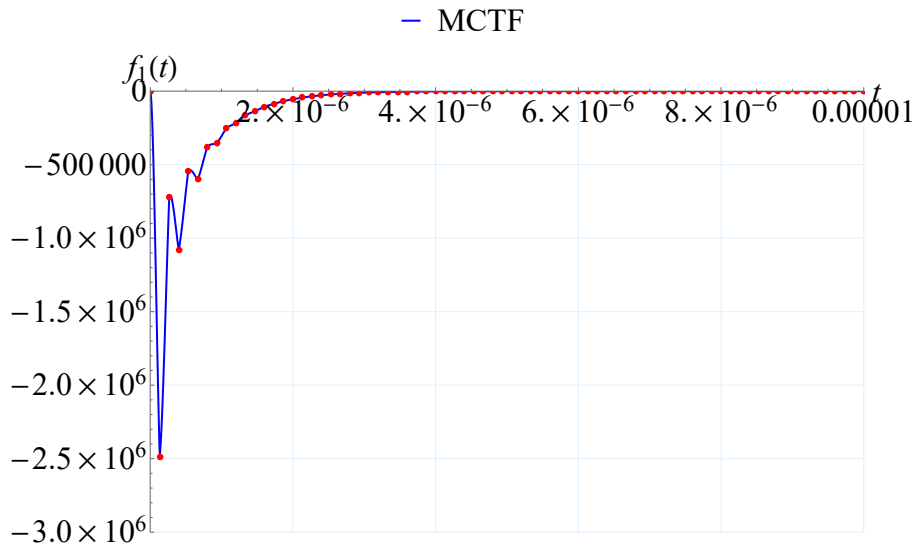
Figure 6.15: Solution f_1 obtained by the MCTF method for Example 3.
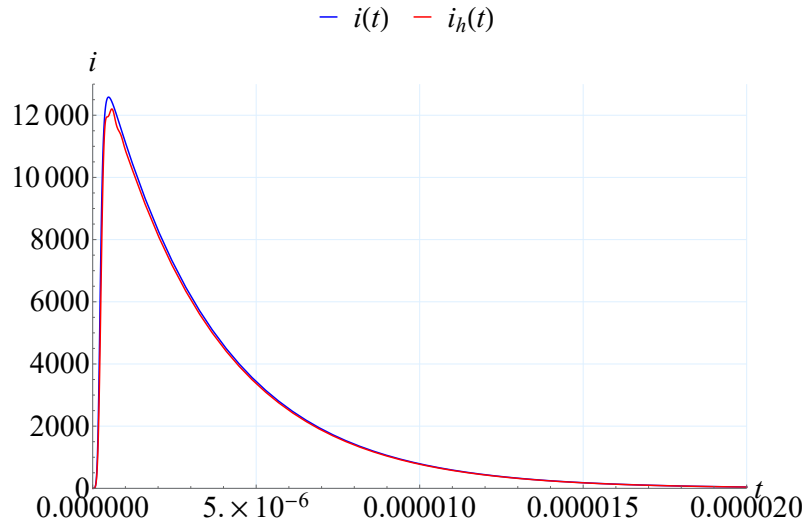
Figure 6.16: Comparison between $i(t)$ and $i_h(t)$ for Example 3.

• Example 4

The example with the following data is considered:

- $I_0 = 7000\,[\text{A}], \quad \tau_1 = 5.4 \times 10^{-6}\,[\text{s}], \quad \tau_2 = 54 \times 10^{-6}\,[\text{s}], \quad \eta = 7.9, \quad n = 5;$

- $Q'_0 = -2.72 \times 10^{-4}\,[\text{C/m}], \quad \lambda_1 = 405\,[\text{m}], \quad \lambda_2 = 2025\,[\text{m}], \quad \lambda_{d_1} = 375\,[\text{m}],$
  $\lambda_{d_2} = 0\,[\text{m}], \quad m = 2,$

as well as

$$c = 3 \times 10^8\,[\text{m/s}], \quad v = \frac{c}{3} = 10^8\,[\text{m/s}], \quad v^* = \frac{v\,c}{v + c} = 7.5 \times 10^7\,[\text{m/s}].$$

The problem will be considered on the interval $[0, T_{\max}]$, where $T_{\max} = 200 \times 10^{-6}\,[\text{s}]$.

Solution for Example 4 obtained by MCTF method is given in the Fig. 6.17. Residual function $R_h(t)$ for this example is given in Fig. 6.18.
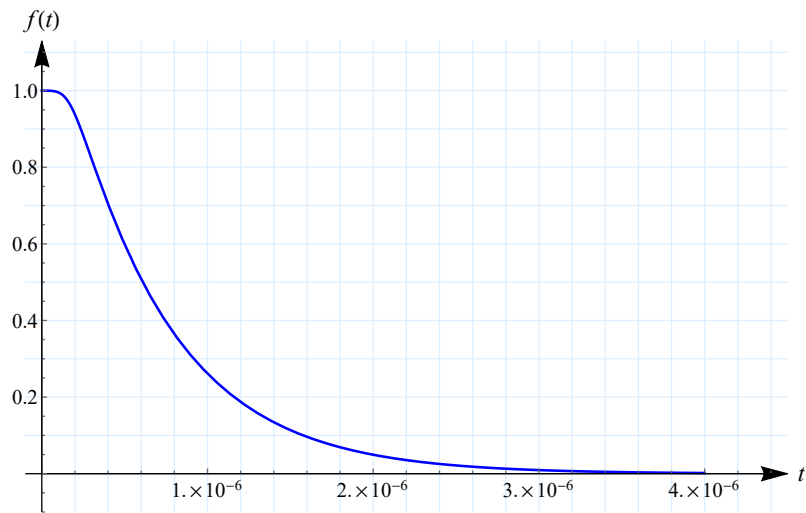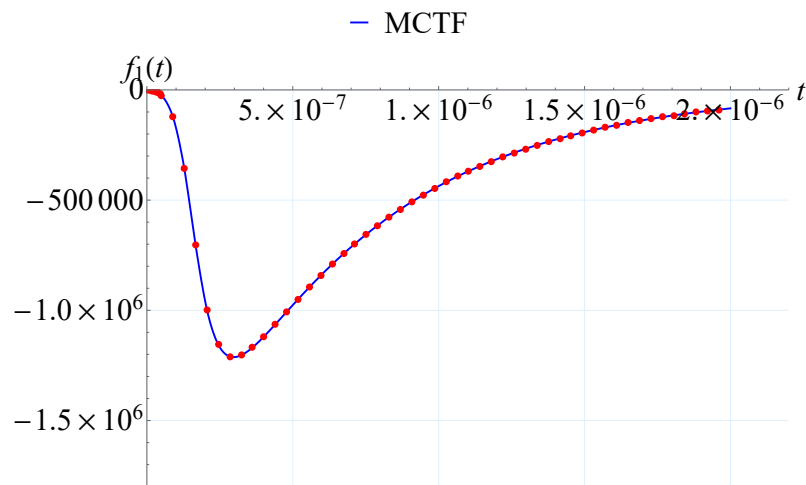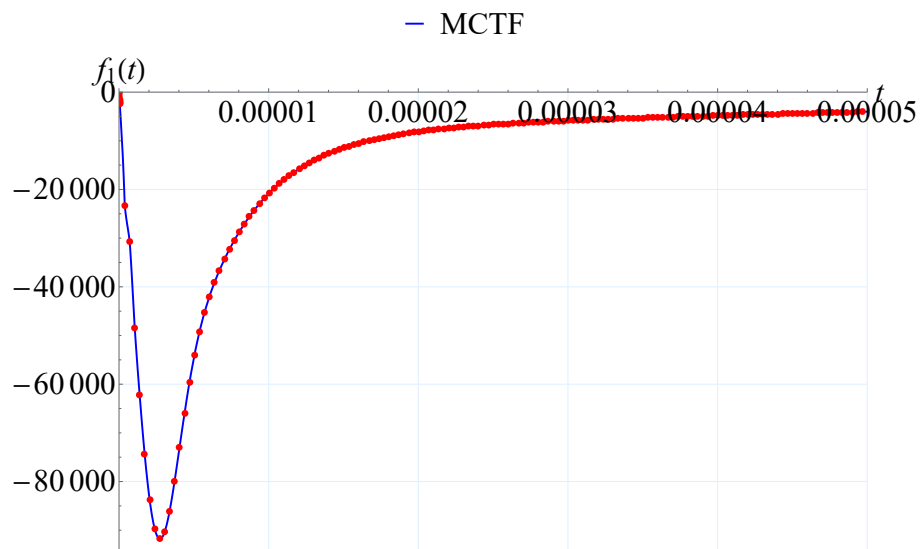
Figure 6.17: Solution f_1 obtained by the MCTF method for Example 4.
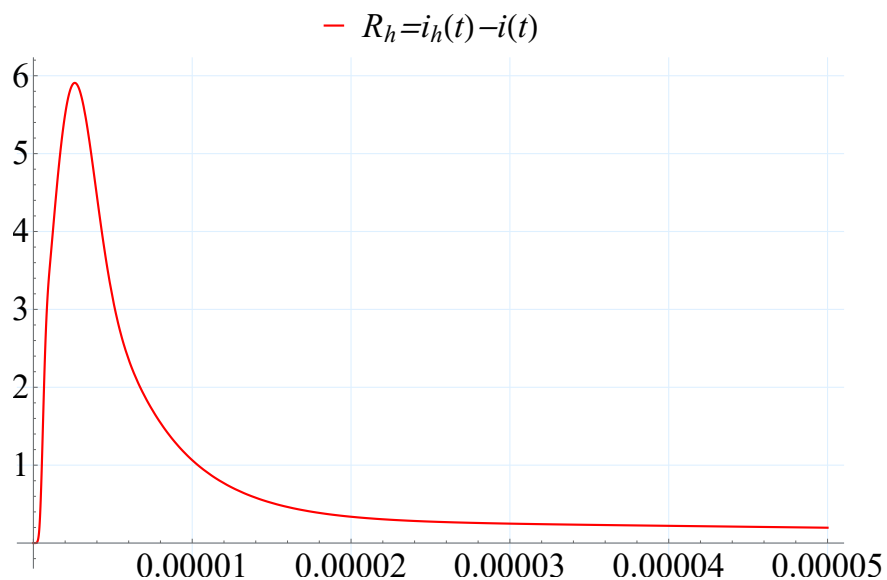
Figure 6.18: Residual function $R_h(t)$ for Example 4.

- **Example 5**

The example with the following data is considered:

- $I_0 = 7000\,[\mathrm{A}], \quad \tau_1 = 5.4 \times 10^{-6}\,[\mathrm{s}], \quad \tau_2 = 54 \times 10^{-6}\,[\mathrm{s}], \quad \eta = 7.9, \quad n = 5;$

- $Q_0' = -2.762 \times 10^{-4}\,[\mathrm{C/m}], \quad \lambda_1 = 405\,[\mathrm{m}], \quad \lambda_2 = 2000\,[\mathrm{m}], \quad \lambda_{d_1} = 750\,[\mathrm{m}], \quad \lambda_{d_2} = 0\,[\mathrm{m}], \quad m = 2,$

as well as

$$c = 3 \times 10^8 \, [\mathrm{m/s}], \quad v = \frac{c}{3} = 10^8 \, [\mathrm{m/s}], \quad v^* = \frac{v\,c}{v + c} = 7.5 \times 10^7 \, [\mathrm{m/s}].$$

The problem will be considered on the interval $[0, T_{\max}]$, where $T_{\max} = 200 \times 10^{-6} \, [\mathrm{s}]$.

Solution for Example 5 obtained by MCTF method is given in the Fig. 6.19. Residual function $R_h(t)$ for this example is given in Fig. 6.20.
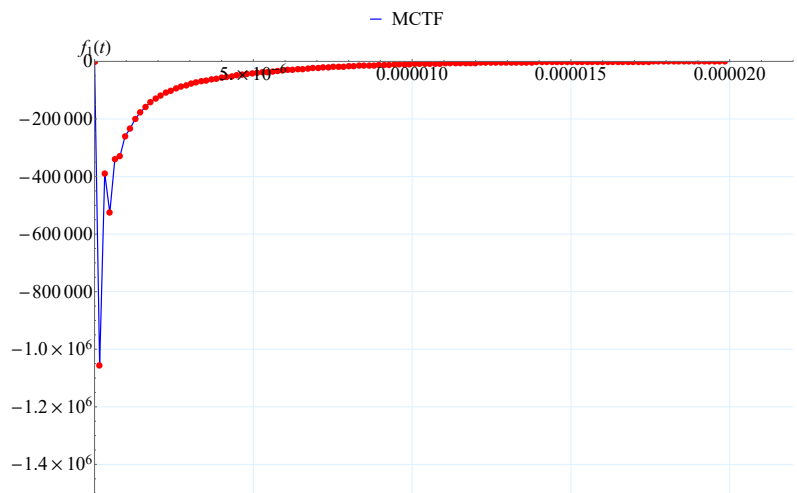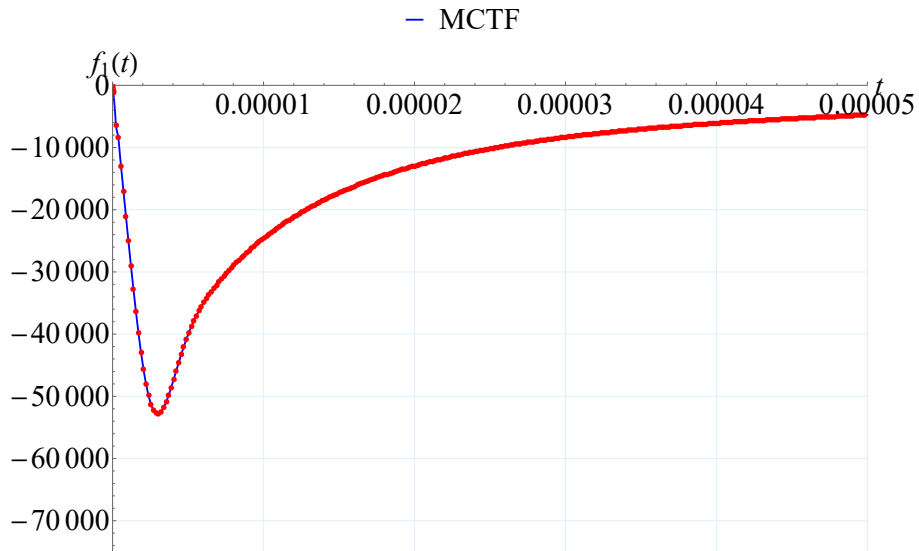

Figure 6.19: Solution f_1 obtained by the MCTF method for Example 5.
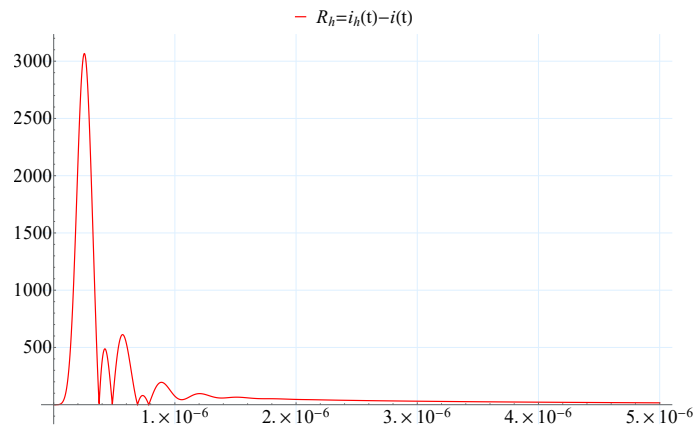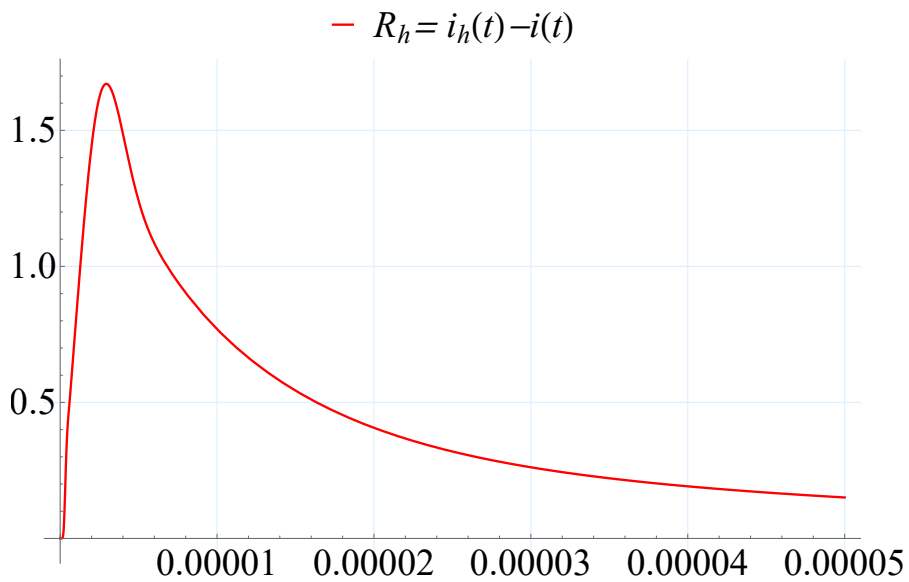

Figure 6.20: Residual function $R_h(t)$ for Example 5.

- ## Example 6

The example with the following data is considered:

- $I_0 = 7000 \, [\text{A}], \quad \tau_1 = 5.4 \times 10^{-6} \, [\text{s}], \quad \tau_2 = 54 \times 10^{-6} \, [\text{s}], \quad \eta = 7.9, \quad n = 5;$

- $Q_0' = -1.21 \times 10^{-4} \, [\text{C/m}], \quad \lambda_1 = 405 \, [\text{m}], \quad \lambda_2 = 4050 \, [\text{m}], \quad \lambda_{d_1} = 375 \, [\text{m}],$
  $\lambda_{d_2} = 0 \, [\text{m}], \quad m = 2,$

as well as

$$c = 3 \times 10^8 \, [\text{m/s}], \quad v = \frac{c}{3} = 10^8 \, [\text{m/s}], \quad v^* = \frac{v \, c}{v + c} = 7.5 \times 10^7 \, [\text{m/s}].$$

The problem will be considered on the interval $[0, T_{\max}]$, where $T_{\max} = 200 \times 10^{-6} \, [\text{s}]$.

Solution for Example 6 obtained by MCTF method is given in the Fig. 6.21. Residual function $R_h(t)$ for this example is given in Fig. 6.22.
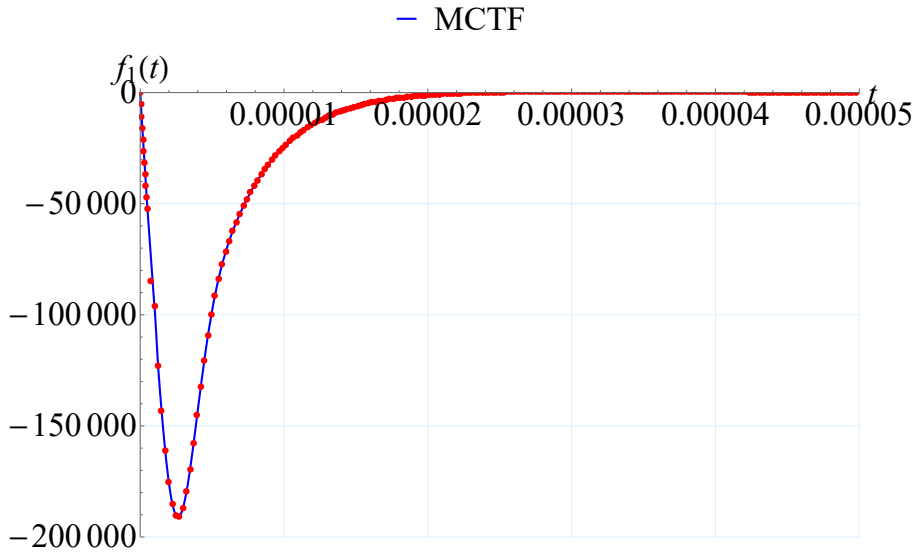
Figure 6.21: Solution f_1 obtained by the MCTF method for Example 6.

These three proposed methods can be compared according to different criteria. There will be a brief overview of each method.

Laplace transform method represent analytic solution of the problem. A disadvantage is that the inverse Laplace transform takes a long time.

Convolution quadrature method is derived for problems in integral equation and specific numerical integration [102]. The basic CQ method provides efficient numerical approximation of convolution integrals by convolution quadrature rules. In CQ method the quadrature weights are determined with the Laplace transform and a
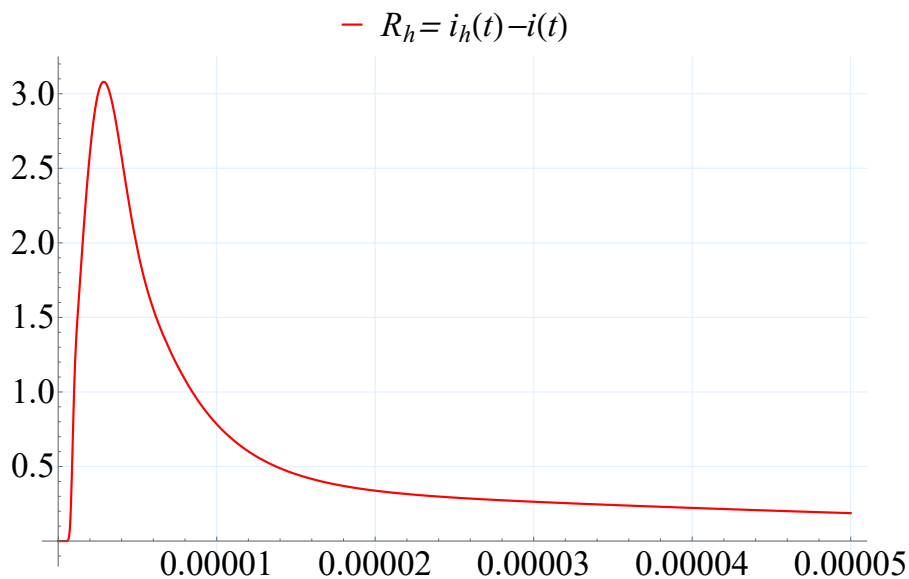
Figure 6.22: Residual function $R_h(t)$ for Example 6.

linear multistep method. This method are convergent and stable, but in work with impulse functions, there are some modification that are introduced to solve problems. Many numerical results show that CQ method is efficient for solving these problems.

It is necessary to put a note for CQ method. When solving a convolution equation whose solutions are highly-oscillating impulse functions, a statistical error may occur. This is due to the fact that when solving a system of equations (6.37), the usual successive solution of the triangular system equation (in the presence of a finite-length arithmetic) can cause problems. The quadrature weights are not determined with the same error in this case. Specifically, weights with higher index will have major errors due to error accumulation during the calculation process. Therefore, it is suitable to use the method in which errors are uniformly distributed. The error would not appear if it would be calculated exactly in the arithmetic of infinite length.

The MCTF method is a precise, efficient and relatively simple numerical method for solving Eq. (6.4). The advantage over other methods is that it has the smallest complexity of the algorithm and the shortest calculation time.

Chapter 7

Conclusion

Cloud-to-ground (CG) lightning is a large scale electric breakdown discharge with a strong current which flows through the channel and intense electromagnetic radiation. The study of the electrical characteristics of lightning is very important topic in the field of lightning physics as well as in the field of lightning protection. Internal electric field and resistance in lightning channel are two important parameters which represent the electrical performances of lightning. In this dissertation, the necessary parameters were calculated based on the engineering return stroke models. The matching of calculated physical quantities with experimental results is satisfactory.

In addition, the lightning channel that is highly ionized stable structure (suddenly created plasma) that lasts much longer than is expected from theoretical considerations and laboratory simulations. Namely, the absence of a pinch effect in plasma structures with a pronounced long geometry and strong current is extremely unusual. In presented dissertation, the first step of the research has been carried out, with aim to partially try to explain the stability of the lightning channel in the return stroke. During this research, fast and very precise analytical and numerical methods for calculating the channel discharge function were developed. These functions will be used for detailed study of lightning channel dynamics and stability of lightning channel.

The conducted analysis confirms all known results and theoretical assumptions and also allows obtaining new results. The basic contributions of this dissertation are the following results:

- A clear classification of engineering return stroke models is shown. Also, an overview of models modeling the dynamics of the corona sheath is given;

- A precisely calculated axial electric field along the axis of the lightning channel. Calculated electric field is without discontinuity, as well as the current in the

core with the direction from ground to cloud (for negative return strokes). Maximum electric field at every point in space was lower than the breakdown electric field at the surface of the corona envelope. Also, the mean value of the calculated field is in accordance with the experiment.

- Maximum value of longitudinal scalar conductivity is of the order of several tens of kS/m, and that is the result estimated theoretically and from spectroscopic measurement of plasma temperature in the channel.

- There are proposed and analyzed a precise, efficient and relatively simple methods for calculation of the channel discharge function. The standard Laplace transformation method is applied, the convolution quadrature method based on the BDF-functions (including the transformation for eliminating singularities) and MCTF method. The second method is sufficiently precise and it is much faster than the Laplace transform method. Also, it does not use special functions like the Meijer G-function. The advantages of MCTF method with respect to other methods is that it has the smallest complexity of the algorithm, the least calculation time, and, on the other hand, the disadvantage is that it is less accurate than the other two methods. After all performed analysis, the best one was the MCTF method.

The aim of the research in this dissertation is the development and application of numerical and analytical methods whose application can be effectively examined in the internal structure of the lightning channel (including electrostatic, but also other physical effects). The significance of the research is reflected in the possibility of developing advanced, detailed and effective methods to achieve understanding of individual physical effects as well as their combinations.

In this way, by calculating the channel discharge function, it will be possible to improve further calculation processes and overcome current limitations in understanding the physical processes and parameter distribution along radial and axial directions of lightning plasma channel. This is also supported by the emergence of new experimental results that have been recently published [111].

Appendices

Appendix A

Meijer G-function

Meijer G-function is introduced by Cornelis Mayer in 1936. It is a very general function introduced to include most of the familiar special functions as a partial case. The general definition of Meijer G-function is given by the following curvilinear integral in the complex plane:

$$
G_{p,q}^{m,n}\left(z \left| \begin{array}{c} a_1,\ldots,a_p \\ b_1,\ldots,b_q \end{array}\right.\right) \equiv G_{p,q}^{m,n}\left(z \left| \begin{array}{c} a_1,\ldots,a_n;a_{n+1},\ldots,a_p \\ b_1,\ldots,b_m;b_{m+1},\ldots,b_q \end{array}\right.\right) \tag{A.1}
$$

$$
= \frac{1}{2\pi i}\int_L \frac{\prod\limits_{\nu=1}^{m}\Gamma(b_\nu-s)\prod\limits_{\nu=1}^{n}\Gamma(1-a_\nu+s)}{\prod\limits_{\nu=m+1}^{q}\Gamma(1-b_\nu+s)\prod\limits_{\nu=n+1}^{p}\Gamma(a_\nu-s)} z^s\,\mathrm{d}s,
$$

where Γ is gamma function. Integral (A.1) is an Mellin-Barnes integral and alternative (equivalent) definition of the Meijer G-function can be done in terms of the inverse Mellin transform. An empty product is interpreted as 1, and parameters a_ν and b_ν are such that no pole of $\Gamma(b_\nu-s)$, $\nu=1,\ldots,m$, coincides with any pole of $\Gamma(1-b_\mu+s)$, $\mu=1,\ldots,n$.

As it can be seen, m and n are such that $1 \le m \le q$ and $1 \le n \le p$. Roughly speaking, the contour L separates the poles of functions $\Gamma(b_1-s)$, ..., $\Gamma(b_m-s)$ from the poles of $\Gamma(1-a_1+s)$, ..., $\Gamma(1-a_n+s)$. One of the fascinating properties of the family of Meijer G- functions is its closure property under differentiation as well as indefinite integration [112]. In the Wolfram Mathematica, the Meijer G-function is implemented as [113]:

```
MeijerG[{{a1,...,an},{an1,,...,ap}},{{b1,...,bm},{bm1,...,bq}},z]
```

and is suitable for both, symbolic and numerical manipulation, and its value can be

evaluated with an arbitrary precision. Elementary functions and special functions can be represented in terms of Meijer G-functions.

$$e^z = G_{1,0}^{0,1} \left(-z \,\middle|\, \begin{matrix} - \\ 0 \end{matrix} \right), \tag{A.2}$$

$$\ln(1 + z) = G_{1,2}^{2,2} \left(z \,\middle|\, \begin{matrix} 1, 1 \\ 1, 0 \end{matrix} \right), \tag{A.3}$$

$$\cos z = \sqrt{\pi} \, G_{1,0}^{0,2} \left(\frac{z^2}{4} \,\middle|\, \begin{matrix} - \\ 0, 1/2 \end{matrix} \right), \tag{A.4}$$

$$\Gamma(\alpha, z) = G_{1,2}^{2,0} \left(z \,\middle|\, \begin{matrix} 1 \\ \alpha, 0 \end{matrix} \right), \tag{A.5}$$

$$J_\nu = G_{0,2}^{1,0} \left(\frac{z^2}{4} \,\middle|\, \begin{matrix} - \\ \nu/2, -\nu/2 \end{matrix} \right), \quad -\frac{\pi}{2} < \arg(z) < \frac{\pi}{2}, \tag{A.6}$$

$$K(z) = \frac{1}{2} G_{2,2}^{1,2} \left(-z \,\middle|\, \begin{matrix} 1/2, 1/2 \\ 0, 0 \end{matrix} \right). \tag{A.7}$$

Appendix B

Laplace transform for functions $i(t)$ and $q(z)$

Laplace transform for function $i(t)$ is given the following expression:

$$
\begin{aligned}
I(s) = \mathcal{L}[i(t)](s) &= \frac{I_0}{\eta v^*} \int_0^\infty e^{-st} \frac{(t/\tau_1)^n}{1 + (t/\tau_1)^n} e^{-t/\tau_2} dt \\
&= \frac{I_0 \tau_1}{\eta v^*} \int_0^\infty e^{-(\tau_1 s + \tau_1/\tau_2)x} \frac{x^n}{1 + x^n} dx \\
&= A\tau_1 G_n \left(\tau_1 \left(s + \tau_2^{-1} \right) \right),
\end{aligned}
\tag{B.1}
$$

where G_n is given by Eq. (6.21) and the constant A is given by $A = I_0/(\eta v^*)$.

In order to find the Laplace transform of $q(t)$, $Q(s) = \mathcal{L}[q(t)](s)$, first determined $G(s) = \mathcal{L}[\hat{g}(t)](s)$, where $\hat{g}(t) = g(v^* t)$ and g is defined by Eq. (3.32).

Now, the new time constants are introduced, $\hat{\tau}_1$ and $\hat{\tau}_2$ by:

$$
\lambda_1 = v^* \hat{\tau}_1 \quad \text{and} \quad \lambda_2 = v^* \hat{\tau}_2.
\tag{B.2}
$$

If a shift $t = \hat{\tau}_1 x$ is introduced, the term is given:

$$
\begin{aligned}
G(s) &= \int_0^\infty e^{-st} \frac{(v^* t)^m}{\lambda_1^m + (v^* t)^m} e^{-v^* t/\lambda_2} dt \\
&= \int_0^\infty e^{-st} \frac{(t/\hat{\tau}_1)^m}{1 + (t/\hat{\tau}_1)^m} e^{-t/\hat{\tau}_2} dt \\
&= \hat{\tau}_1 \int_0^\infty e^{-\hat{\tau}_1(s + 1/\hat{\tau}_2)x} \frac{x^m}{1 + x^m} dx,
\end{aligned}
$$

i.e.,

$$G(s) = \mathcal{L}[\hat{g}(t)](s) = \hat{\tau}_1 G_m \left(\hat{\tau}_1 \left(s + \hat{\tau}_2^{-1} \right) \right), \tag{B.3}$$

where G_m is given by Eq. (6.21).

According to Eq. (3.33) with $g(v^*t) = \hat{g}(t)$, it follows:

$$q(t) = Q_0' \left\{ \hat{g}(t) + \frac{\lambda_{d_1}}{v^*} \hat{g}'(t) + \frac{\lambda_{d_2}}{v^{*2}} \hat{g}''(t) \right\}.$$

Since $m \geq 1$ and

$$\hat{g}(t) = \frac{(v^*t)^m}{\lambda_1^m + (v^*t)^m} e^{-v^*t/\lambda_2} = \frac{t^m}{\hat{\tau}_1^m + t^m} e^{-t/\hat{\tau}_2} \quad \text{and} \quad \hat{g}'(t) = -\frac{1}{\hat{\tau}_2} \hat{g}(t) + \frac{m \hat{\tau}_1^m t^{m-1}}{(\hat{\tau}_1^m + t^m)^2} e^{-t/\hat{\tau}_2}, \tag{B.4}$$

it can be concluded that $\hat{g}(0) = 0$ and $\hat{g}'(0) = 0$ for $m \geq 2$ and $\hat{g}'(0) = 1/\hat{\tau}_1$ when $m = 1$. Therefore, Laplace transform of the function $q(t)$ is:

$$Q(s) = \mathcal{L}[q(t)](s) = Q_0' \left\{ G(s) + \frac{\lambda_{d_1}}{v^*} \left(sG(s) - \hat{g}(0) \right) + \frac{\lambda_{d_2}}{v^{*2}} \left(s^2 G(s) - s\hat{g}(0) - \hat{g}'(0) \right) \right\},$$

i.e.,

$$
\begin{aligned}
Q(s) &= Q_0' \left\{ \left(1 + \frac{\lambda_{d_1}}{v^*} s + \frac{\lambda_{d_2}}{v^{*2}} s^2 \right) G(s) - \frac{\lambda_{d_2}}{v^{*2} \hat{\tau}_1} \delta_{m,1} \right\} \\
&= Q_0' \left\{ \left(1 + \frac{\lambda_{d_1}}{v^*} s + \frac{\lambda_{d_2}}{v^{*2}} s^2 \right) \hat{\tau}_1 G_m \left(\hat{\tau}_1 \left(s + \hat{\tau}_2^{-1} \right) \right) - \frac{\lambda_{d_2}}{v^{*2} \hat{\tau}_1} \delta_{m,1} \right\}, \tag{B.5}
\end{aligned}
$$

because of (B.3). Here, $\delta_{m,1}$ is Kronecker's delta.

Appendix C

Backward differentiation formula - BDF

The backward differentiation formula (BDF) is a family of implicit methods for the "numerical integration of ordinary differential equations". They are linear multistep methods that, given a function and a temporal instant, provide an approximate value of the derivative of the function using the results of the calculations for previous time instants and thus increasing the accuracy of the approximation. These methods are especially used for the solution of stiff differential equations [114].

BDF's are used to solve the following problem with the initial values:

$$y^{'} = f(y,t), \quad y(t_0) = y_0 \tag{C.1}$$

A generic BDF can be written as:

$$\sum_{k=0}^{s} a_k y_{n+k} = h\beta f(t_{n+s}, y_{n+s}), \tag{C.2}$$

where h denotes the step size and $t_n = t_0 + nh$. The coefficients a_k and β are chosen in such way that the method reaches the order s, which is as maximum as possible. The BDF methods are all implicit because the unknown value y_{n+1} enters into the equation. BDF (s) has exactly the consistency order s.

The s-step BDF's with $s < 7$ are:

- BDF1 - implicit Euler method:
  $y_{n+1} - y_n = hf(x_{n+1}, y_{n+1})$

- BDF2:
  $3y_{n+2} - 4y_{n+1} + y_n = 2hf(x_{n+2}, y_{n+2})$

- BDF3:

$$11y_{n+3} - 18y_{n+2} + 9y_{n+1} - 2y_n = 6hf(x_{n+3}, y_{n+3})$$

- BDF4:

$$25y_{n+4} - 48y_{n+3} + 36y_{n+2} - 16y_{n+1} + 3y_n = 12hf(x_{n+4}, y_{n+4})$$

- BDF5:

$$137y_{n+5} - 300y_{n+4} + 300y_{n+3} - 200y_{n+2} + 75y_{n+1} - 12y_n = 60hf(x_{n+5}, y_{n+5})$$

- BDF6:

$$147y_{n+6} - 360y_{n+5} + 450y_{n+4} - 400y_{n+3} + 225y_{n+2} - 72y_{n+1} + 10y_n = 60hf(x_{n+6}, y_{n+6})$$

The stability of the numerical solution that calculates the solution of a stiff differential equation is shown as an area that can guarantee absolute stability (or linear stability) on a complex number plane. The absolute stability region of the BDF method (region of absolute stability) is the pink area on the Fig C.1.

The method BDF1 is the implicit Euler method. This method and BDF2 method are A stable, while the higher order methods A (α) - stable, with the opening angle α downsized with higher order. For $s > 6$, the methods are unstable.
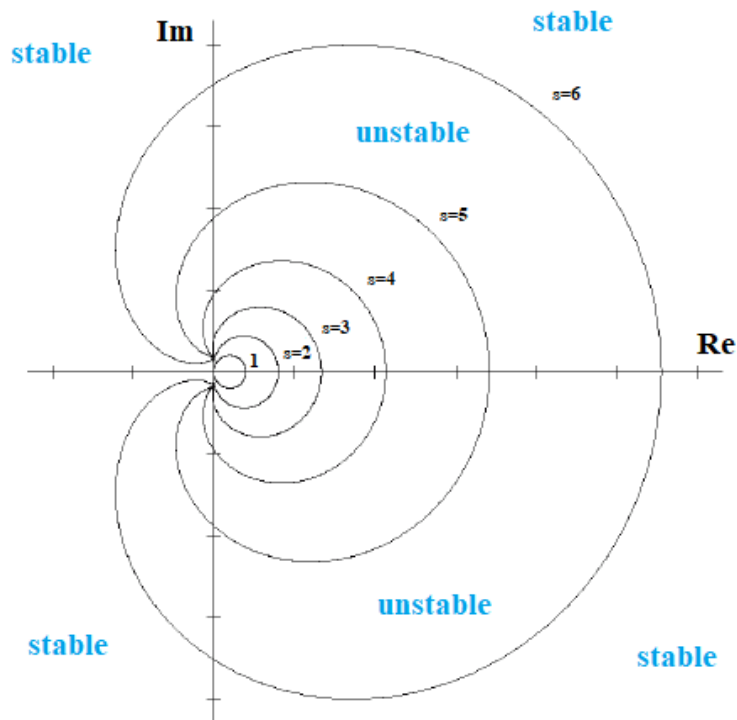
Figure C.1: BDF.

Bibliography

[1] T. Klinger, Overview of first high-performance operation of Wendelstein 7-X with operation of Wendelstein 7-X with island divertor, 27th IAEA Fusion Energy Conference (FEC 2018), Gandhinagar (India), 22 – 27 October 2018.

[2] R. L. Gardner, Ph.D. thesis, University of Colorado, 1980.

[3] R. Gardner, Lightning Electromagnetics, CRC Press, 01.05.1990.

[4] V. Cooray, The Lightning Flash, The Institution of Engineering and Technology, 2003 (ISBN-13: 978-0852967805).

[5] MIT OCW, Introduction to Plasma Physics I (Fall 2006), 22.611J, Instructor(s): Prof. Ian Hutchinson and Prof. Jeffrey Freidberg.

[6] https://www.wikipedia.org

[7] D. K. Kalluri, Electromagnetics of Complex Media, CRC Press, Boca Raton, 1999.

[8] A. I. Morozov, Introduction to Plasma Dynamic, 2012.

[9] J. R. Perić, Savremeni pravci istraživanja u Hemiji plazme, Fakultet za fizičku hemiju, doktorske studije, 2018.

[10] J. A. Bittencourt, Fundamentals of Plasma Physics, Springer Science and Business Media, 17.06.2004

[11] F. F. Chen, Introduction to plasma physics, Plenum Press, New York, 1974.

[12] M. Alimpijević, Uticaj ekvivalentne temperature Maksvelovog spektra gasa slobodnih elektrona na proboj gasova pri malim vrednostima pritisaka i međuelektrodnog rastojanja, doktorska disertacija, Beograd, 2015.

[13] J. Raimbault, Introduction 'a la Physique des Plasmas, Laboratoire de Physique des Plasmas, Universit´e Paris-Sud 11, Master 2 APIM et PIE, 2012.

[14] Ю. П. Райзер. Физика газового разряда. Изд. 2-ое, доп. и перераб. М.: Наука, 1992 год, 536 стр.

[15] M. Hotinceanu, Z. Borsos, O. Dinu, Aspects of Thermodynamic Equilibrium in Plasma, Matematică - Informatică - Fizică, Vol. LXII, No. 1/2010.

[16] P. Osmokrović, Elektrotehnički materijali, Akademska misao Beograd, 2003.

[17] A. Küchler, Hochspannungstechnik: Grundlagen - Technologie - Anwendungen, Springer Vieweg; 4. Aufl. 2017 edition.

[18] H. Reather, Electron Avalanches and Breakdown in Gases, London: Butterworth and Co. Ltd., 1964.

[19] J. Meek (1940). "A Theory of Spark Discharge". Physical Review. 57 (8): 722–728.

[20] M. C. Wang and E. E. Kunhardt, Streamer dynamics Phys. Rev. A 42., 1990.

[21] C. T. Phelps, Positive streamer system intensification and its possible role in lightning initiation, J. Atmos. Terr. Phys., 36, 103-111, 1974.

[22] A. Fridman, L. A. Kennedy, Plasma Physics and Engineering, CRC Press, Second Edition, 2012.

[23] A. Haddad, Advances in High Voltage Engineering, ISBN-10: 1849190380, October 22, 2004.

[24] M. M. Simić, Lučna plazma u zagrejanom grafitnom cilindru, kao spektroskopski izvor, doktorska disertacija, Beograd, 1977.

[25] В. Ф. Важов, Ю.И. Кузнецов, Г.Е. Куртенков, В.А. Лавринович, В.В. Лопатин, А.В. Мытников, Техника высоких напряжений, Томский политехнический университет, Томск, 2010. – 208 с.

[26] С. Самарџић, Линијски спектар неутралног аргона емитован из лучне плазме (Дипломски рад), Нови Сад, 1999.

[27] M. Schnick, U. Fuessel, M. Hertel, A. Spille-Kohoff and A. B. Murphy, Numerical investigations of arc behaviour in gas metal arc welding using ANSYS CFX, Front. Mater. Sci. 2011, 5(2): 98–108, DOI 10.1007/s11706-011-0134-4.

[28] C. E. Baum, Return stroke initiation, In Lightning Electromagnetics, ed. R.L.Gardner, New York: Hemisphere, pp. 101-14, (1990).

[29] V. Cooray, V. A. Rakov, N. Theethayi, The lightning striking distance-Revisited, J. Electrostatics 65, 296-306, (2007).

[30] B. F. J. Schonland: Progressive Lightning, pt. 4, The Discharge Mechanism, Proc. Roy. Soc. (London), A 164:132-150, 1938.

[31] C. F. Wagner and A. R. Hileman: The lightning stroke (1). AIEE Trans. 77(3): 622-42, 1958.

[32] E. T. Pierce and T. W. Wormell: Field changes due to lightning discharges. In Thunderstrom Electricity. Ed. H.R.Byers. pp. 251-66. Chicago, Illinois. University of Chicago Press.

[33] D. J. Malan: Physic of Ligtning. 176 pp. London: The English Universities Press. 1963.

[34] M. A. Uman: The diameter of lightning. J. Geophys. Res. 69: 583-5. 1964.

[35] M. A. Uman, D. K. McLain, Magnetic field of lightning return stroke, J.Geophys.Res. 74, 6899-6910, (1969).

[36] R. E. Orville, M. A. Uman and A. M. Sletten: Temperature and electron density in long air sparks. J. Appl. Phys. 38: 895-6. 1967.

[37] J. B. Higham and J. M. Meek: The expansion of gaseous spark chanenels. Proc.Phys. Soc. (London) B 63694-61. 1950a.

[38] H. Norinder and O. Karsten: Experimental Investigation of Resistance and Power within Artifical Lightning Current Pats. Arkiv. Mat. 36: 1-48. 1948.

[39] S. I. Drabkina: The theory of the development of a spark channel. J.Exper. Teoret. Phys. 21: 473-83. (English translation, AERE LIB/Trans 621, Harwell, Berkshire, UK.) 34: 1068-74, 1951.

[40] J. M. Somerville: The Electric Arc. Pp 101-19, John Wiley and Sons,Inc,New York, 1959.

[41] S. I. Braginskii, "Theory of the development of a spark channel", Sov.Phys.JETP, vol. 34,pp. 1068-1074, 1958 (Engl. transl.).

[42] R.D.Hill: Channel heating in return stroke lightning. J. Geophys. Res. 76:637-45, 1971.

[43] E.I.Dubovoy, V.I.Pryazhinsky and G.I.Chitanava: Calculation of energy dissipation in lightning channel. Meteorologiya i gidralogiya 2: 40-5. 1991.

[44] M. Plooster, Numerical model of the return stroke of the lightning discharge, Phys. Fluids, 14(10), 2124, (1971a).

[45] M. Plooster, Numerical simulation of spark discharges in air, Phys. Fluids, 14(10), 2111, (1971b).

[46] A. H. Paxton, L. R. Gardner and L. Baker: Lightning return stroke: numerical calculation of the optical radiation. Phys. Fluids 29: 2736-41, 1986.

[47] A. H. Paxton, L. R. Gardner and L. Baker: Lightning return stroke: numerical calculation of the optical radiation, In Lightning Electromagnetics, ed. R.L.Gardner, pp. 47-61, New York: Hemisphere. 1990.

[48] Modest, M. F. (2002), Radiative Heat Transfer, 2nd ed., Acad. Press, New York.

[49] V. A. Rakov, A. A. Dulzon, Calculated electromagnetic fields of lightning return stroke, Tekh.Elektrodinam. (1987) 87-89 (in Russain).

[50] C. A. Nucci, C. Mazzetti, F. Rachidi, M. Ianoz, On lightning return stroke modelsfor LEMP calculations, in: 19th International Conference on Lightning protection, Graz, Austria, 1988.

[51] V. A. Rakov, A. A. Dulzon, A modified transmission line model for lightning return stroke field calculation, in: 9th International Zurich Symposium and TechnicalExhibition on EMC, Zurich, Switzerland, 1991.

[52] C. E. R. Bruce, R. H. Golde, The lightning discharge,J.Inst.Electr.Eng. 88 (6), 487-505, (1941).

[53] M. A. Uman and D. K. McLain, Magnetic Field of Lightning Return Stroke. Journal of Geophysical Research, 74, 6899-6910, (1969).

[54] B. F. J. Schonland, The lightning discharge, Handbuch der Physik 22, 576-628, 1956.

[55] F. Heidler, TCS model for LEMP calculation, in: 6th Symposium on EMC, Zurich, pp.175-162, 1985.

[56] G. Diendorfer, M. A. Uman, An improved return stroke model with specified channel-base current, J.Geophys. Res. 95, 13621-13644, (1990).

[57] R. Thottappillil, M. A. Uman, Lightning return stroke model with height-variable discharge time constant, J.Geophys. Res. 99, 22773-22780, (1994).

[58] J. M. Cvetic, B. V. Stanic, An improved return stroke model with specified channel-base current and charge distribution along lightning channel, in: International Conference on Electromagnetics in Advanced Application (ICEAA), Torino, Italy, 1995.

[59] J. M. Cvetic, B. V. Stanic, F. Heidler, Behavior of the rise and fall characteristics of the channel discharge function for the GTCS return stroke model, in: 15th International Zurich Symposium and Technical Exhibition on EMC, Zurich, pp. 557-560, 2003.

[60] J. M. Cvetić: Interakcija elektromagnetskog impulsa struje munje sa žičanim vodovima iznad zemlje, magistarska teza, Elektrotehnički fakultet Univerziteta u Beogradu, Srbija, 1993.

[61] Y. T. Lin, M. A. Uman, R. B. Standler "Lightning Return Stroke Models", Journal of Geophysical Research, Vol.85, No. C3, March, 1980.

[62] M. J. Master, M. A. Uman, Y.T.Lin and R.B.Standler, "Calculation of Lightning Return Stroke Electric and Magnetic Fields above Ground", Journal of Geophysical Research, Vol.86, No.C12, Pec.1981.

[63] E. T. Pierce, Meteorogical aspects of the source of atmospherics noise in lightning, paper in Radio Noise of Terrestial Origin, ed F.Horner, Elsevier, 55-71, (1962).

[64] A. S. Dennis and E. T. Pierce, "The Return Stroke of the Lightning Flash to Earth as a Source of VLF Atomspheric," Radio Sci., J. Res. Vol 68D, pp 777-794, (1964).

[65] J. M.Cvetić: Model povratnog udara atmosferskog pražnjenja sa specificiranom strujom u tački udara i raspodelom naelektrisanja duž kanala, doktorska disertacija, Elektrotehnički fakultet Univerziteta u Beogradu, Srbija, 1996.

[66] C. E. Baum, L. Baker, Analytic transmission line model, in: R.L.Gardner (Ed.), Lightning Electromagnetics, Hemisphere Publishing Corporation, New York, pp. 17-40, 1990.

[67] V. Kodali, V. A. Rakov, M. A. Uman, K. J. Rambo, G. H. Schnetzer, J. Schoene, J. Jer-auld, Triggered lightning properties inferred from measured currents and veryclose electric fields, Atmos. Res. 75, 335-376, (2005).

[68] M. A. Uman, The Lightning Discharge. New York: Academic, 1987.

[69] V. A. Rakov, M. A. Uman, Lightning, Physics and Effects, Cambridge University Press, Cambridge, 2003.

[70] M. Tausanovic, M. Ignjatovic, J. Cvetic, F.Heidler, M.Alimpijevic, D.Pavlovic, Influence of current reflections from the ground on the corona sheath dynamics during the return stroke, Electric Power System Research, Elsevier, 2017.

[71] F. Heidler, Review and extension of the TCS-model to consider the current reflections at ground and at the upper end of the lightning channel, J. Light.Res. 1, 40-50, (2007).

[72] F. Heidler, J. M. Cvetic, and B. V. Stanic, "Calculation of lightning current parameters", IEEE Trans. Power Del., vol. 14, no. 2, pp. 399–404, Apr. 1999.

[73] D. Pavlovic, J. Cvetic, F. Heidler, R. Djuric, Vertical electric field inside the lightning channel and the channel-core conductivity during discharge - Comparison of different return stroke models, ELECTRIC POWER SYSTEMS RESEARCH, vol. 113 br., str. 30-40, (2014).

[74] B. F. J. Schonland, The diameter of lightning channel, Philos.Mag.37 503-508, (1937).

[75] B. F. J. Schonland, The Flight of Thunderbolts, Oxford University Press, New York, 63 pp, 1950.

[76] R. Jones, Return stroke core diameter, J.Geophys. Res. 73, 809-814, (1968).

[77] G. Maslowski, V. A. Rakov, A study of the lightning channel corona sheath, J.Geophys. Res. 111 (D14110) (2006), http://dx.doi.org/10.1029/2005JD006858.

[78] M. Tausanovic, S. Markovic, S. Marjanovic, J. Cvetic, M. Cvejic, Dynamics of alightning channel corona sheath using a generalized traveling current source return stroke model – theory and calculations, IEEE Trans. EMC 52 (3), 646–656, (2010).

[79] J. R. Dwyer, M. A. Uman, The physics of lightning, Physics Reports, Volume 534, Issue 4, pp. 147-241, 2014.

[80] M. Miki, V. A. Rakov, K. J. Rambo, G. H. Schnetzer, M. A. Uman, Electric field near triggered lightning channels measured with Pockels sensors, J. Geophys. Res.107 (D16), ACL 2-1–ACL 2-11, (2002).

[81] J. Cen, P. Yuana , S. Xue and X. Wang, Resistance and internal electric field in cloud-to-ground lightning channel, Applied Physics Letters 106, 054104 (2015); https://doi.org/10.1063/1.4907287.

[82] S. J. Heckman and E. R. Williams, "Corona envelopes and lightning currents" J. Geophys. Res., vol. 94, pp. 13287–13294, 1989.

[83] B. N. Gorin, "Mathematical modeling of the lightning return stroke,"Elektrichestvo, vol. 4, pp. 10–16, 1985.

[84] G. Maslowski, V. A. Rakov, J. M. Cvetic, M. Miki, An improved model for prediction of the dynamics of lightning channel corona sheath, in: 20th International Zurich Symposium on EMC, Zurich, 2009.

[85] V. Cabrera, V. Cooray, On the mechanism of space charge generation and neutralization in a coaxial cylindrical configuration, J. Geophys. Res. 38, 187–196, (1992).

[86] J. Cvetic, M. Ignjatovic, M. Tausanovic, N. Mijajlovic, D. Pavlovic, F. Heidler, Electric field close to lightning channel in the presence of current reflections from the ground, 33rd International Conference on Lightning Protection - ICLP 2016, Estoril, Portugal.

[87] R. Thottappillil, V. Rakov, M. Uman, Distribution of charge along the lightning channel: relation to remote electric and magnetic fields and to return strokemodels, J. Geophys. Res. 102 (D6), 6987–7006, (1997).

[88] M. Tausanovic, M. Ignjatovic, J. Cvetic, F. Heidler, M. Alimpijevic, D. Pavlovic, Influence of current reflections from the ground on corona sheath dynamics during the return stroke, Electric Power System Research, Vol. 143, pp 84-98, 2017.

[89] P. K. Kythe, P. Puri, Computational Methods for Linear Integral Equations, Boston, USA, Birkhäuser, 2002.

[90] http://mathworld.wolfram.com.

[91] Tikhonov A. N. On ill-posed problems of linear algebra and the stable method for solving them // DAN SSSR, 1965, vol. 163, No. 3, pp. 591–594.

[92] D. Pavlović, G. Milovanović, J. Cvetić, Calculation of the channel discharge function for the generalized lightning traveling current source return stroke model, Filomat 32:20 (2018), 6937–6951, https://doi.org/10.2298/FIL1820937P.

[93] Д. Павловић, Г. Миловановић, J. Цветић, Н. Мијајловић, М. Игњатовић, Нумеричко решавање Волтерине интегралне једначине прве врсте за генералисани модел повратног удара са путујућим струјним извором, 61. конференција за електронику, телекомуникације, рачунарство, аутоматику и нуклеарну технику, ЕТРАН 2017, Кладово, 5. до 8. јуна 2017. године (ISBN: 987-86-7466-692-0).

[94] J. Hadamard, Sur les problèmes aux dérivées partielles et leur signification physique, Princeton University Bulletin, pp. 49–52., (1902).

[95] D. P. Gaver, Jr., Observing stochastic processes and approximate transform inversion, Oper. Res. **14** (1966), 444–459.

[96] A. Talbot, The accurate numerical inversion of Laplace transforms, IMA J. Appl. Math. **23** (1979), 97–120.

[97] J. Mikulović, T. Šekara, The Numerical Method of Inverse Laplace Transform for Calculation of Overvoltages in Power Transformers and Test Results, SERBIAN JOURNAL OF ELECTRICAL ENGINEERING, Vol. 11, No. 2, June 2014, 243-256, DOI: 10.2298/SJEE131123020M.

[98] M. Lazarević, Z. Gordić, B. Lukić, Primena numeričkih metoda inverzne Laplasove transformacije u rešavanju jedne klase parcijalnih diferencijalnih jednačina fizičkih procesa, INFOTEH-JAHORINA Vol. 12, March 2013.

[99] G. V. Milovanović, Numerička analiza II, Naučna knjiga, Beograd, 1991.

[100] G. V. Milovanović, Numerička analiza III, Naučna knjiga, Beograd, 1991.

[101] G. Mastroianni, G. V. Milovanović, Interpolation Processes: Basic Theory and Applications, Springer, Berlin – Heidelberg, 2008.

[102] C. Lubich, Convolution quadrature and discretized operational calculus. I, Numer. Math. **52** (1988), 129–145.

[103] C. Lubich, Convolution quadrature and discretized operational calculus. II, Numer. Math. **52** (1988), 413–425.

[104] M. Schanz, Wave Propagation in Viscoelastic and Poroelastic Continua: A Boundary Element Approach, Springer Berlin Heidelberg, 03.12.2010.

[105] U. Langer, M. Schanz, O. Steinbach, W. Wendland, Fast Boundary Element Methods in Engineering and Industrial Applications, Springer, 2012th Edition.

[106] J. Ma, H. Liu, On the convolution quadrature rule for integral transforms with oscillatory Bessel kernels, Symmetry **10**, no. 7: 239 (2018), 15 pp.

[107] L. Banjai, Multistep and multistage convolution quadrature for the wave equation: algorithms and experiments, SIAM J. Sci. Comput. 32, no. 5 (2010), 2964–2994.

[108] G. Monegato, L. Scuderi, M. P. Stanic, Lubich convolution quadratures and their application to problems described by space-time BIEs, Numer. Algorithms 56 (2011), 405–436.

[109] G. Monegato, L. Scuderi, Quadrature rules for unbounded intervals and their application to integral equations, In: Approximation and Computation: In Honor of Gradimir V. Milovanović (W. Gautschi, G. Mastroianni, Th.M. Rassias, eds.), Springer Optimization and its Applications, Vol. 42, Springer, New York, 2011, pp. 185–208.

[110] M. Mori, M. Sugihara, The double-exponential transformation in numerical analysis, Journal of Computational and Applied Mathematics 127(1-2):287-296, January 2001, DOI: 10.1016/S0377-0427(00)00501-X.

[111] Tingting An, Ping Yuan, Guorong Liu, Jianyong Cen, Xuejuan Wang, Meng Zhang, and Yingying An, The radius and temperature distribution along radial direction of lightning plasma channel, Physics of Plasmas 26, 013506 (2019); https://doi.org/10.1063/1.5059363.

[112] S. Kumar, Exact evaluations of some Meijer G-functions and probability of all eigenvalues real for product of two Gaussian matrices, Journal of Physics A Mathematical and Theoretical 48(44):445206, October 2015.

[113] https://www.wolframalpha.com.

[114] C. F. Curtiss and J. O. Hirschfelder, Integration of Stiff Equations, Proc US Nat. Acad. Sci, 38, # 3 pp 235-243, March, 1952.

Biographical details (in Serbian)

Драган (Миладин) Павловић је рођен 13. септембра 1988. године у Горњем Милановцу. Основну школу „Свети Сава" у Горњем Милановцу уписао је 1995. године, а завршио је 2003. године као носилац Вукове дипломе. Након тога је завршио средњу школу у Горњем Милановцу 2007. године као носилац Вукове дипломе и као носилац треће награде на републичком такмичењу из енергетске електронике 2006. године. Основне академске студије завршио је у јулу 2011. године на Електротехничком факултет у Београду, на Одсеку за физичку електронику, смер Наноелектроника, оптоелектроника и ласерска техника, са просечном оценом 8.44. Дипломски рад под називом „Високоимпедансни јединични појачавач напона мале дисторзије" одбранио је са оценом 10 под менторством др Слободана Петричевића.

Мастер студије на Електротехничком факултету у Београду уписао је у октобру 2011. године на модулу Наноелектроника, оптоелектроника и ласерска техника. Испите је положио са просечном оценом 10.00, а мастер рад под називом „Температурно стабилисан ЛЕД" одбранио је у јуну 2012. са оценом 10 под менторством др Слободана Петричевића.

Докторске студије је уписао новембра 2012. године на Електротехничком факултету Универзитета у Београду, модул Наноелектроника и фотоника. Положио је све испите предвиђене наставним планом и програмом са просечном оценом 10.00 и урадио је све обавезе предвиђене планом и програмом докторских студија.

У фебруару 2013. године запослио се на Електротехничком факултету у звању истраживач-приправник као учесник на пројекту Министарства просвете, науке и технолошког развоја под бројем ТР37019 „Електродинамика атмосфере у урбаним срединама Србије" чији је руководилац професор Јован Цветић. У фебруару 2015. године изабран је у звање истраживач-сарадник, а у фебруару 2018. је реизабран у исто звање.

Током свог досадашњег рада на Електротехничком факултету у Београду, кандидат је учествовао у научно-истраживачком раду из области физике плазме,

физике атмосферских пражњења и нумеричке математике. Драган Павловић је аутор или коаутор три научна рада у часописима са SCI листе, двадесет један рад на конференцијама међународног значаја и пет радова на конференцијама националног значаја.

Такође, учествовао је у експерименталном раду и унапређивању лабораторијских вежби у Лабораторији за Климатологију и екологију атмосфере на Електротехничком факултету.

Кандидат је добио Захвалницу регионалног центра за таленте Београд II за допринос у развоју рада са надареном и талентованом школском популацијом, у склопу програмског рада центра за таленте у школској 2017/2018. години.

Активно говори енглески језик, а поседује и основно знање немачког језика.

Прилог 1.

Изјава о ауторству

Име и презиме аутора: Драган (Миладин) Павловић

Број индекса: 2012/5002

Изјављујем

да је докторска дисертација под насловом

" Еволуција плазма канала код тригерованих атмосферских пражњења" (енгл.
" Plasma channel evolution in the triggered lightning discharge ").

- резултат сопственог истраживачког рада;
- да дисертација у целини ни у деловима није била предложена за стицање друге дипломе према студијским програмима других високошколских установа;
- да су резултати коректно наведени и
- да нисам кршио/ла ауторска права и користио/ла интелектуалну својину других лица.

Потпис аутора

У Београду, 21.2.2019.

Изјава о истоветности штампане и електронске верзије докторског рада

Име и презиме аутора: Драган (Миладин Павловић)

Број индекса: 2012/5002

Студијски програм: Електротехника и рачунарство (модул Наноелектроника и фотоника)

Наслов рада: "Еволуција плазма канала код тригерованих атмосферских пражњења" (енгл. " Plasma channel evolution in the triggered lightning discharge ")

Ментор: др Јован Цветић, редовни професор

Изјављујем да је штампана верзија мог докторског рада истоветна електронској верзији коју сам предао/ла ради похрањена у **Дигиталном репозиторијуму Универзитета у Београду.**

Дозвољавам да се објаве моји лични подаци везани за добијање академског назива доктора наука, као што су име и презиме, година и место рођења и датум одбране рада.

Ови лични подаци могу се објавити на мрежним страницама дигиталне библиотеке, у електронском каталогу и у публикацијама Универзитета у Београду.

Потпис аутора

У Београду, 21.02.2019.

Прилог 3.

Изјава о коришћењу

Овлашћујем Универзитетску библиотеку „Светозар Марковић" да у Дигитални репозиторијум Универзитета у Београду унесе моју докторску дисертацију под насловом:

"Еволуција плазма канала код тригерованих атмосферских пражњења" (енгл. "Plasma channel evolution in the triggered lightning discharge ")

која је моје ауторско дело.

Дисертацију са свим прилозима предао/ла сам у електронском формату погодном за трајно архивирање.
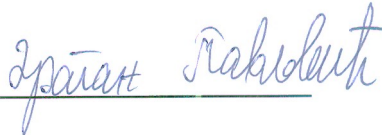
Моју докторску дисертацију похрањену у Дигиталном репозиторијуму Универзитета у Београду и доступну у отвореном приступу могу да користе сви који поштују одредбе садржане у одабраном типу лиценце Креативне заједнице (Creative Commons) за коју сам се одлучио/ла.

1. Ауторство (CC BY)

2. Ауторство – некомерцијално (CC BY-NC)

3. Ауторство – некомерцијално – без прерада (CC BY-NC-ND)

4. Ауторство – некомерцијално – делити под истим условима (CC BY-NC-SA)

5. Ауторство – без прерада (CC BY-ND)

6. Ауторство – делити под истим условима (CC BY-SA)

(Молимо да заокружите само једну од шест понуђених лиценци.
 Кратак опис лиценци је саставни део ове изјаве).

Потпис аутора

У Београду, 21.2.2019.

1. **Ауторство**. Дозвољавате умножавање, дистрибуцију и јавно саопштавање дела, и прераде, ако се наведе име аутора на начин одређен од стране аутора или даваоца лиценце, чак и у комерцијалне сврхе. Ово је најслободнија од свих лиценци.

2. **Ауторство – некомерцијално**. Дозвољавате умножавање, дистрибуцију и јавно саопштавање дела, и прераде, ако се наведе име аутора на начин одређен од стране аутора или даваоца лиценце. Ова лиценца не дозвољава комерцијалну употребу дела.

3. **Ауторство – некомерцијално – без прерада**. Дозвољавате умножавање, дистрибуцију и јавно саопштавање дела, без промена, преобликовања или употребе дела у свом делу, ако се наведе име аутора на начин одређен од стране аутора или даваоца лиценце. Ова лиценца не дозвољава комерцијалну употребу дела. У односу на све остале лиценце, овом лиценцом се ограничава највећи обим права коришћења дела.

4. **Ауторство – некомерцијално – делити под истим условима**. Дозвољавате умножавање, дистрибуцију и јавно саопштавање дела, и прераде, ако се наведе име аутора на начин одређен од стране аутора или даваоца лиценце и ако се прерада дистрибуира под истом или сличном лиценцом. Ова лиценца не дозвољава комерцијалну употребу дела и прерада.

5. **Ауторство – без прерада**. Дозвољавате умножавање, дистрибуцију и јавно саопштавање дела, без промена, преобликовања или употребе дела у свом делу, ако се наведе име аутора на начин одређен од стране аутора или даваоца лиценце. Ова лиценца дозвољава комерцијалну употребу дела.

6. **Ауторство – делити под истим условима**. Дозвољавате умножавање, дистрибуцију и јавно саопштавање дела, и прераде, ако се наведе име аутора на начин одређен од стране аутора или даваоца лиценце и ако се прерада дистрибуира под истом или сличном лиценцом. Ова лиценца дозвољава комерцијалну употребу дела и прерада. Слична је софтверским лиценцама, односно лиценцама отвореног кода.